

Study of crystallography and erosion behavior of single and multilayer coatings used for applications in aero engines

Von der Fakultät für Maschinenbau, Elektrotechnik und Wirtschaftsingenieurwesen
der Brandenburgischen Technischen Universität Cottbus – Senftenberg
zur Erlangung des akademischen Grades eines
Doktors der Ingenieurwissenschaften
genehmigte Dissertation

vorgelegt von

M. Sc. Muhammad Naveed

geboren am 20.07.1983 in Karachi, Pakistan

Vorsitzender: Prof. Dr.-Ing. Arnold Kühhorn
Gutachter: Prof. Dr.-Ing. habil. Sabine Weiß
Gutachter: Prof. Dr.-Ing. Alfons Fischer

Tag der mündlichen Prüfung: 09.07.2015

Acknowledgement

The present research was performed during my scientific activities at the Chair of Materials and Physical Metallurgy at the Brandenburg Technical University Cottbus-Senftenberg.

I would like to express my deep gratitude to Prof. Dr.-Ing. habil. Sabine Weiss and Prof. Dr.-Ing. Christoph Leyens for giving me the opportunity to perform this scientific work and assisting me in the scientific supervision in the later or initial stages of my work respectively.

I am very thankful to Prof. Dr.-Ing. Alfons Fischer for his interest and the evaluation of my work as second supervisor.

I am grateful to Dr.-rer.nat. Kai Ortner (IST Fraunhofer) and Dr. Ing. Arturo Flores Renteria (Siemens AG) for the scientific and technical discussions and without his help this work has not been possible.

I am especially thankful to my colleagues at the Chair of Materials and Physical Metallurgy for their patience and help for conducting this research work.

I would like to emphasize my gratitude for Dr.-Ing. Stefan Bolz and the entire service team from CemeCon AG for helping me out in troubleshooting the problems related to coating machine and their useful advices.

My very special thanks to Dr.-Ing. Stefan Haaga, Dr.-Ing. Jens Brechbuehl for their scientific assistance in my work. I am also thankful to Dr.-Ing. Wolfram Pitschke and the entire service team of Bruker AG for their technical assistance in conducting the experiments.

At the same time I would like to thank M. Sc. Chittaranjan Das (Chair of Practical Physics) for his help for his technical help.

Last but not the least I would like to thank my parents and my family for their moral support during my work and stay in Cottbus.

Table of Contents

List of Figures	iii
List of Tables.....	vi
Abbreviation	vii
1. Introduction	1
2. Literature Survey	4
2.1. Deterioration of turbomachinery performance due to erosion of gas turbine components	5
2.2. Solid Particle Erosion.....	6
2.3. Physical Vapor Deposition.....	7
2.3.1. Magnetron Sputtering.....	8
2.3.2. Reactive Magnetron Sputtering	10
2.4. Coating Deposition and Structure Zone Models	12
2.4.1. Coating Deposition Mechanisms	12
2.4.2. Structural Models.....	13
2.5. Erosion resistant coatings	16
2.5.1. Single layer Coatings.....	16
2.5.2. Multilayer Coatings.....	17
2.5.3. Design of an erosion resistant coating system	18
3. Experimental Setup.....	20
3.1. PVD- Coating Machine and coating process description.....	20
3.2. Coating Characterization	21
3.2.1. Coating Thickness Measurements	21
3.2.2. Adhesion Testing	21
3.2.3. Nanoindentation	22
3.2.4. X-ray Diffraction	23
3.2.5. Scanning Electron Microscopy.....	24
3.2.6. X-Ray Photon Spectrometry	24
3.3. Erosion Testing.....	25
3.3.1. Erosion Test Rig	25
3.3.2. Properties of Erodent and Laser Doppler Anemometer Measurements.....	26
4. Materials.....	27
4.1. Inconel 718	27
4.2. Chromium	28
4.3. Titanium.....	29
4.4. Chromium Nitride	30

4.5.	Titanium Nitride.....	31
5.	Deposition Parameters and properties of multilayer coatings	33
5.1.	Deposition parameters and coating structures	33
5.1.1.	Cr/CrN Multilayer.....	33
5.2.	Mechanical Properties.....	37
5.2.1.	Cr/CrN Multilayer.....	37
5.2.2.	CrN/X (X=Ti, TiN) Multilayer, TiN Single layer	38
5.3.	Adhesion behavior of coatings.....	39
5.3.1.	Cr/CrN Multilayer.....	39
5.3.2.	CrN/X (X=Ti, TiN), TiN Single layer.....	41
6.	Crystallography and XPS Analysis.....	43
6.1.	Phase Analysis.....	43
6.1.1.	Cr/CrN Multilayer Coatings	43
6.1.2.	CrN/X (X=Ti,TiN) Multilayer Coatings, TiN single layer	47
6.2.	Crystal Size Determination.....	49
6.2.1.	Instrumental Broadening Analysis	50
6.2.2.	Scherrer Method.....	50
6.3.	Stress Analysis	52
6.3.1.	$\sin^2 \psi$ - Method for stress analysis	52
6.3.2.	Stress Measurements.....	54
7.	Erosion Behavior	56
7.1.	Cr/CrN Multilayer Coatings	56
7.1.1.	Gravimetric Analysis.....	56
7.1.2.	Erosion Mechanism	59
7.2.	CrN/X (X=Ti,TiN) Multilayers, TiN single layer	65
7.2.1.	Gravimetric analysis	65
7.2.2.	Erosion Mechanism	67
7.3.	On the design of erosion resistant coatings	72
7.3.1.	Correlation between H^3/E^2 and erosion rate	72
7.3.2.	Effect of elastic mismatch between coating and substrate.....	74
8.	Conclusions and future prospects	78
	References	81

List of Figures

Figure 1.1: Landing of aircrafts in dusty environments leading to erosion of components (Reference: Airbus).....	1
Figure 2.1: A comparison of eroded compressor blade and new blade [10]	4
Figure 2.2 :(a) Static pressure observed around blade near tip (b) corrected mass flow rate with reference to change in pressure rise coefficient and adiabatic efficiency [16].....	6
Figure 2.3: Erosion mechanism in (a) ductile (b) brittle material [37].....	7
Figure 2.4: Classification of PVD Methods	8
Figure 2.5: (a) Schematic of a magnetron sputtering process (b) Plasma generation in a conventional circular magnetron.....	9
Figure 2.6: Illustration of various magnetron sputter configurations (a) Conventional or balanced magnetron sputtering (CM) (b) Unbalanced Magnetron Sputtering (UBM) (c) Magnetron with Additional Coil (MAC) [41].....	10
Figure 2.7: Schematic illustration of (a) deposition rate of sputtered films (b) partial pressure of reactive gas as a function of flow rate [47]	11
Figure 2.8: Atomistic growth of coatings structure according to various models (a) Frank-van-der-Merve (b) Volume Weber (c) Stranski-Krastov	12
Figure 2.9: Structure Zone Model proposed by Movchan and Demchishin [53].....	13
Figure 2.10: Structure Zone Model proposed by Thornton for sputtered metal coatings [60].....	15
Figure 2.11: Sturcture zone model proposed by Meisser et. al. [62].....	16
Figure 2.12: A schematic of the important components for the design of an erosion resistant coating	19
Figure 3.1: PVD coater CC800/9 from CemeCon AG used for the coating of specimen.....	20
Figure 3.2: Working principle of ball crater method.....	21
Figure 3.3: (a) Working principle of Scratch Tester (b) Scratch Tester from CSM Instruments.....	22
Figure 3.4: A load-displacement curve showing various phases of indenter loading	23
Figure 3.5: Schematic of (a) Braggs principle based on interference of incident and reflected rays (b) Grazing Incidence X-Ray Diffractometer	24
Figure 3.6: Erosion test rig showing various components.....	25
Figure 3.7: (a) SEM image of SiO ₂ particles used as erodent (b) velocity measurement of particles using LDA	26
Figure.4.1: BSE image of Inconel 718 super alloy.....	27
Figure 4.2: Coating structure of Cr at various cathode power (a) 2000 W (b) 3500W	29
Figure 4.3: Titanium-single layer coatings at various substrate bias (a) 60 V (b) 90V (c) 120V	30
Figure 4.4: Structures of CrN coatings deposited at various N ₂ /Ar realtionships (a) 0.15 (b) 0.23 (c) 0.37	31
Figure 4.5: Coating structure of TiN coatings at various cathode powers (a) 6000 W (b) 7000 W	32
Figure 5.1: Coating structure of Cr ₃ /CrN ₁ multilayer coating grown on Silicium wafer(left) individual Cr and CrN single layers (right)	33
Figure 5.2: SEM analysis of surface quality of the deposited (a) Ti/CrN (b) TiN/CrN coatings (c) TiN coating	35
Figure 5.3: Coating structure of Ti ₁ /CrN ₃ coatings showing detailed column growth on the surface of the coating and columnar structure in cross-section.....	35
Figure 5.4: Coating structure of TiN ₁ /CrN ₃ coatings showing detailed column growth on the surface of the coating and columnar structure in cross-section	36

Figure 5.5: Coating structure of TiN coating showing detailed column growth on the surface of the coating and columnar structure in cross-section	36
Figure 5.6: SEM images of scratched Cr1/CrN3 coating	40
Figure 5.7: SEM images of scratched Cr1/CrN1 coating	40
Figure 5.8: SEM images of scratched Ti1/CrN3 coating	41
Figure 5.9: SEM images of scratched TiN1/CrN3 coating	41
Figure 5.10: SEM images of scratched TiN coating	42
Figure 6.1: XRD Analysis of Cr/CrN coatings (a) Cr1/CrN3 (b) Cr0.25/CrN3.75(c) Cr3/CrN1	44
Figure 6.2: XPS analysis of the CrN coating showing various phases and respective binding energies	45
Figure 6.3: XRD Analysis of Cr/CrN coatings (a) Cr1/CrN1 (b) Cr0.5/CrN0.5(c) Cr0.25/CrN0.25 ...	46
Figure 6.4: XRD Analysis of TiN single layer coating	47
Figure 6.5: XRD Analysis of Ti/CrN multilayer coating	48
Figure 6.6: XRD Analysis of TiN/CrN multilayer coating	48
Figure 6.7: Illustration of relationship between grain size and material hardness [112].....	49
Figure 6.8: Schematic diagram of the macrostress σ versus T_s/T_m	52
Figure 6.9: Shift of diffraction peak with changing tilt angle	53
Figure 6.10: Peaks observed at various Chi angles (a) @44.393° for Cr (110) (b) @63.204° for CrN(220) in Cr1/CrN3 multilayer coating	54
Figure 6.11: $\sin^2\psi$ plots for (a) Cr-layer (b) CrN-layer performed for Cr1/CrN3 multilayer coating ..	54
Figure 6.12: Peaks observed at various Chi angles (a) @44.393° for CrN (200) (b) @63.204° for CrN(220) in Cr0.25/CrN3.75 multilayer coatings.....	55
Figure 6.13: $\sin^2\psi$ plots for a CrN-layer in a Cr0.25/CrN3.75 multilayer coating	55
Figure 7.1: Macroscopic images of multilayer Cr/CrN multilayer coatings	57
Figure 7.2: Gravimetric measurements for erosion of multilayer Cr/CrN coatings at 30° impact angle	58
Figure 7.3: Gravimetric measurements observed during erosion of multilayer Cr/CrN coatings at an incidence angle of 90°	59
Figure 7.4: Cr1/CrN1 coating at (a-b) 90 °incidence angle.....	60
Figure 7.5: Intercolumnar shear sliding of (a) Cr1/CrN1 coating (b) Schematic.....	61
Figure 7.6: (a) SEM image of Cr1/CrN3 at 90° impact angle (a) surface (b) cross-section.....	61
Figure 7.7: Erosion mechanism observed for Cr1/CrN3 multilayer coatings (a) incidence angle 30° (b) incidence angle 90°	62
Figure 7.8: (a) Single particle impact Cr3/CrN1 (b) Cross-sectional image of Cr3/CrN1 at normal incidence angle.....	63
Figure 7.9: SEM image of Cr0.5/CrN0.5 at 90° impact angle (a) single particle impact (b) cross-section image	65
Figure 7.10: Gravimetric analysis of Multilayer and Single layer coatings at 30°.....	66
Figure 7.11: Mass Loss graphs of various multilayer and monolayer coatings eroded at 90° impact angle	66
Figure 7.12: Optical images observed for Ti1/CrN3 after various intervals during erosion tests at 30° impact angle	67
Figure 7.13: SEM images of Ti/CrN coatings at (a) 30° impact angle (b-d) 90° impact angle	68
Figure 7.14: Optical images observed for TiN1/CrN3 after various intervals during erosion tests at 30° impact angle	69
Figure 7.15: SEM images of TiN/CrN coatings a) 30° impact angle b) 90° impact angle	70
Figure 7.16: SEM images of TiN coatings at a-b) 30° impact angle.....	70

Figure 7.17: Optical images observed for TiN1/CrN3 after various intervals during erosion tests	71
Figure 7.18: Erosion behavior of TiN coating a-d) 90° impact angle	71
Figure 7.19: Relationship between Erosion rate and mechanical properties of coatings (a) Cr/CrN coatings (b) all tested single layer and multilayer coatings.....	73
Figure 7.20: Influence of elastic-modulus ratio on the (a) substrate-coating fracture (b) force-displacement response.....	75

List of Tables

Table 2-1: Factors influencing the erosion phenomenon	6
Table 2-2: Schematic of Structure Zone Model proposed by Movchan and Demchishin.....	14
Table 2-3: Literature analysis of investigated monolayer coatings for erosion applications	17
Table 2-4: Literature analysis of investigated multilayer coatings for erosion applications	18
Table 4-1: Atomic percentage of elements in Inconel718 alloy	27
Table 4-2: Properties of Chrome	28
Table 4-3: Properties of Titanium	29
Table 4-4: Properties of Chromium Nitride	30
Table 4-5: Properties of Titanium Nitride	31
Table 5-1: Deposition process parameters for Cr/CrN multilayer coatings	33
Table 5-2: Deposition process parameters for Ti/CrN, TiN/CrN, TiN coatings	34
Table 5-3: Mechanical properties of Cr/CrN multilayer coatings	37
Table 5-4: Mechanical properties of multilayer and single layer coatings.....	38
Table 5-5 Adhesion behavior of Cr/CrN multilayer coatings obtained through scratch tests	39
Table 6-1: Estimation of instrumental error through FWHM analysis of Al ₂ O ₃ standard	50
Table 6-2: Average crystal size analysis of multilayer and single layer coatings	51
Table 7-1: Dominant erosion mechanisms observed due to Ec/Es ratios.....	76
Table 7-2: Comparison of erosion rates for various coatings.....	77

Abbreviation

PVD- Physical Vapor Deposition
CVD- Chemical Vapor Deposition
DC- Direct Current
PLC- Product Life Cycle
SPE- Solid Particle Erosion
MTBO- Mean Time Between Overhauls
FEM- Finite Element Analysis
CMS- Conventional/Balanced Magnetron Sputtering
UBM- Unbalanced Magnetron Sputtering
MAC- Magnetron with Additional Coil
RG- Reactive Gas
Th-Homologous Temperature
Tm-Melting Temperature
SZM- Structure Zone Model
QCSM- Quasi Continuous Stiffness Measurement
SEM- Scanning Electron Microscopy
TEM- Transmission Electron Microscopy
XRD- X-Ray Diffraction
SE-Secondary Electrons
BSE- Back Scattered Electrons
DLC- Diamond Like Carbon
Lc- Critical Load
ASTM- American Society of Testing Materials
CLSM- Confocal Laser Scanning Microscopy
EDS- Electron Dispersive Spectroscopy
WDS- Wavelength Dispersive Spectroscopy
XPS- X-ray Photon Spectroscopy
dc- Critical Diameter of crystal
FWHM- Full Width Half Maximum

H/E- Strain to elastic deformation

H3/E2- Strain to onset of plastic deformation

r- radius of indenter (sphere)

Ec-Elastic Modulus of Coating

Ef- Elastic Modulus of Film/Coating

Es- Elastic Modulus of Substrate

bcc- body centered cubic crystal structure

fcc- face centered cubic crystal structure

hcp- hexagonal close packed crystal structure

ER-Erosion Rate

LDA- Laser Doppler Anemometer

UHV- Ultra High Vacuum

1. Introduction

With the increasing number of commercial and military flights, air-based gas turbine manufacturers are looking for suitable methodologies to improve the efficiency of the engines working. Many of the material related problems like fretting of components, corrosion, oxidation, bio-fouling etc. [1, 2] are generally encountered in the aero engines. One of the main problems encountered by the military engines due to their operation in dusty environment is the Solid Particle Erosion (SPE). This problem has been reported mainly for the helicopters and military airplanes operating in dusty environments. Literature reports that dust erosion proved to be a severe problem during the Vietnam War where engines have to be removed after 100 hours of operation. Even after two decades of technological advances, many of the helicopter engines have to be removed after 20 hours of operation during the Gulf War [3]. The particle erosion leads to the wear of components and hence lead to decrease of engine efficiency and inefficient use of fuel. The replacement of worn components also leads to increase in overhaul costs for the turbine manufacturers. Hence, heavy investments have been made in order to produce efficient filters but still very small particles are still able to enter the engine and erode the components [4].



Figure 1.1: Landing of aircrafts in dusty environments leading to erosion of components (Reference: Airbus)

A conventional method to reduce component wear is the use of erosion resistant coatings. Such coatings should bear high hardness along with high fracture toughness in order to absorb energy of the incoming erodent before plastic deformation takes place. Literature indicates a number of single layer coatings like TiN, ZrN [5], TiAlN and multilayer coatings like Ti/TiN [5, 6], Ti/TiC [5], W/WN [7], Ti/TiB₂ [8] as possible coatings systems against erosion.

A traditional way to deposit such type of coatings is the conventional Direct Current (DC) method which finds its roots in Physical Vapor Deposition (PVD) methods. By employing this method a high deposition rate along with defect free structure is observed for the coatings. Moreover, the process is regarded to be economical and user friendly in comparison to other PVD methods as no complicated electronic devices are used in order to achieve high density plasma or to direct the electrons towards the surface.

The aim of this work is to study the behavior of single layer ceramic coatings and multilayer metal-ceramic coatings deposited through DC method. In order to deposit a multilayer coating with a metallic and ceramic layer, a study of the properties of the individual layers is necessary to select the best performing coatings. A combination of the best performing layers would allow achieving a multilayer coating with required properties. The first part of the work focus on the properties of the materials used for the deposition of coatings. Mechanical properties like Hardness and E-Modulus, coating growth rate, coating structure etc. of the coatings have studied to provide a correlation of the coating behavior at various process parameters. The multilayer coatings are then deposited by selecting a combination of metal-ceramic or ceramic/ceramic coating on the basis of highest H^3/E^2 value obtained from the mechanical analysis.

In order to estimate the mechanical properties of the coatings, Inconel 718 alloy has been used as a substrate in the present study. The choice of Inconel 718 has been made due to its ability to withstand high temperatures (till 700 °C). The most frequent use of In718 is found in the last stages of low pressure compressors of an aero engine.

The research work deals with the deposition parameters used for the deposition of the coatings along with the discussion of the coating structure. Moreover, a discussion on the mechanical properties and the adhesion of the single and multilayer coatings has been added to this section. This section is followed by a crystallographic analysis of the deposited multilayer coatings. An estimation of the crystal size of the deposited coatings was done by analyzing the obtained diffractograms (phase analysis). Moreover, stress analysis of some of the deposited multilayer coatings has been included in order to explain the behavior of the individual metallic and ceramic components affecting the behavior of the coatings.

The next section includes the erosion testing of the deposited single and multilayer coatings. An analysis on the erosion wear has been conducted on an in house developed erosion test rig. A suitable erodent (SiO_2) with defined testing conditions has been used for the test. In order to understand the erosion behavior, the tests have been supported with gravimetric analysis and crack propagation analysis. Erosion rate analysis and their correlation with the measured mechanical properties have been performed to study the process in further detail.

The last section summarizes the important results which were obtained during the research work. Moreover, some recommendations have been added in this section which could be helpful for the development of erosion resistant coatings.

2. Literature Survey

Product Life Cycle (PLC) and asset management have always been key issues for the power generation companies. The integrity of the components after a particular time decides and controls the life of the machine. It has an influence on the direct and indirect costs of the product. Maintenance and repair of the components also play a vital role in improving the life cycle of a commodity. Gas turbine manufacturers have documented severe problems encountered due to the erosion of gas turbine blades especially during takeoff and landing in dusty environments. As a result of material removal, high maintenance costs are required in order to repair and many blades have to be replaced in severe cases [9].

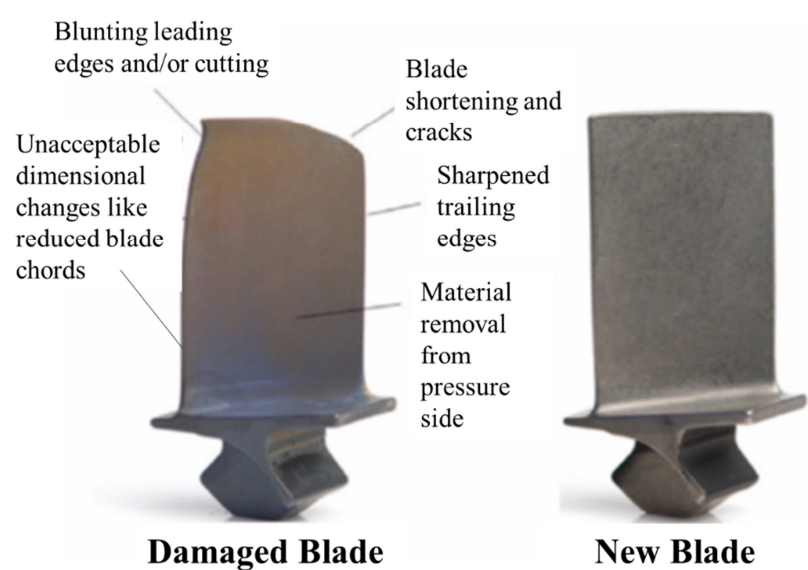


Figure 2.1: A comparison of eroded compressor blade and new blade [10]

Similar to other component degradation processes (fatigue, corrosion, oxidation), Solid Particle Erosion (SPE) has also been identified as one of the major problems which is responsible for the reduction of the life of a component. Solid Particle Erosion (SPE) is a wear process where particles strike against surfaces and promote material loss. Different models have been proposed which estimate the stresses of a moving particle imposing on a target surface [11, 12]. During the impact, the target can be locally scratched, extruded, melted and cracked in different ways. The imposed surface damage will vary with the target material, erodent particle, impact angle, erosion time, particle velocity, temperature, atmosphere and other factors. Solid particle erosion is usually defined in terms of weight loss per unit charge [13]. A comparison between new and tested blade can be observed in Fig. 2.1. Shortening of blade, sharpening of trailing edges, loss of material from pressure side and blunting of the leading edges were reported as some of the effects of the erosion on blades in sandy environments [10].

The main idea of erosion analysis is to understand the erosion mechanisms in general and to characterize the erosion resistance of materials in particular for a selected application (e.g. fluidized beds, nozzle flows, pneumatic flows in pipes etc.). An understanding on the effect of abrasive charge is not only meant to understand the different stages of erosion process but is also helpful in modeling and extrapolating laboratory data more precisely to field conditions [13].

2.1. Deterioration of turbomachinery performance due to erosion of gas turbine components

Erosion of low compressor gas turbine blades has been a serious problem for the manufacturers and users of industrial and aeronautical gas turbines. Particle erosion in compressors lead to the reduction in blade chord, changes in the shape of leading and trailing edge and an increase in surface roughness of the blade surface too [14]. Bons et al. reported an average roughness increase of 4-8 times greater due to erosion in comparison to after production roughness [15]. A lot of research has been conducted to observe the aerodynamic performance of the fan and blades after erosion which was determined in terms of blade geometry, axial flow velocity, flow angles, upstream pressure, temperature and Reynolds Number [3]. Ghenaïet *et. al* [16] reported a degradation of engine performance due to the blunting of blade leading edges, reduction of chord and increase tip clearance and surface roughness. Simulations on the reduction of static pressure after erosion with a mass flow of 0.69 kg/s are depicted in Fig. 2.2a. It is very clear from the illustration that high pressure drop occurs at the pressure and the suction side. Adiabatic efficiency which determines the efficiency of the engine after heat gain or loss which is important in order to acquire the actual work (Fig. 2.2b) showed a decrease of in 10 % after the ingestion of sand for 9 hours. Another important aspect is the pressure rise coefficient which determines the pressure drop passing through the turbomachine and is responsible for the engine efficiency.

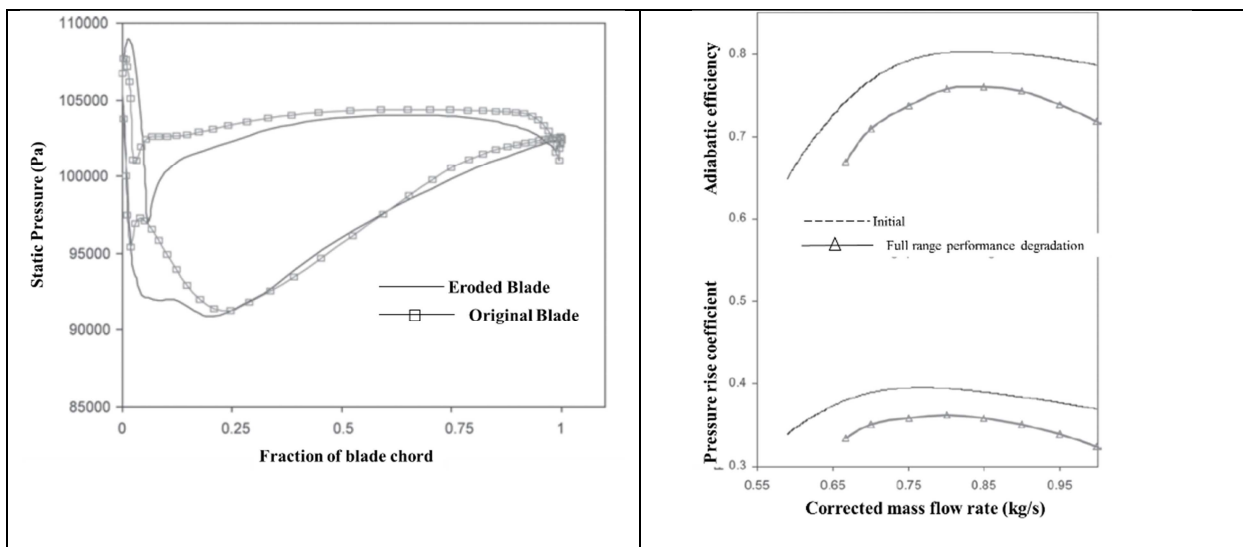


Figure 2.2 :(a) Static pressure observed around blade near tip (b) corrected mass flow rate with reference to change in pressure rise coefficient and adiabatic efficiency [16]

This ingestion of sand in the engine does not only lead to loss in power of the engine but also reduced Mean Time Between Overhauls (MTBO) which leads to increase in logistic support and the associated costs [4]. Maintenance costs of a three-stage blisk compressor were estimated to be about \$ 200.000 per year whereas \$1.000.000 for large compressors [17]. Another aspect of the erosion of compressor components is inefficiency of the fuel system which can lead to high costs for the organizations. A comprehensive study of the increased fuel consumption due to the erosion in turbine has been made by Uihlein et. al [17] where he reported an increase of 0.02 % of specific fuel consumption for an engine which does not land in dusty environments. The eroded components of such engines can be changed after 3000 cycles of flying. Alternatively, engines which are used in high aggressive dusty environments show an increase of 0.05% specific fuel consumption and the life time of the components were reported not to be more than 2000 cycles.

2.2. Solid Particle Erosion

Erosion because of solid particle impact is a complex process combining numerous wear processes instantly. A particle with a high velocity strikes the surface of the material imparting its kinetic energy into it. A consequence of this transfer of energy is the deformation of surface or removal of material. A number of factors have been discussed in literature describing their influence on the erosion process. Some of them can be found in Tab.2-1:

<i>Material Properties</i>	<i>Particle Properties</i>	<i>Air/Atmospheric Properties</i>
Fracture Toughness [18]	Shape [19, 20]	Incidence Angle [21, 22]
Hardness [23]	Size [24-26]	Particle Velocity [27, 28]
Material structure [29]	Hardness [30]	Particle Rotation[31]
Intinsic Stresses [32]		Particle Flux [33]
Microstructure [29]		Temperature [21, 34]
		Humidity[35]

Table 2-1: Factors influencing the erosion phenomenon

On the other hand a number of models have been discussed in literature to study the erosion behavior of systems. One of the first models developed for ductile materials was proposed by Finnie [28]. He studied the behavior of ductile materials by varying the incidence angles and velocity of the erodent. Finally he formulated a numerical model which predicted the erosion behavior of ductile materials. The proposed model also predicted that when particles attack a surface at shallow angles, craters having a length/depth ratio of 10:1 were observed depicting a cutting mechanism clearly. Nelson and

Gilchrist [36] studied a number of ductile materials and found that deformation takes place when an alloy is attacked at normal angles.

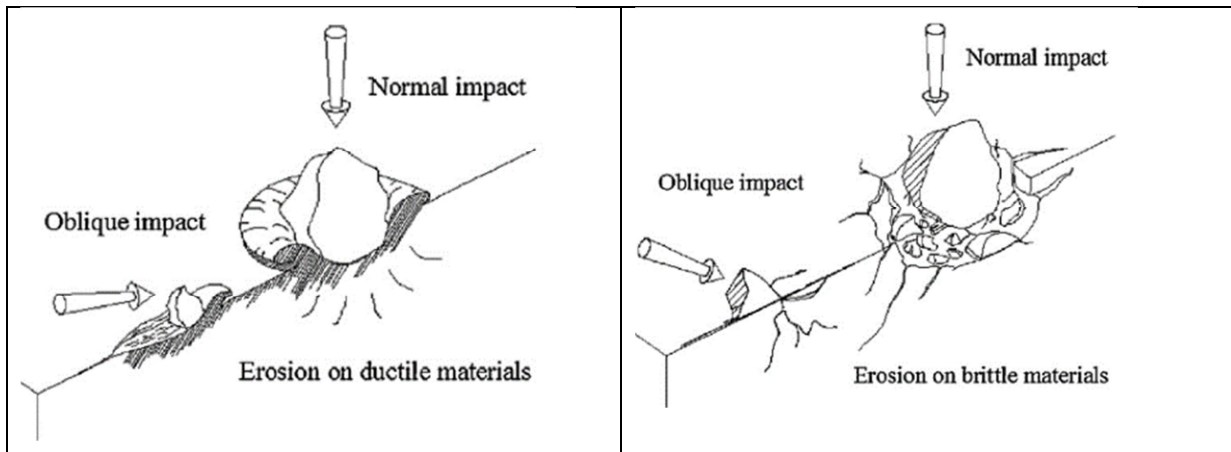


Figure 2.3: Erosion mechanism in (a) ductile (b) brittle material [37]

A schematic model of the erosion mechanism in a ductile material is depicted in Fig.2.3 [37]. They made an FEM analysis in order to understand the erosion behavior of Ti6Al4V alloy and found that material removal due to plastic deformation is one of the major wear processes at lower impingement angles for ductile materials. With increase in impingement angle, low material removal is observed due to an increase in plastic deformation. Hence, maximum depth of penetration occurs at oblique angles. Erosion in brittle material is generally defined by the Hertzian crack theory. According to Hertzian theory, the particle kinetic energy of the erodent is converted into the elastic deformation energy. When the deformation energy exceeds the elastic limit of the material, a plastic deformation is ought to be observed within the material [38]. Similar to ductile materials, a FEM model for the erosion of brittle materials was also devised by Wand and Chang (Fig. 2.3b) [37]. They found that formation of subsurface cracks is the major reason for the failure of brittle material. The normal component of the impinging velocity is responsible for the subsurface cracking the target. At oblique angles, a maximum value was observed for the normal component of the alloy. Moreover, high crack coalescence of the subsurface cracks is also observed at oblique angles. The behavior of penetration depth and the development of residual stresses in the subsurface are similar to that of ductile materials.

2.3. Physical Vapor Deposition

Physical Vapor Deposition (PVD) has been an effective method in order to deposit thin films which protect the surfaces from external effects.

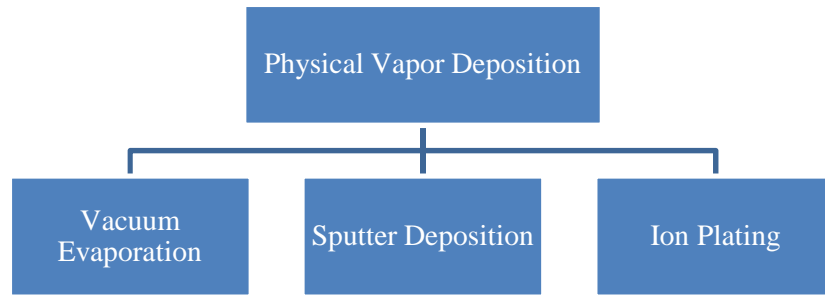


Figure 2.4: Classification of PVD Methods

PVD is a vacuum process where material is transported from an evaporator or a magnetron source in the form of vapors and then condensed on a suitable substrate. Vacuum evaporation refers to the thermal vaporization or sublimation of the source into vapor phase. Typical vacuum pressures of 10^{-3} to 10^{-6} Torr are used during vacuum evaporation processes depending on the contamination within the vacuum chamber. One of the main advantages of vacuum arc processes is the use of evaporator in solid as well as in liquid or gaseous form. Moreover, high purity in the deposited coating can be observed through this process. This method also offers an easy control and monitoring of deposition process. Good adhesion, high evaporation rates (approx.. 10^{-3} g/cm²s) and constant coating thickness are identified as advantages of the vacuum evaporation process [39].

Another PVD method often used is the magnetron sputtering process. In this process, Argon is used as a process gas and act as a medium for the transport of ions towards substrate. In comparison to vacuum evaporation, the coating material is not heated to transform into gas but are knocked out from the coating target in form of ions. Magnetron sputtering offers better adhesion due to highly energetic ions along with low sputtering rates [39]. Detailed information regarding the magnetron sputtering can be found in Section 2.3.1.

A third sub classified form of PVD method is the ion plating method. With the improvement of electro-magnetic field within the coating chamber (through the addition of strong magnets), high energy ions can be collected on the substrate. An increase in sputtering rate with a similar ion energy was reported for ion implanting as compared to magnetron sputtering. Moreover, the high adhesion and low deposition temperatures were also found to be among some advantages of ion plating process [39].

2.3.1. Magnetron Sputtering

In a basic magnetron sputtering process plasma is created in which the positively charged ions (Argon ions in most cases) are used to eject the electrons form the negatively charged targets. In order to eject the atoms from the target, the ions should have enough energy to dislodge the atoms from the target. The ejected atoms would find their way and condense on the substrate which is present in the

proximity of the magnetrons. Secondary electrons are also generated in this process which play their role in maintaining the plasma as can be observed in Fig. 2.5a. Magnetrons which are located behind the Metal or compound target, are series of magnets which are responsible for the concentration of electrons in the vicinity of the target. This concentration of electrons will lead to a higher probability of electron-atom collision resulting in increased ion bombardment of the target, higher sputtering rates, higher deposition rates etc. [40].

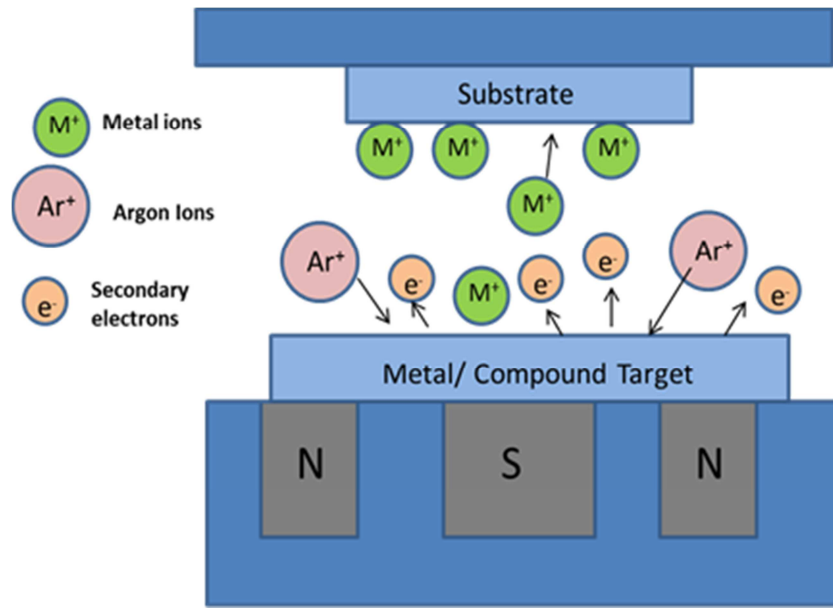


Figure 2.5: (a) Schematic of a magnetron sputtering process (b) Plasma generation in a conventional circular magnetron

A configuration of the conventional or balanced magnetron sputtering is depicted in Fig. 2.6a. In this case almost all of the field lines are trapped between the poles. In such a configuration the plasma discharge is concentrated in the target region due to high efficiency of trap and therefore the distance between target and substrate plays an important role [41]. Low coating deposition rates, low ion current densities, low energy of atoms during deposition are some of the properties defined for balanced magnetron sputtered coatings in literature [42].

In case of unbalanced magnetron sputtering (Fig. 2.6b), the magnetic field is directed towards the substrate by using high volume magnets leading to intensification of magnetic field at outer poles. In this case the plasma is not concentrated to the targets and allows a flow towards the substrate [40]. An important parameter is the ion-to-atom ratio which defines the structure development and properties of the coating. In case of unbalanced magnetron sputtering, the ion-to-atom ratio remains fixed at a constant target to substrate distance [41].

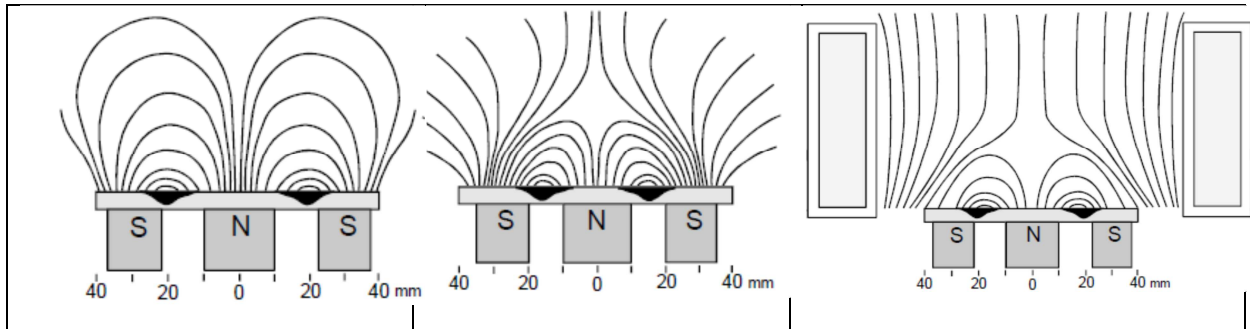


Figure 2.6: Illustration of various magnetron sputter configurations (a) Conventional or balanced magnetron sputtering (CM) (b) Unbalanced Magnetron Sputtering (UBM) (c) Magnetron with Additional Coil (MAC) [41]

A configuration of the Magnetron with Additional Coil (MAC) can be shown in Fig. 2.6c. In this case an extra coil is added to the unbalanced magnetron configuration in front of the target. This allows the control of the magnetic field in the target-substrate region [41]. Studies show that in an additional coil configuration, the plasma was found to be uniform with low values of ion to atom ratio. A reason for this type of behavior is the electron flow deviation of the radiating magnetic field away from the substrate area leading to low density plasma [43, 44].

A number of advantages have been addressed in literature for magnetron sputtering in comparison to other PVD methods. High adhesion is obtained due to higher electron energy achieved for the ions arriving at the substrate. Due to no chemical reactions, the stoichiometry of the coating and the substrate remains unchanged. A possibility to deposit coatings at low temperatures can be realized using magnetron sputtering. Almost no limitation on the type of substrate or coating material can be observed for magnetron sputtering. Reproducibility in quality and thickness of the coating was reported too [45].

2.3.2. Reactive Magnetron Sputtering

Reactive magnetron sputtering is a process where reactive gas like N, O etc. takes part in order to form respective metallic nitrides or oxides. Similar to magnetron sputtering, an inert gas like Ar is added as a working gas responsible for ejecting the atoms from the target surface layer. The ejected metal ions together with the inert and reactive gas molecules form plasma and the magnetron allows this plasma to concentrate close to the target surface. This confinement of plasma near the target is supported by the permanent magnets. A high probability of collisions between molecules and atoms takes place leading to highly ionized plasma. These ionized particles deposit on the chamber walls as well as on the negatively charged substrate [46]. The reactive gas process is generally controlled by the amount of reactive gas induced into the chamber and the process is generally classified into three phases (a) metallic (b) transition and (c) reactive. A characteristic of reactive mode is the lower deposition rate of the compound (CrN, TiN, TiO₂ etc) than in pure metallic mode. The reason for the low deposition in

reactive mode is the low sputtering yield of ceramic compounds compared to pure metallic compounds. The sputtering yield in a reactive phase is dependent on the sputtering yield of the metallic material and the type of reactive gas used in the chamber [47].

Some of the limitations involved in the reactive magnetron sputtering process are as follows:

a) Hysteresis Losses:

As mentioned in the previous section, the reactive sputtering modes works in three different modes a) metallic mode (b) transition mode and (c) reactive mode (Fig. 2.7a). A decrease in coating thickness and deterioration of coating quality is generally observed during the reactive sputtering process which is generally related to the hystereses losses. A general schematic of the hysteresis losses can be shown in Fig. 2.7b where hysteresis occur only in discharge mode. At an interval AB low rates of reactive gas (RG) were introduced into the chamber and hence all the amount of reactive gas is gettered by the sputter material. At stage B, the flow rate of reactive gas is equal to the gettering rate of sputtered material. During the interval BC, the flow rate of reactive gas further increased leading to linear increase of the chamber pressure and decrease in the deposition rate of coating. A further increase of reactive gas at point C, shows again an increase in overall pressure and a constant coating thickness in interval CD. Interval DE shows that a result in reactive gas would decrease in a linear decrease in pressure of reactive gas leading to a delayed metal mode sputtering. This delay is observed due to the presence of metallic compounds present on the target surface and time is required to be completely removed from the surface. Hence the area BCEF is referred as a closed hysteresis loop in literature [47, 48].

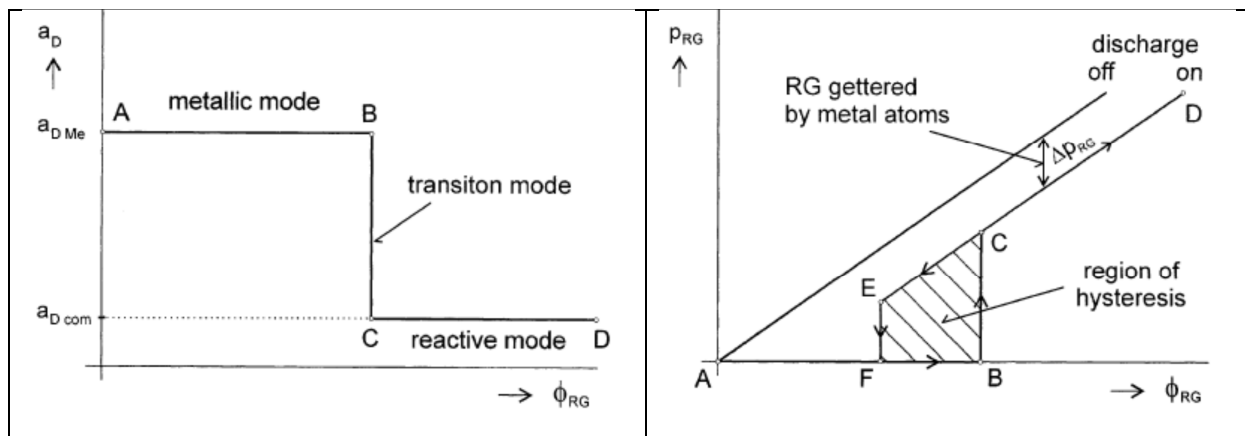


Figure 2.7: Schematic illustration of (a) deposition rate of sputtered films (b) partial pressure of reactive gas as a function of flow rate [47]

A hysteresis loss in a reactive magnetron sputtering is an undesirable process as it does not allow the deposition of coating with a reliable stoichiometry. This problem generally arises due to the competitive sputtering of the metal and its deposited compound during the reactive sputtering process.

This deposition of metallic compounds on the target surface is referred as target poisoning which leads to unstable sputtering of the target [47].

b) Arcing

The existence of uneroded areas on the planar magnetrons is usually found in the neighborhood of magnetron race track. During the reactive sputtering process, metallic compounds are deposited on the surface which decreases the efficiency of the metallic target. These metallic compounds acts as insulators on the metallic target and by charging them during the process leads to arcing in front of the metallic targets. Arcing leads to inhomogeneity and coatings defects during the sputtering process [47].

2.4. Coating Deposition and Structure Zone Models

2.4.1. Coating Deposition Mechanisms

The condensation of a vapor phase on a solid substrate defines the growth of the coatings and decides the material properties. The atomic growth of coatings is generally associated to the difference of interfacial energies evolved due to the deposition of vapor phase on the substrate which is termed as “free surface energy” and “adhesion energy”. A number of coating deposition models has been described in literature to understand the atomic growth behavior of coatings. The most discussed coating deposition models are discussed in next sections.

Frank-van-der-Merwe was one of the first scientists who introduced a model of a layer-by-layer growth of atoms on surfaces. According to the model, after the first monolayer is formed, the subsequent monolayer finds its way on the previous one until a critical thickness is achieved. Dislocations tend to find their places after a critical thickness is achieved and the phenomenon of strain relief begins. Strain relief continues to take place till the film growth continues. Such a growth mode is generally observed for epitaxial growth of oxide layers on semiconductors [49].

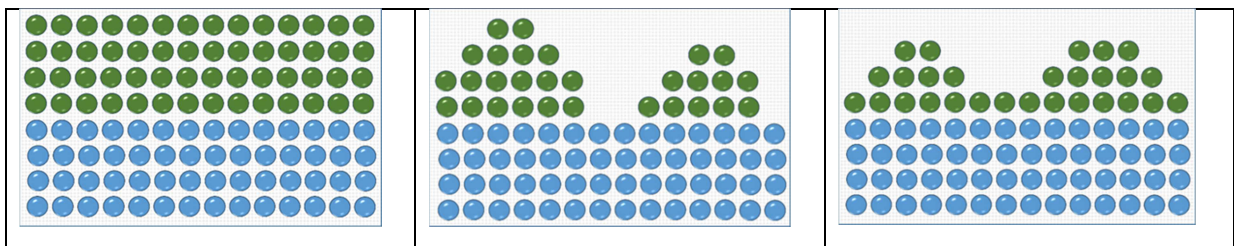


Figure 2.8: Atomistic growth of coatings structure according to various models (a) Frank-van-der-Merve (b) Volume Weber (c) Stranski-Krastov

Volume Weber growth is generally regarded as a 3D-growth of a coating system as the incoming adatoms grow in form of islands. According to Volmer-Weber model, thin films initially grow due to the initial nucleation of atoms in form of islands with various orientations. With the passage of time

these islands grow and coalescence takes place to form a network. The film grows till the substrate is completely covered with such islands and thickening of coating takes place [50].

The Stranski-Krastanov growth is generally observed in heteroepitaxy which generally takes place due to the lattice mismatch of two different materials. Similar to the previous section, a thin film generally grows in a layer by layer fashion till a critical thickness is achieved. Deposition of a film after the critical thickness is achieved is followed by 3D island growth which is generally known as Stranski-Krastanov growth in literature. Such a type of film growth can be influenced by using a suitable coating temperature, coating deposition rate etc. [51]. A comprehensive analysis on the stress produced due to Stranski-Krastanov film deposition is made by Othman et. al. He simulated that an increase in total stresses in a film has an exponential increase with the increasing coating monolayer. He also proved that an increase in lattice misfit results in high lattice strain within the coatings [52].

2.4.2. Structural Models

In order to understand the relationship between various process parameters used during the coating process, various structure zone models have been proposed. These parameters show a relationship between process temperature, pressure, substrate voltage, ion energy etc.

Movchan and Demchishin (1969) were among the first scientists who gave a detailed overview of the coating growth of evaporated films. They proposed a ratio T/T_m (homologous temperature) in order to define various phases which are generally observed during the deposition process T is defined as the deposition temperature whereas T_m is defined as the melting temperature of the coating material. They classified the structural zone diagram in three different zones (Fig.2.9).

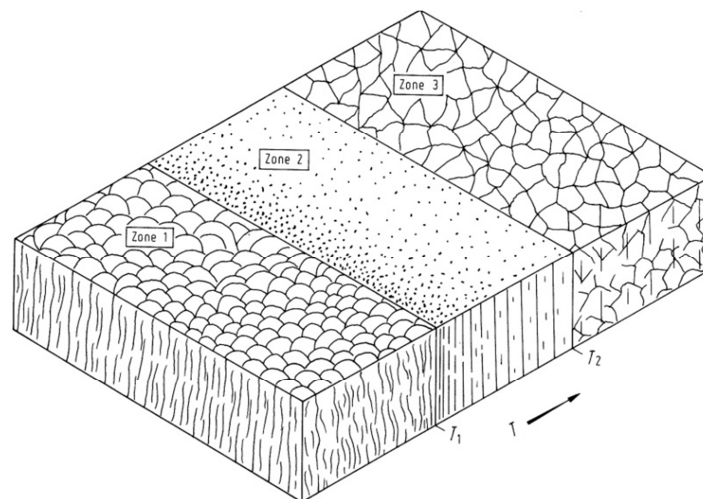


Figure 2.9: Structure Zone Model proposed by Movchan and Demchishin [53]

Zone 1 is a region where low admissibility of atoms takes place with $T/T_m < 0.2$. This type of coating structure is generally achieved by deposition of coatings at low temperature which results in low

admobility of atoms and low rate of nucleation of grains. Deposition process like CVD allows shadowing of atoms as there is oblique deposition of ions on the surface. The result is a fine grained coating structure and the direction of the coating deposition was proposed to be in the direction of arriving vapor flux with domed tops [54]. Such coatings are highly porous and with high lattice defects at the grain boundaries [55].

	Zone 1	Zone 2	Zone 3
Metals	< 0.2	0.2-0.4	> 0.4
Oxides	< 0.26	0.26-0.45	> 0.45

Table 2-2: Schematic of Structure Zone Model proposed by Movchan and Demchishin

The transition zone (Zone 2), defined by T/T_m in the range of 0.2-0.4, is achieved by depositing at high temperatures. Surface diffusion is considered to be the major process controlling the grain growth in this zone. The coating growth is of columnar nature and the grain size increases with the increase of T/T_m ratio [55]. These grains are separated by intercrystalline boundaries and the surface structure is believed to be smooth and dense [56]. Zone 3, growth occurs at homologous temperatures above 0.4. High admobility with a strong tendency in nucleation takes place during the deposition. Grain boundary migration plays a vital role in the growth of coatings. During this stage, coalescence of grains with various orientations takes place leading to grain coarsening. This restructuring allows mobility of grain boundaries to a position generally perpendicular to film plane. The size of the grains increases with increasing temperature too and they tend to orient themselves in the same order [57].

Thornton (1974) analyzed 25- 250 μm thick Ti, Cr, Fe, Cu, Mo and Al coatings and found that a third parameter along with homologous temperature is responsible for the different structural growth in coatings. Therefore, he proposed the addition of another dimension (sputtering gas pressure) to the Movchan and Demchishin model resulting in four different zones [56, 58]. Unlike Movchan's structure zone model, four different coating growth zones (Zone 1-Zone 3) depicted in Fig. 2.9. Zone 1 defines the growth of coatings at extremely low temperatures (below 0.1 T_m). Here the admobility of atoms is very low and hence low nucleation takes place. No coalescence neither grain migration takes place. In this zone substrate roughness as well as and texture play a vital role as the behavior of nucleated atoms is influenced by the substrate [59]. The coating grows generally in form of fibers (diameter: 1-10 nm), often found in bundles [57]. A competitive structure growth takes place in Zone T. The grains start to grow parallel at the substrate interface but proceed to grow in V-shape as the coating thickness increases. Due to low temperature a self-diffusion of atoms on the substrate takes place with low boundary migration [57].

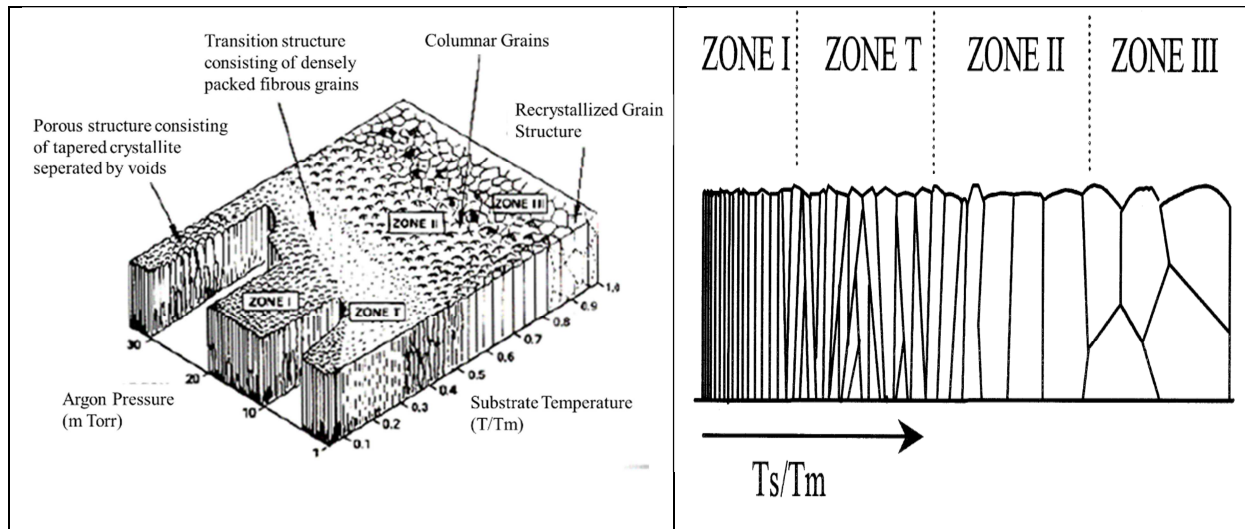


Figure 2.10: Structure Zone Model proposed by Thornton for sputtered metal coatings [60]

A similar growth of coatings as described by Movchan, has been presented by Thornton (Fig. 2.10) in Zone 2 ($0.3 < T/T_m < 0.5$). Sufficient values of T/T_m are responsible for the domination of adatom surface diffusion process leading to localized epitaxy followed by columnar growth of crystals [61]. These crystals are generally separated by dense intercrystalline boundaries. In case of high adatom diffusion, crystal formation takes place in form of platelets and needles. Such structures are generally found to be porous in nature. The growth of these coatings is dependent on the lattice absorption probabilities, surface diffusion characteristics and the crystal face condensation probabilities[56]. The transition of surface diffusion (Zone 2) to bulk diffusion as well as recrystallization (Zone 3) allow an equiaxed grain growth of coatings [61]. The structural behavior of coatings is generally influenced by the adatom mobility. At low deposition temperatures a negligible or low adatom mobility is observed resulting in amorphous coatings. With the increase in temperature high mobility of adatoms takes place allowing the atoms to grow in forms of valleys and hence a columnar structure takes place. Further increase of deposition temperature causes the annealing of coatings and such coatings act as a bulk material. Dense grain, twin boundaries and grain shapes that do not coincide with the substrate and coating surface topographies are some of the characteristics of the coatings in this zone [61].

Meisser investigated coating growth of TiB_2 , WO_3 , BN, SiC etc. and found that the coating growth due to low mobility adatoms lead to various column sizes in Zone 1. The energy change in the adatoms has been induced by applying a substrate potential (V_s) whereas Movchan and Thornton discussed the adatom mobility of atoms in relation to pressure and high temperatures. In contrast to other Structure Zone Models he also discussed that the area of Transition Zone can be increased or decreased by influencing the substrate voltage [62].

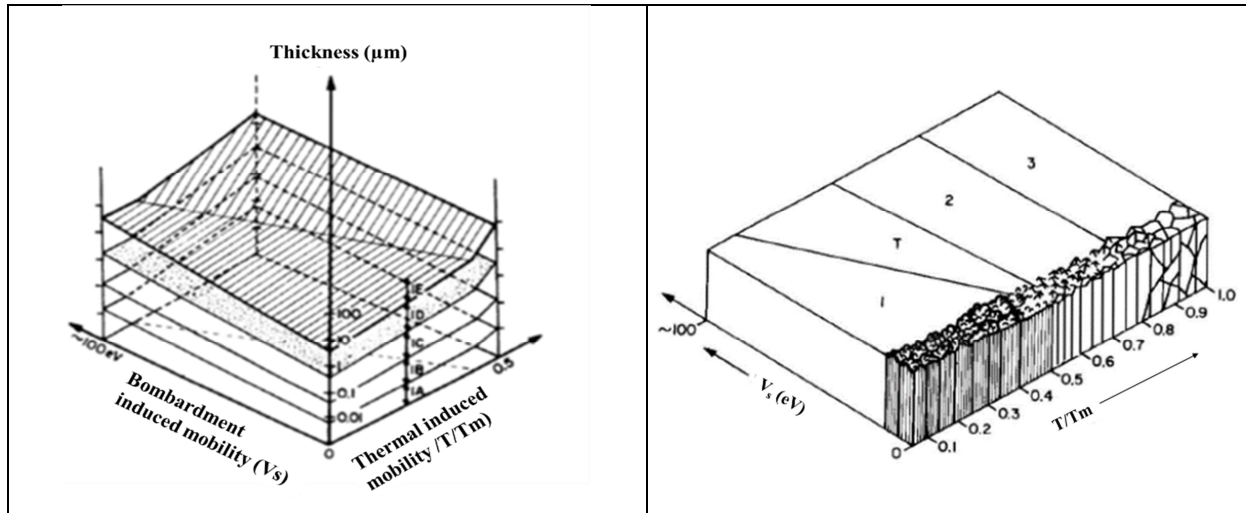


Figure 2.11: Sturcture zone model proposed by Meisser et. al. [62]

According to Meisser (Fig. 2.11) Zone 1 can be further classified in subzones (Zone 1A-1E). Zone 1A represents the grains with column size of 1-3 nm, 1 B with column size of 5-20 nm, 1C shows column size of 20-40 nm, 1 D represents column size of 50-200 nm and 1 E has a column size of 200-400 nm. He interpreted that a growth of film is a non-linear process and is therefore plotted on a logarithmic scale. The boundaries drawn between the different zones show dominant change in column sizes of the coating. He also postulated that the coating structure is a function of the thermal and bombardment induced mobility which can be influenced by substrate potential (V_s). Hence he proposed an additional parameter along with the parameters discussed by Thornton und Movchan for detailed investigation of the coating structure.

2.5. Erosion resistant coatings

2.5.1. Single layer Coatings

Various metallic nitride/carbide/boride monolithic coatings have been used in past for applications against particle erosion. Single layer coatings should be able to show enough hardness and fracture toughness to be able to stand the indented load used for that conditions [63]. Literature indicates a number of monolithihic coatings used for the applications against erosion Table 2-3.

Substrate	Coating	Angles	Velocity	Reference
OT4-1-Titanium alloy	V, ZrN, TiN, MoN, CrN, NbN	20,70	80m/s	S. A. Muboyadzhyan [5]
Ti64	TiAlN	30,90	70-150 m/s	Levy and Buqian [63]
Ti64	CrTiAlN, TiN	15-90	60 m/s	Yang. et. al. [6]
Polymer (CFRP)	Ti, TiN, Cr, Al	20, 90	65m/s, 95 m/s	Maurer and Schulz [64]

IN718	Cr ₂ AlC	30,90	Not available	Schroeter [65]
Ti64	TiSiC	30,90	84 m/s	Wei et. al. [66]
W-Substrate	Diamond Coatings	90	33-268 m/s	Wheeler and Wood [67]

Table 2-3: Literature analysis of investigated monolayer coatings for erosion applications

During the last decades monolithic diamond coatings achieved their popularity for use in erosion applications. Monolayers with inclusion of small nanocrystals of hard transition nitrides within hard layers (e.g. W₂N or TiN) leading to further increase in hardness and improved fracture toughness of the coatings is often used for wear applications. The wear rate of such a coating is approximately 4 times less than the conventional TiN coatings [68]. Literature also indicates a limited use of single layer coatings for wear applications. A single layer coating are generally composed of a material with common properties and does not have the potential to react differently due to the various material removal process taking place during the material removal process. On the other hand, multilayer coatings is an overlapping of various layers where a transition of properties can be observed provided by each single layer [69].

2.5.2. Multilayer Coatings

Multilayer coatings seem to be popular during the last decades due to their structural stability during the erosion process. The coating should consist of two or more different layers with various crystal structures, various hardness, Elastic Modulus etc. The first layer should be able to provide high toughness and should have a high load bearing capacity that no cracks can be induced in the coating. Once the crack has been induced, the crack should propagate till the interface of the two layers is reached and should deflect at the interface. This would decelerate or prevent further crack propagation into the second layer and resistance against erosion can be obtained. Once, the crack is initiated into the second layer, this layer should have the capability to deform plastically in order to improve the plastic deformation capability of the entire coating [70]. Such an effect is generally achieved by combining a hard phase (metal nitrides/carbides) and a soft phase (metals) within a coating system. Table 2-4 suggests some of the possible multilayer coatings deposited for wear applications.

Substrate	Coating	Angles	Velocity	Reference
Ti64	TiN/TiN _{1-x}	20,90	90-100 m/s	Feuerstein et.al. [71]
Ti64	W/WC	30°-90°	240 m/s	Quensnel et.al. [72]
Ti64	W/WN	30°, 90°	396 m/s	Gachon et. al. [7]

AISI 4140	TiCN/TiNbCN	30 °	-	Aperador et. al. [73]
-----------	-------------	------	---	-----------------------

Table 2-4: Literature analysis of investigated multilayer coatings for erosion applications

Literature indicates two theories used to explain the various wear phenomenon taking place during the erosion process: elastic and elastic-plastic. According to elastic theory, the hertzian cracks are responsible for the initiation of erosion process within a coatings. Therefore, the coatings should be hard enough with a high load bearing capacity in order to avoid crack initiation during the impact process. The elastic-plastic theory refers to the tensile stresses after particle impact which lead to lateral crack propagation within the coatings [74]. Hence both of the above defined models refer hardness, elastic modulus and fracture toughness of the coatings as the key parameters which define the erosion resistance of a coating. Hence the combination of metallic and ceramic layer would lead to a higher hardness and fracture toughness of the coating than in a monolithic metallic or ceramic layer.

2.5.3. Design of an erosion resistant coating system

A number of studies have been conducted in past to find the optimal design for the use in wear/erosion applications. A model discussing most of the important properties for an optimal coating design is referred in Fig. 2.12. The devised model represents four different parts of a coating system which influence the wear behavior of a system. These parts include properties of: 1) the surface of the coating 2) the mechanical and chemical properties of the coating 3) processes at the interface between coating and substrate 4) the properties of the substrate. An elaboration of each of the above mentioned factors is discussed in the next section.

Contact mechanics points to the fact that high surface stresses lead to high wear of materials. Hence, high surface finish/roughness is considered as an important factor influencing the wear of surfaces. During wear of the coating, a crack generation in regions with high surface stresses is likely to nucleate more quickly than in a region with low or no stresses. The result is stress relaxation of stresses in the surface. The crack propagation in such regions is very fast leading to large flakes or chip formation. In the later stages, the induced cracks interact with each other resulting in fragmentation of coatings in large pieces [75].

Hardness and Elastic Modulus are the most discussed mechanical parameters for the design of optimal coatings for applications in wear. The toughness of the coating is dependent on Hardness and E-Modulus of the materials. Holleck and Schier [70] introduced a comprehensive idea of interface toughening of a multilayer coating. Such coatings are composed of two different materials containing different crystal structure, Hardness, E-Modulus etc. The first layer is resistant to the impact and due to its properties phenomena like interface toughening take place. Once the crack is generated the crack propagates till the interface between the two coatings and reduced crack propagation takes place [70].

Coating thickness is also defined as an important parameter influencing the behavior of the coating in a particular application. Simulations revealed that TiN ($E=300\text{GPa}$, $H=23\text{GPa}$) seems to have a poor erosion resistance when the coating thickness was below $8\mu\text{m}$. A fracture toughness of $5\text{ MPa}\cdot\text{m}^{1/2}$ was calculated to be ideal for erosion applications [76].

Simulation results suggested that the stress generated at the film substrate interface is responsible for the adhesion of the coating on the substrate. Since both normal and shear stresses contribute to the removal of the coating from the interface, a precise knowledge of the possible stress generation after the coating process would optimal design of the coating system. Moreover, the elastic mismatch between the film E_{film} and the substrate $E_{\text{substrate}}$ leads to stress generation at the interface too. These stresses influence not only the adhesion but also the coating growth, mechanical and chemical properties, fracture behavior of the coating, texture etc. Hence, optimal combinations of substrate and coatings, defined coating thickness along with optimized coating parameters would allow the coating designers to achieve better interfaces for the support of coating structure [77].

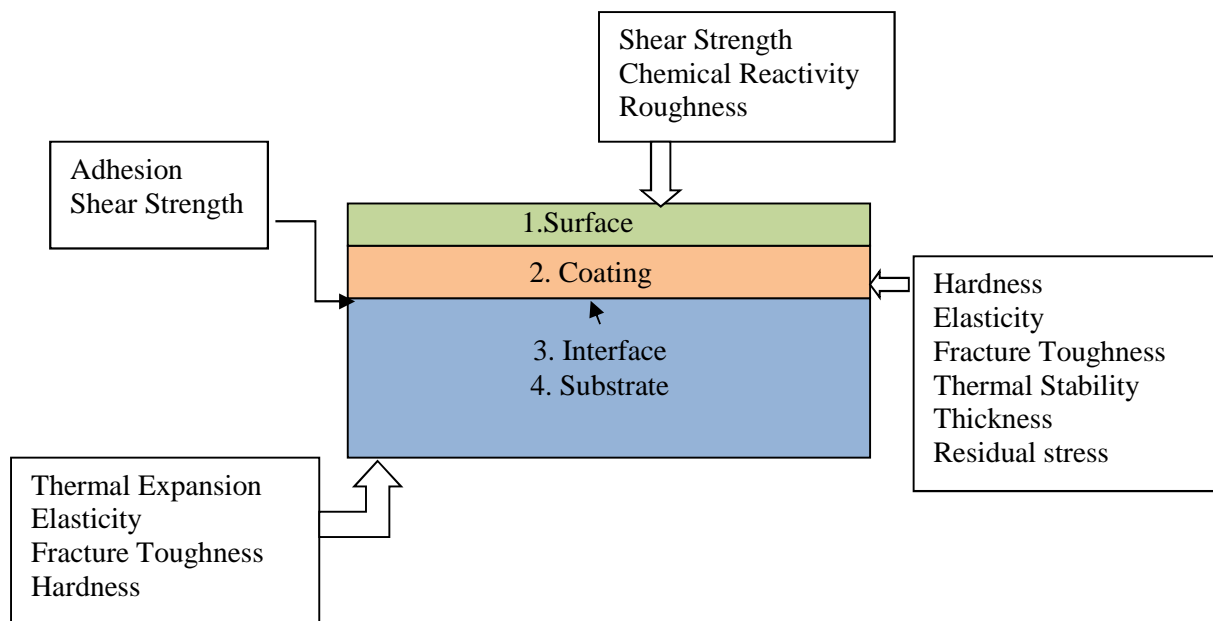


Figure 2.12: A schematic of the important components for the design of an erosion resistant coating

The importance of properties and structure of the substrate is very often studied in the semiconductor industry. WO_3 films were deposited on Al_2O_3 substrates with different molecular structure. Variation in the substrate structure was found to lead to the difference in the coating structure and conductivity of the WO_3 films [78]. An effect on the mechanical properties of a TiN coating due to the variation of substrate material was discussed by Han et. al. [79]. He found variations in Hardness and E-Modulus when deposited on stainless and high speed steel due to the variation in coating structure on the two metals.

3. Experimental Setup

3.1. PVD- Coating Machine and coating process description

The coating process has been performed in a PVD coating machine from CemeCon AG (Aachen, Germany) Fig. 3.1. The coating machine is equipped with a vacuum chamber with dimensions of 850 mm x 850 mm x 1000 mm. One of the two heating elements is installed on of the door whereas inlet of Argon gas into the chamber is also installed on the front door. The second heating element is situated on the opposite side of the first heating element. Two cathodes (targets) have been installed on each door opening to left and right.



Figure 3.1: PVD coater CC800/9 from CemeCon AG used for the coating of specimen

The table located in the center of the chamber can be rotated at various speeds. The distance between the cathodes and the anodes can be adjusted by the use of various distances adjusting apparatus. The process is controlled by a control panel which is installed on the door of the chamber. The process control software “DataView” has been used to design, control and visualize the performed coating processes.

Each coating process is divided into four steps: heating, etching, coating and cooling. Prior to the heating process, the chamber the equipment is evacuated to a pressure of 8mPa. After the given temperature is achieved, the etching process takes place which allows the cleaning of unwanted dirt and oxide layers from the oxide layers from the surface of the substrate. At the end of the etching process a static or rotating motion of the specimen holder is to be defined before the coating begins. Induction of reactive gas, in case of reactive gas, is needed to be defined before the coating process starts.

3.2. Coating Characterization

3.2.1. Coating Thickness Measurements

On order to measure the coating thickness a ball crater method is used. In this method a ball generally made of hardened stainless steel is rotated against the coated surface until the ball removes the coating and reaches the substrate. A diamond suspension is used as a cooling medium for the process (Fig.3.2a). The specimen is then observed under the microscope in order to observe the diameters of the substrate and coatings (Fig.3.2b).

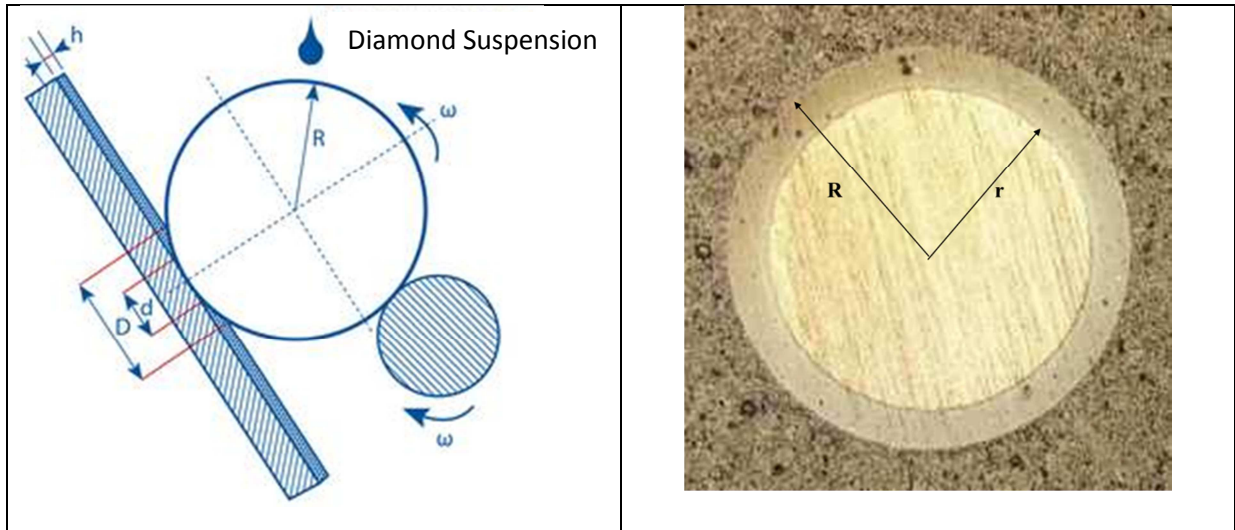


Figure 3.2: Working principle of ball crater method

A mathematical formula based on the parameters observed after the ball crater test has been defined to measure the thickness of the coating which can be found as follows:

$$h = \sqrt{R^2 - \frac{d^2}{4}} - \sqrt{R^2 - \frac{D^2}{4}} \quad \text{Equation 3.1}$$

where

h= thickness of the coating

R= Radius of the steel ball

d= inner diameter of the crater

D= outer diameter of the crater

Where d is the diameter of the substrate and D is the diameter of the coating after the ball cratering test has been performed. These tests have been performed on an equipment provided by CemeCon AG.

3.2.2. Adhesion Testing

Scratch testing is believed to be a popular quantitative technique which is used in order to address the adhesion properties of coatings and tin order to define their cohesive or adhesive nature with the substrate. A CSM Revetest® is used in the present study in order to analyze the behavior of the

coatings (Fig.3.3b). Fig. 3.3a. shows the principle working of a scratch tester. A progressive load (10-80N) is applied with a diamond tip is indented on to the coating surface and moved across the surface with a constant velocity. This method is generally used in order to determine the critical loads (L_{c2}) defining the cracking, chipping (cohesive failure) or delamination (adhesive failure) of the coatings. Coating thickness, internal stresses in the material in cases of bulk material, hardness and roughness of the coating, hardness and roughness of the substrate and friction between surface and indenter are some of the factors which directly influence the results obtained from scratch tester.

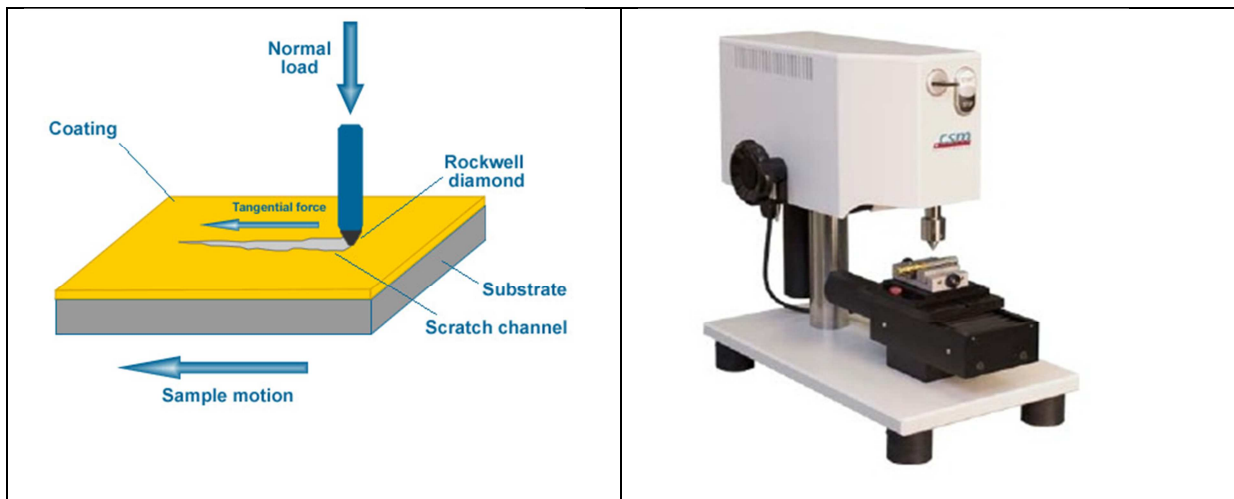


Figure 3.3: (a) Working principle of Scratch Tester (b) Scratch Tester from CSM Instruments

A microscopic analysis of the scratch allows the observer to identify the loads at which the failure of the coating takes place. A record of tangential frictional force can also be observed which allow the user to understand the coating-substrate system by the change in the coefficient of friction. An acoustic emission detector integrated in the system which is responsible for detecting the elastic waves as a result of formation and propagation of micro cracks.

3.2.3. Nanoindentation

Nano-indentation is a technology employed in order to study the mechanical properties of materials such as Young's modulus, hardness, yield stress or the buckling loadings. This method uses an indenter tip of known geometry which is indented onto a coated surface with a normal load. The load is increased to a pre-set maximum value and then the load is reduced until complete relaxation occurs. A piezoactuator is used to apply the load and the load is monitored using a control loop. The achieved load-displacement curve allows the user to determine the mechanical properties of the coatings.

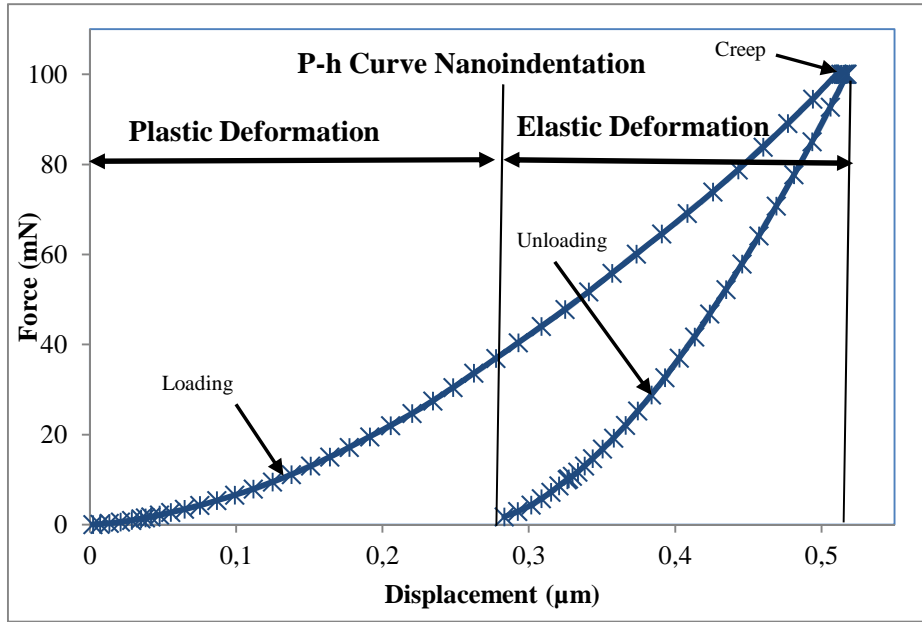


Figure 3.4: A load-displacement curve showing various phases of indenter loading

Nanoindentation measurements for the present work are being conducted on UNAT- from ASMEC GmbH. A designed software INSPECTOR X is used to analyze the properties of the coatings. A 10% rule (penetration depth of 1/10th of the coating thickness) in order to avoid the influence of mechanical properties obtained from substrate. A Berkovich indenter has been opted for the nanoindentation measurements. A Quasi Continuous Displacement Method (QCSM) method is used instead to of a conventional hardness method for the accuracy of results. In comparison to conventional method, QCSM method allow the stiffness measurement at the loading as well as unloading phase of the indentation. Therefore, the achieved results provide depth dependent results for a particular sample.

3.2.4. X-ray Diffraction

A qualitative Phase analysis of the coated specimen has been conducted with help of a BRUKER D8 DISCOVER. The instrument is equipped with a Cu K α - X-Ray Tube ($\lambda = 0.15418$ nm) and runs on a voltage of 40KV and current of 40mA. The x-ray diffractometry is based on the basic physic law of Bragg proposed in 1913 which is based on the interference behavior of the incoming and reflected X-rays used to study the system. The mathematical formulation of the Bragg Law can be studied as under:

$$n\lambda = 2d\sin\theta$$

Equation 3.2

Where n is an integer

λ is the length of the incident wave

d is the spacing between the atoms

θ is the angle between the incident and the scattering planes.

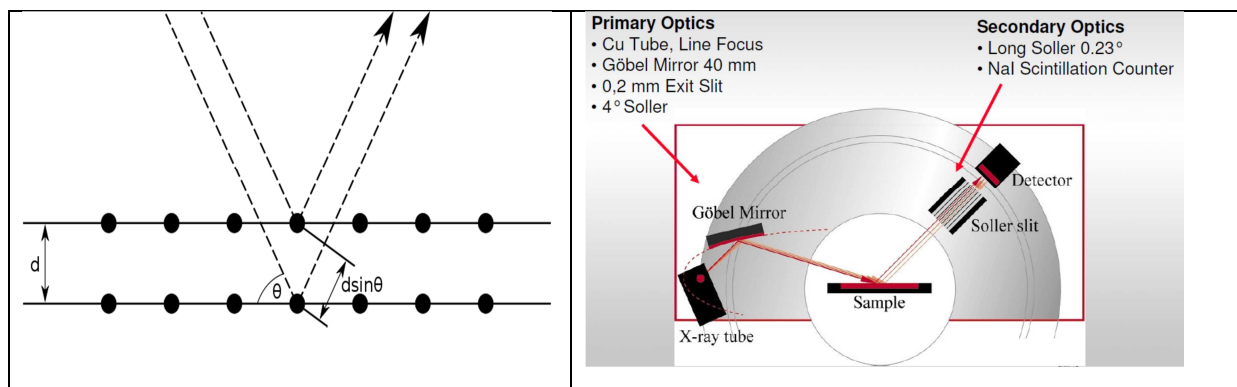


Figure 3.5: Schematic of (a) Bragg's principle based on interference of incident and reflected rays (b) Grazing Incidence X-Ray Diffractometer

A Theta-Theta combination Goniometer configuration is used for the measurement of phase analysis (Fig. 3.5b). A combination of X-ray tube, optical slits, mirrors and a scintillation counter is used for the above mentioned XRD configuration. A scintillation counter or detector comprises of a scintillator coupled with a photomultiplier or a photodiode. The scintillation counter is made of a single crystal material generally NaI, CaI or CaI_2 . X-rays in form of γ -rays are sent towards the sample which are partially absorbed and the reflected rays are sent towards the scintillation counter. The reflected rays first pass through the Soller slits where the rays are intensified and further sent to scintillation counter. X-rays absorbed by the scintillator are sent to the photomultiplier tube and are reemitted in form of electrons due to photoelectric effect [80]. The phase analysis has been performed for angles of 2θ ranging from 30° to 70° for the measurements.

3.2.5. Scanning Electron Microscopy

Scanning Electron Microscopy (SEM) has been used for the analysis of the surface structures. For that purpose a SEM from Tescan is used with an integrated EDS (Electron Dispersive Spectroscopy) for the estimation of element composition within the specimen. In order to measure Carbon or Nitrogen content WDX (Wavelength Dispersive X-rays) is used. Like EDS, WDS has also been coupled within the vacuum chamber of the SEM and have been manufactured by the OXFORD Systems.

3.2.6. X-Ray Photon Spectrometry

X-ray photon spectrometry is a widely used method for the analysis of the surface below 5 nm. XPS analysis is generally conducted with a with argon ion etching as it disrupts the chemical reduction, surface roughening, preferential sputtering etc. during the XPS analysis [81]. XPS works on the principle of emission of the atoms of their energy bands leading to emission of photons. The binding energy of the emitted atom can be estimated by analyzing the kinetic energy of the photon (E_{kin}) and the work function (W_f) which can be observed in Fig. 3.6. The energy of the incident x-ray photon $h\nu$

and BE is referred as the binding energy of the emitted electron in the material with a work function of (ϕ). The kinetic energy can therefore be expressed as:

$$KE = h\nu - BE + \phi \quad \text{Equation 3.3}$$

An excitation of the electrons with a medium energy X-rays generally Al-K α or Mg-K α is used. Ultra High Vacuum (UHV) is generally used for such type of measurements (base pressure 10^{-9} bar) in order to avoid collisions with any other foreign ion/particles present within the chamber. Quantitative element analysis of the surfaces can be estimated through the spectral analysis. Moreover, an information of the chemical states of specific elements can be analyzed through peak position and shift.

The X-ray photoelectron spectroscopy measurements were performed using SpecsLab system available at the Chair of Physics. The Mg K α X-ray emission source is used for emission of photon of energy 1253.6 eV. The XPS measurement was performed at a vacuum level of 10^{-9} mBar of pressure and the data are collected with a scan rate of 0.01eV per step with acquisition time of 1sec for each step. Measurements were conducted for Cr, N and O radicals in order to understand the formation of various phases in CrN coatings.

3.3. Erosion Testing

3.3.1. Erosion Test Rig

The erosion testing has been performed using an in-house built erosion testing rig (Fig. 3.7). The test rig consists of the three components 1) compressor 2) testing chamber 3) sand Feeder. Highly pressurized gas is achieved from the compressor which mixes with the sand particles from the powder feeder. These particles attain a high velocity after mixing with the pressurized gas and are then accelerated towards the surface.

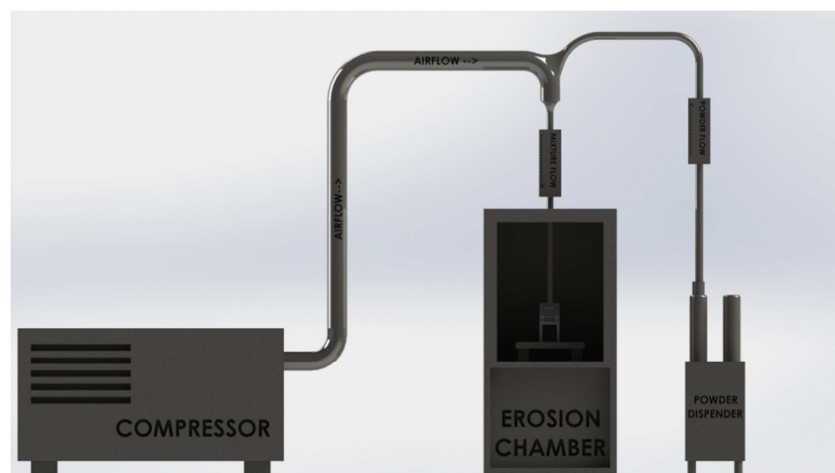


Figure 3.6: Erosion test rig showing various components

The specimen is placed in a specimen holder which can be oriented at various angles with respect to the incoming stream of particles. The specimen holder can be oriented between angles of 0° - 90° with a step change of 15° . A Sartorius measuring balance is used in order to measure the weight changes during the erosion procedure for gravimetric analysis.

3.3.2. Properties of Erodent and Laser Doppler Anemometer Measurements

The erodent used for the erosion testing can be observed in Fig. 3.7a. The particle size was found to be in the range of 75-210 μm . The hardness of the sand was measured to be 7 Mohs. The main component of the erodent was found to be SiO_2 and are found to sharp edge particles. A particle flow of 1 g/min was used for the tests and were performed at room temperature. A distance of 25 mm was kept constant between the nozzle and specimen and an incidence angle of 30° and 90° was used for the tests.

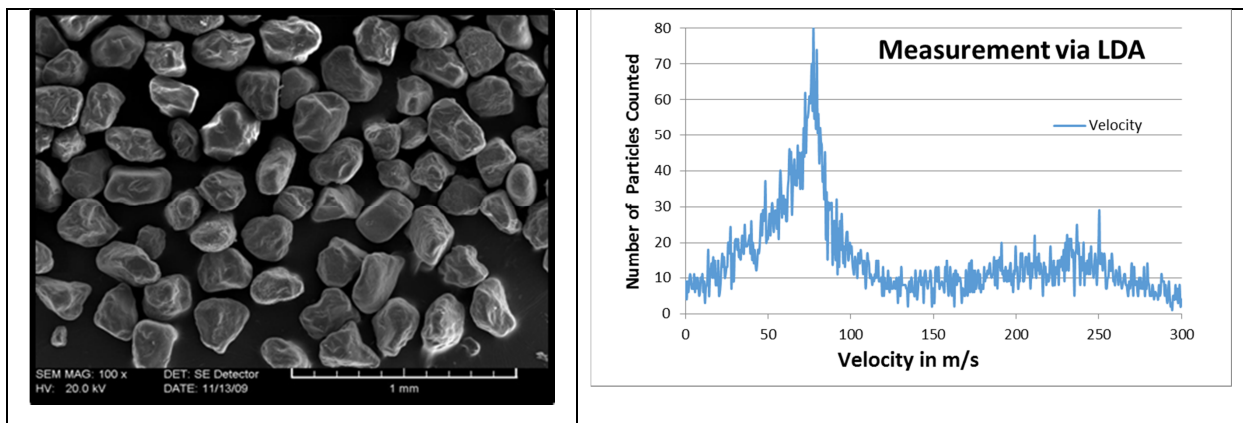


Figure 3.7: (a) SEM image of SiO_2 particles used as erodent (b) velocity measurement of particles using LDA

LDA is one of the most popular method used for the measurement of particle velocity in air. LDA works on the principle of frequency shift of the laser due to an incoming foreign particle. LDA consists of an incident light of a known frequency (ν), and a photomultiplier tube consisting of a photodetector. A small buoyant particle is seeded within flowing air, which intersects the incident light of known frequency. The scattering light is then detected by a Photomultiplier tube which generates and amplifies the current which is in proportion to the absorbed photon. The difference between the incidence and scattered light is calculated and is known as Doppler shift. A set including an 800 W laser with a wavelength of 514.5 nm connected to a band pass filter of 20-80 MHz within a signal processor and a photo detector module was used for the measurements. The data were collected with the software “FlowSizer”[®]. An analysis of the velocity measured through LDA can be observed in Fig.3.8b. It was found that a large number of particles have a velocity between 75-80 m/s. An availability of large range of particle size also lead high velocity particles in the range of 150-300 m/s.

4. Materials

4.1. Inconel 718

Inconel 718 is one of the most popular nickel super alloy with high amounts of Ni, Fe and Cr elements. This alloy finds its application in land/air based gas turbines, rockets and nuclear reactors. After a relevant heat treatment, the application temperature of the Inconel 718 super alloy lies in between -250 °C and 700 °C [82]. In addition, high tensile strength, fatigue and creep strength as well as good corrosion and oxidation resistance of the alloy has been reported due to the high amounts of alloying elements like Cr, Nb and Mo. Inconel 718 is a popular alloy for industrial applications because of its simple and easy production. Inconel 718 is also known for its highly ductile behavior and good cold forming properties [83].

Ni	Co	Cr	Mo	Fe	Si	Mn	C	Al	Nb+Ta
52.50	1.00	19.00	3.05	17.00	0.35	0.35	0.080	0.600	5.125

Table 4-1: Atomic percentage of elements in Inconel718 alloy

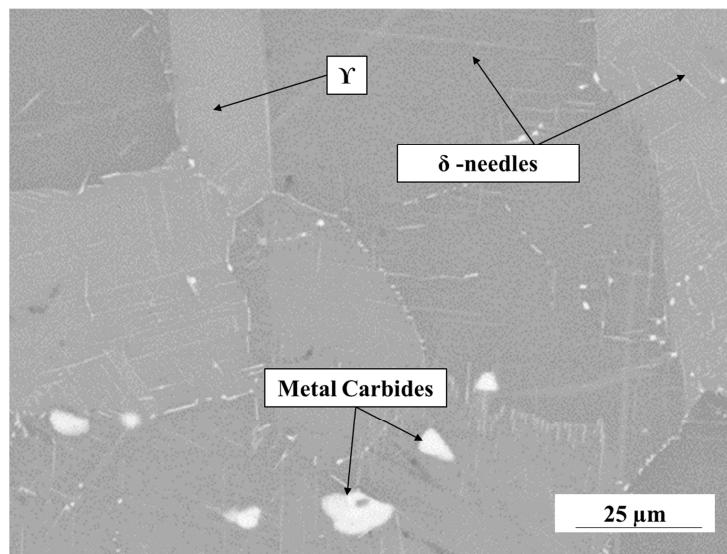


Figure.4.1: BSE image of Inconel 718 super alloy

Fig. 4.1 represents a Back Scattered Electron (BSE) image of Inconel 718 alloy. The alloy consists mainly of a γ -Ni fcc matrix. Plates like phases depict the DO₂-ordered δ (Ni₃Nb) particles and appearance of metal carbides. Moreover, γ' and γ'' precipitates are assumed to be present within the alloy but can only be detected via TEM due their small size (0.4 μm).

4.2. Chromium

Chromium is one of the metals which is often used for hard coatings like CrN, TiAlCrN and multilayer Cr/CrN [84], TiAlN/CrN, CrN/NbN [85], TiN/CrN [86] coatings etc. Some of the interesting properties of Chromium are listed in Table 4-2.

Crystal structure	bcc
Atomic Number	24
Density	7.19 g/cm ³
Molecular Weight	52 g/mol
Lattice Parameters (a = c)	2.88390 °A
Thermal expansion coefficient	4.9 x 10 ⁻⁶ m/mK
Melting point	1260-1336 °C
Hardness	6-10 GPa

Table 4-2: Properties of Chrome

In order to study the properties of Cr-coatings, these coatings were deposited with various process parameters like substrate bias, substrate frequency, cathode power, chamber pressure etc. For the discussion the effect of the cathode power has been opted here. The columns grown at 3500W are perpendicular to the surface and are parallel to each other. Such a type of column growth can be discussed using microscopic model for columnar thin films devised by Fan et. al [87]. According to them, in case of flat smooth substrate surfaces (Si-wafers) the deposited atoms prefer to arrange them in form of islands in equal sizes and hence no competitive growth between two islands take place. This results in a column growth of equal size parallel to each other. A homologous temperature (T_h) of 0.4, a columnar growth of coatings with high equiaxed grains are expected to be observed in this zone (Zone 3, Thornton Model) (Fig. 4.2).

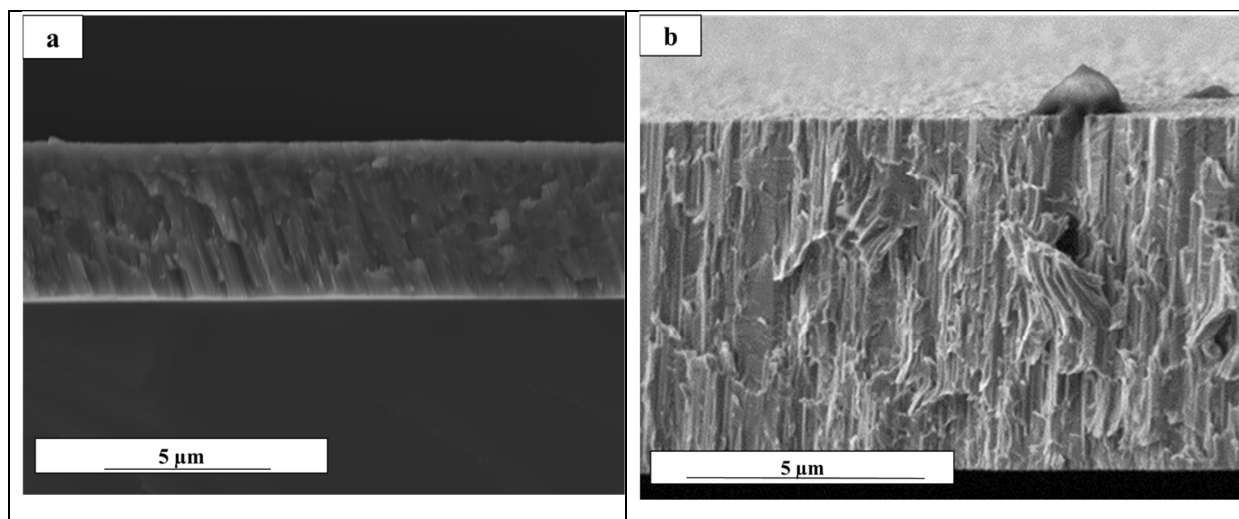


Figure 4.2: Coating structure of Cr at various cathode power (a) 2000 W (b) 3500W

A high hardness of Cr-coatings is reached for low cathode power. A rapid decrease in coating hardness with the increase in cathode power from 1000 W to 2000 W was measured. With further increase of power the hardness was found to decrease. An increase in surface roughness can be reported with the increase in cathode power.

4.3. Titanium

The use of titanium coatings in order to increase the ductility of a brittle system has often been reported in literature [88]. Some of the properties of titanium coatings are listed in Table 4-3.

Crystal structure	hcp
Atomic Number	22
Density	4.5g/cm ³
Atomic Weight	47.86
Lattice Parameter	a:2.95;c: 4.68
Thermal Expansion coefficient	8.6 x 10 ⁻⁶ m/m.K
Melting point	1668 °C
Hardness	5-9 GPa

Table 4-3: Properties of Titanium

Similar to Cr-coatings, an influence of various process parameters has been studied for Ti-single layer coatings. An influence of substrate bias on the structure of Titanium coatings is documented in Fig. 4.3. A brittle fracture has been performed for the Ti coatings in order to study the structure.

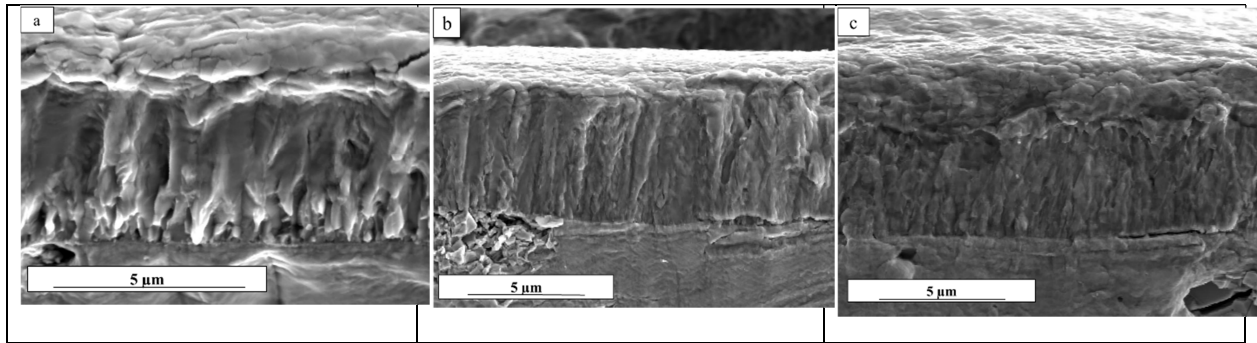


Figure 4.3: Titanium-single layer coatings at various substrate bias (a) 60 V (b) 90V (c) 120V

The coatings were deposited with a homologous temperature of 0.3. Hence, the presence of Zone T structure is expected to be available according to Thornton [60]. The presence of Zone T structure can be predicted from the available SEM images where a V- shaped and competitive growth of coatings can be depicted. At 60V, the coating column diameter is larger than at 100V and 120V. Additionally, the columns show a feathery and dense structure at higher voltages. Hence low porosity and better mechanical properties are expected at high voltages.

4.4. Chromium Nitride

An increasing popularity of the CrN coatings in various applications is due to their high hardness and low porosity. Moreover, a combination of CrN with a metallic or ceramic layer in form of matrix has been used extensively for wear applications [89]. Some of the properties of CrN coatings have been reported in Table 4-4.

Crystal structure	CrN-fcc; Cr ₂ N-hcp
Density	6.178 g/cm ³
Molecular Weight	CrN: 66, Cr ₂ N: 118
Lattice Parameter	CrN:4.14, Cr ₂ N:a=4.81130;c= 4.48410
Thermal conductivity	310 W/mK
Thermal expansion coefficient	2.3 x 10 ⁻⁶ m/m.K
Melting point	1770 °C
Hardness	12- 22 GPa

Table 4-4: Properties of Chromium Nitride

In reactive sputtering processes, the ratio between the reactive and the working gas regulates the growth of the coating, the stress and conductivity in the films, the texture, the chemical and mechanical properties of the films etc [90]. Hence, in order to obtain CrN films with required mechanical properties, different ratios of N₂ and Ar have been tested (Fig.4.4). With the increasing N₂/Ar ratio, a denser growth of the coating columns took place on Si-wafer.

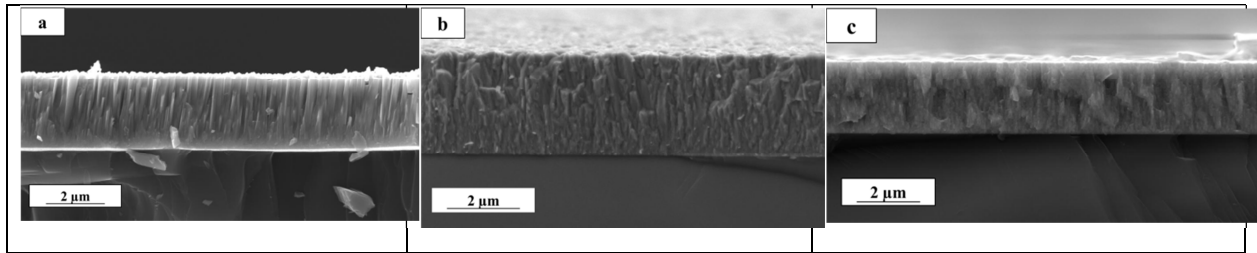


Figure 4.4: Structures of CrN coatings deposited at various N_2/Ar realtionships (a) 0.15 (b) 0.23 (c) 0.37

With the increase of N_2/Ar relation, an increase in hardness values of the CrN coatings as well as a decrease in E-Modulus can be reported. A linear tendency can be observed within the decrease or increase of mechanical properties with increase of N_2 content. The changes in mechanical properties of the CrN-coatings can be related to the avergae grain size, average residual stresses and the formation of various phases formed due to the increasing reactive gas flow rates within the coatings [91].

4.5. Titanium Nitride

TiN coatings are well known for use in various wear applications due to their high hardness. Low friction coefficient, high elasticity, high thermal and environmental stability have been identified as some of the properties of TiN coatings [92, 93].

Crystal structure	α -TiN-fcc, Ti_2N -tertagonal
Density	5.22 g/cm ³
Molecular Weight	61.91 g/mol
Lattice Parameter	TiN: a= 4.24173
Thermal Expansion Coefficient	9.35×10^{-6} m/m.K
Melting point	2930 °C
Hardness	24-35 GPa

Table 4-5: Properties of Titanium Nitride

The properties and the structure of the reactive coatings can be altered by the addition of reactive gas (N_2 gas) in various amounts. A WDX analysis has been performed in order to analyze the amounts of titanium and nitrogen using various amounts of nitrogen to argon ratios. Deposition of TiN coatings was performed with N_2/Ar ratios of 0.24, 0.47 and 0.66.

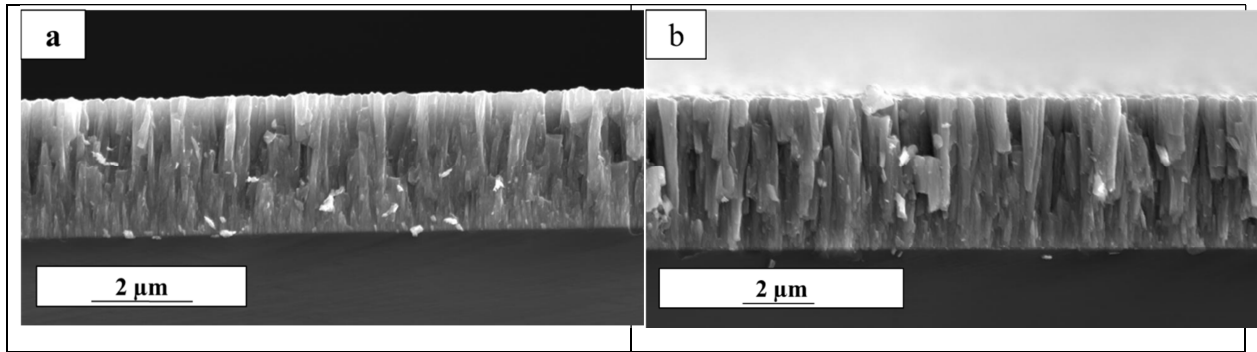


Figure 4.5: Coating structure of TiN coatings at various cathode powers (a) 6000 W (b) 7000 W

The TiN coatings were deposited with a N_2/Ar ratio of 0.66 at cathode powers of 6000 W and 7000 W (Fig. 4.5). A constant substrate bias of 90V was opted for the deposition of the coatings. From the SEM images, a large diameter of TiN columns was observed at higher cathode power. In both the cases, V-shaped of columns were observed on Si-wafer. The sputtering rates were also reported increase with the decrease in hardness of coatings with increase in cathode power.

5. Deposition Parameters and properties of multilayer coatings

5.1. Deposition parameters and coating structures

5.1.1. Cr/CrN Multilayer

The coatings have been deposited with the process parameters as described in Table 5-1:

Argon etching period	0.5 h
Chamber pressure during etching	300 mPa
Coating deposition temperature	500 °C
Substrate Bias	90 V
Cathode power	2000 W
Chamber pressure during coating	300 mPa
No. of Targets used	1
Target-Substrate distance	70 mm
N ₂ flow	60 mln
Sputtering Rate (Cr)-Static Mode	140 nm/min
Sputtering Rate (CrN)-Static Mode	100 nm/min

Table 5-1: Deposition process parameters for Cr/CrN multilayer coatings

A variation in deposition time has been observed for the multilayer coatings due to the difference in sputtering rates of Cr and CrN coatings (Table 5-1). Deposition of multilayer Cr/CrN coatings has been performed by controlling the flow of nitrogen gas during the deposition process. A gradual flow of nitrogen gas was allowed in the chamber during the deposition of CrN layer in order to avoid the lattice misalignment arising due to the addition of high amounts of Nitrogen at the Cr-CrN interface. A N₂/Ar ratio of 0.37 has been used for the deposition of coatings. The effect of the growth of CrN coating with the variation of N₂/Ar ratio was discussed in Section 4.4.

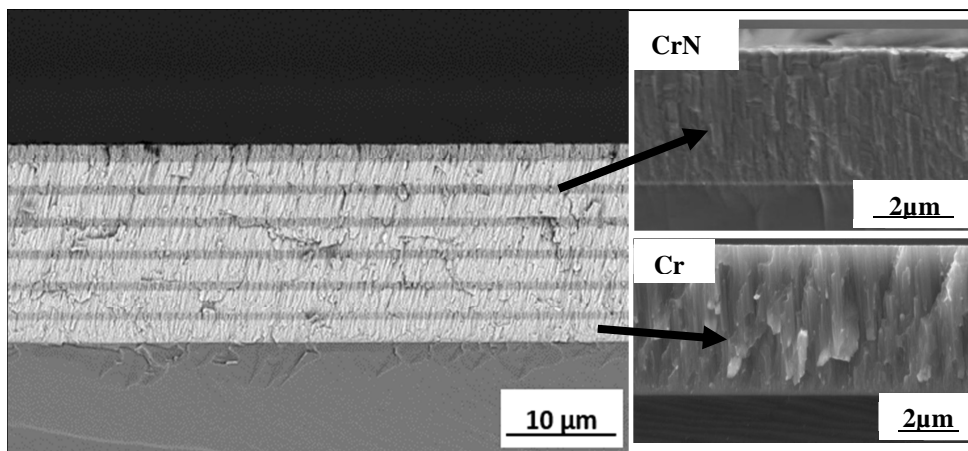


Figure 5.1: Coating structure of Cr3/CrN1 multilayer coating grown on Silicon wafer(left) individual Cr and CrN single layers (right)

growth of Cr and CrN layer, the individual coating structure in a detailed SEM image in Fig. 5.1. The Cr-coating grows in form of densely packed columns and perpendicular to the substrate and tends to orient itself at a particular angle during the coating growth. Thin CrN layers orient themselves in accordance to the Cr-coating as no clear discontinuities are observed at the interface of Cr-CrN coatings. Columnar structure of Cr and CrN coatings can also be observed in the Fig. 5.1. Cr columns are feathery, have a porous structure with large column diameters whereas CrN seems to have small width columns with low porosity. This variation in the structure can lead to positive or negative changes in the behavior of multilayer coatings which is discussed in the next section.

5.1.2. CrN/X (X=Ti, TiN) Multilayer, TiN Single layer

The coatings have been deposited with the process parameters as described in Table 5-2:

Parameters	No. of Targets	
Argon etching period	-	0.5h
Chamber pressure during etching	-	300 mPa
Coating deposition temperature	-	500 °C
Substrate Bias	-	90V
Cathode power	-	2000W
Chamber pressure during coating	-	300 mPa
Target-Substrate distance	-	70 mm
N ₂ flow for CrN	-	60 mln
N ₂ flow for TiN	-	50 mln
Sputtering Rate (Ti)-Rotation Mode	2	50 nm/min
Sputtering Rate (TiN)-Static Mode	1	66.6 nm/min
Sputtering rate (TiN)- Rotation Mode	2	30 nm/min
Sputtering Rate (CrN)- Rotation Mode	2	60 nm /min

Table 5-2: Deposition process parameters for Ti/CrN, TiN/CrN, TiN coatings

An analysis on the quality of the deposited Ti1/CrN3 (Ti:1μm/CrN:3μm) and TiN1/CrN3 (TiN:1μm/CrN:3μm) (Fig. 5.2). An SEM image of the Ti1/CrN3 (Fig.5.2a) shows that the coating surface is highly saturated with coating defects (carrots). Moreover, it seems that the grinding marks on the surface have an effect on the coating growth as the surface shows high roughness comparable to the structure of the grinding marks. In comparison, the TiN1/CrN3 coating (Fig. 5.2b) is poorly influenced by the grinding marks as a relatively smooth surface was observed in this case. The surface is not dominated by a large number of coating defects whereas the size of the defects is larger in size as compared to Ti/CrN coating. Large carrots can also be found on TiN coating surface (5.2c) but the

density of such defects is much lower than that of Ti/CrN coating and smaller in size than in the TiN/CrN coating.

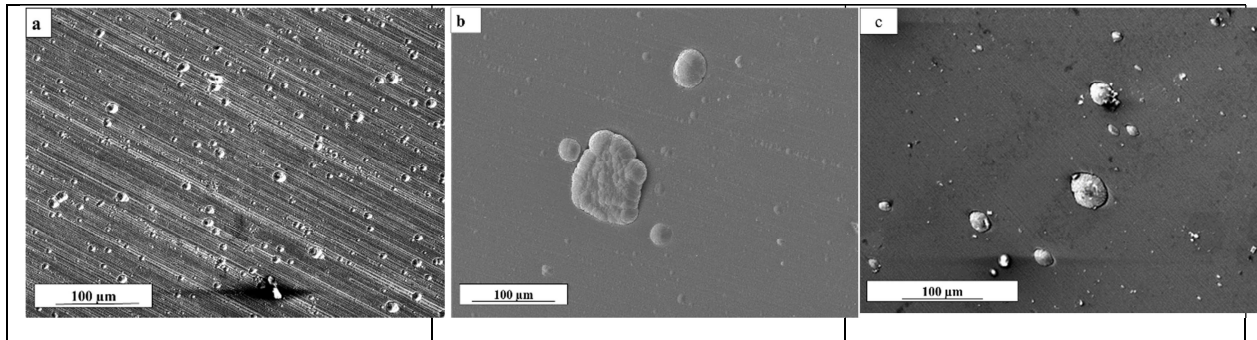


Figure 5.2: SEM analysis of surface quality of the deposited (a) Ti/CrN (b) TiN/CrN coatings (c) TiN coating

A columnar structure of the deposited Ti/CrN coating is depicted in Fig. 5.3. SEM analysis of the surface of the coating shows a surface covered with circular columns which orient themselves according to the grinding marks on the substrate. The column diameter for CrN varies between 250nm and 500 nm whereas the column diameter of Ti seems to be much smaller and fibrous (cross-sectional image). Additionally, the coating structure seem to be dense and with low porosity. No clear change in growth orientation of the deposited CrN layers on Ti layers can be seen in consecutive bilayers.

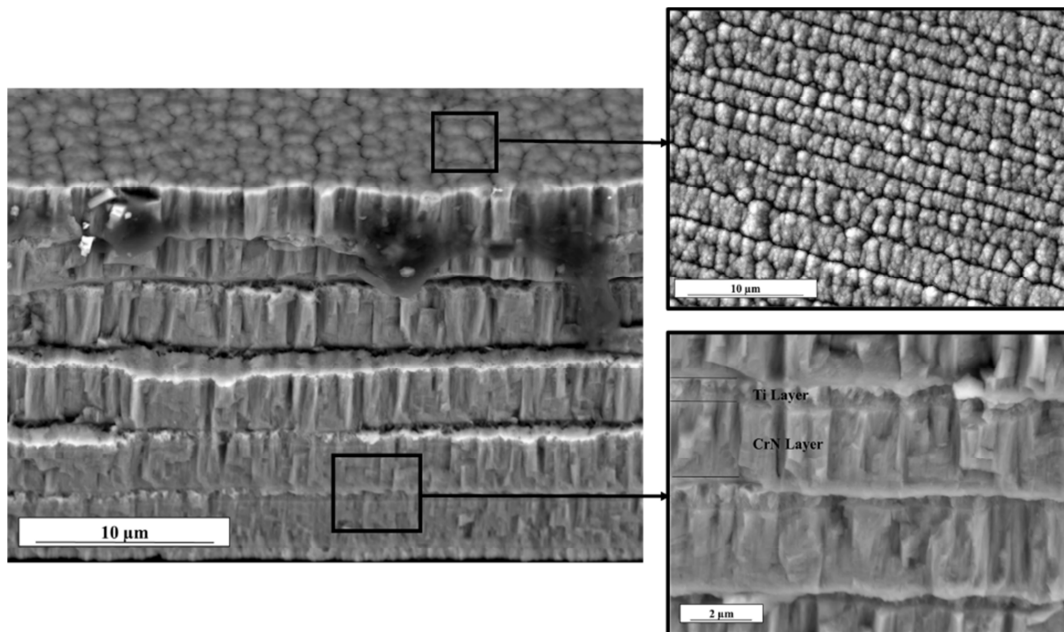


Figure 5.3: Coating structure of Ti1/CrN3 coatings showing detailed column growth on the surface of the coating and columnar structure in cross-section

In contrast, a feathery coating growth structure (also known as nodular structure) is seen for TiN/CrN (Fig. 5.4). By comparing the coating deposition of Ti/CrN and TiN/CrN, it can be observed that the addition of a metallic or ceramic component within a ceramic matrix can lead to a change in deposition kinetics of the coating growth. This would again affect the mechanical and chemical

properties of the coating. Even the change in bilayer period of a multilayer coating shows a change in coating growth and surface roughness of the coating [94].

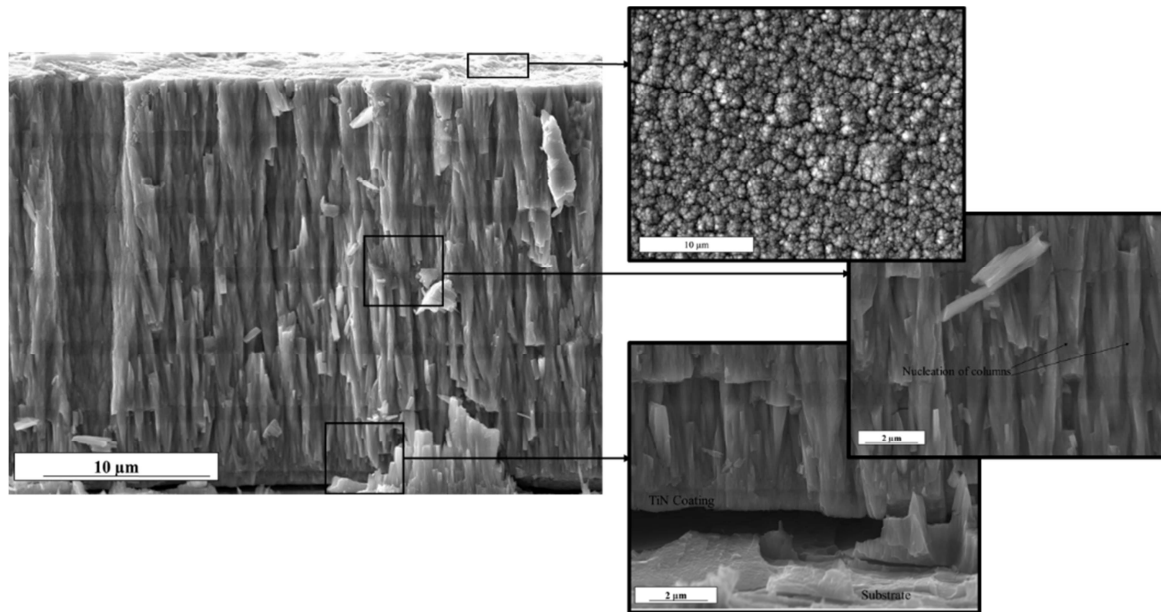


Figure 5.4: Coating structure of TiN1/CrN3 coatings showing detailed column growth on the surface of the coating and columnar structure in cross-section

The deposition kinetics of the coating supported nucleation of V-shaped columns between the coating layers for TiN/CrN coating (Fig. 5.4). This type of interruption of a continuous coating growth can lead to the weakening of the coating structure and lead to imperfections within the coatings. The formation of such V-shaped structure is the result of a competitive growth of the columns. Such a coating growth results in a preferred orientation in the coatings and an increase in roughness due to open column boundaries because of atomic shadowing [95].

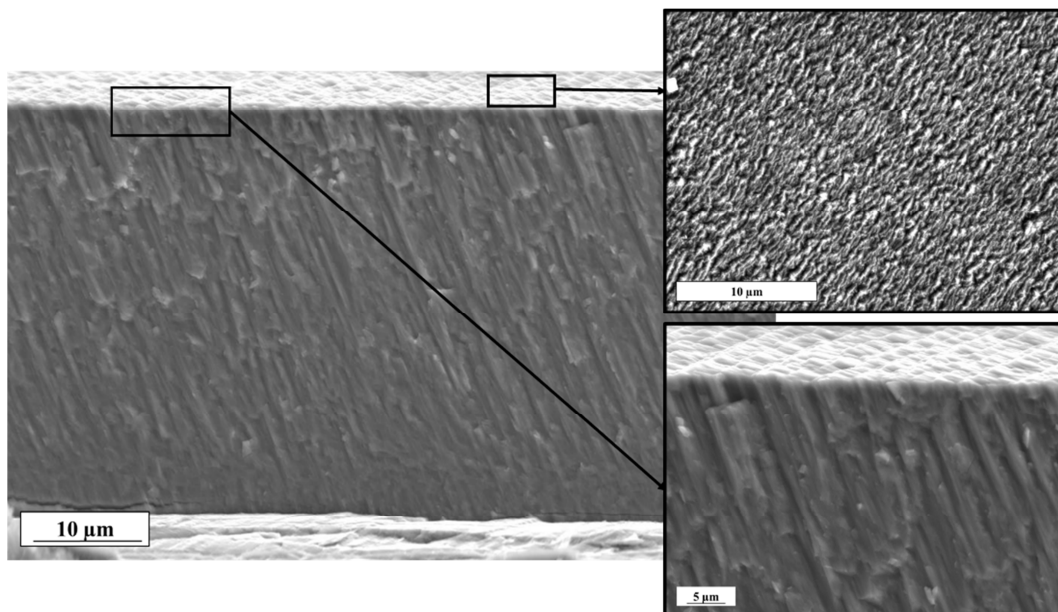


Figure 5.5: Coating structure of TiN coating showing detailed column growth on the surface of the coating and columnar structure in cross-section

In the depicted coating structure (Fig. 5.4), the first TiN layer seems to control the structure of the multilayer as no change in the structure of the later deposited CrN layers was observed. In case of reactive sputtered TiN coating (Fig. 5.5), a N_2/Ar ratio play a vital role in defining the properties of the coating. A N_2/Ar ratio has been opted in our case as it provided the best possible mechanical properties in the test series. From the cross-sectional image (Fig. 5.5c), TiN coatings grow in form of very thin columns with an orientation of about 75° with respect to the substrate having a fibrous dense structure. With a homologous temperature (T_h) of 0.17, the coating lies within Zone T as defined by Thornton (Section 2.4.2). Reactive coatings which grow in Zone T are expected to show nano or micro columns on the surface of the coatings [56]. It is expected that such coatings deposit by surface diffusion of the adatoms leading to local epitaxy and better adhesion between the coating and substrate. Additionally, due to competitive growth of columns in Zone T, a continuous change in morphology, texture and surface topography would be expected with increasing film thickness [95].

5.2. Mechanical Properties

5.2.1. Cr/CrN Multilayer

Mechanical properties of the coatings have been determined by means of nanoindentation with a load of 100 mN. Hardness and E-Modulus have been determined by analyzing the nanoindentation measurements depicted in Table 5-3. These measurements have been conducted for six different Cr/CrN multilayer and two single layer coatings, differentiated through the individual thickness of metal and ceramic coating deposited in a particular multilayer architecture. An average of 15 measurements has been used for the determination of mechanical properties. Absolute values of Hardness and E-Modulus have been selected for the calculations of H^3/E^2 in the present work.

Coating	Bimodal Period	Coating Thickness (μm)	Hardness (GPa)	E-Modulus (GPa)	H^3/E^2 (GPa)
Cr single layer	-	2.8	7.55 ± 0.43	$308,17 \pm 22.24$	0.005 ± 0.001
CrN single layer	-	1.1	20.43 ± 1.70	195.76 ± 25.17	0.223 ± 0.080
Cr1/CrN1	2	19.40	20.49 ± 0.86	319.04 ± 14.93	0.085 ± 0.013
Cr3/CrN1	4	29.21	$17.02 \pm 1,37$	282.92 ± 24.54	0.062 ± 0.018
Cr0,5/CrN0,5	1	24.11	20.05 ± 1.86	$252,97 \pm 23.73$	0.126 ± 0.042
Cr1/CrN3	4	24.23	12.40 ± 1.13	91.80 ± 7.69	0.227 ± 0.073
Cr0,25/CrN0,25	0.5	23.78	19.82 ± 1.55	298.01 ± 24.04	0.088 ± 0.025
Cr0,25/CrN03,75	4	25.35	21.42 ± 2.18	303.68 ± 30.83	0.107 ± 0.039

Table 5-3: Mechanical properties of Cr/CrN multilayer coatings

The measurements show that Cr-single layer showed low hardness compared to CrN-single layer which is expected due to the formation of hard nitride phases within the coating. In contrary, a low E-Modulus of CrN coating was measured in comparison to Cr-layer, proving CrN to be a better candidate for the load carrying capacity applications. It can be observed that in almost all coating except Cr1/CrN3 the hardness values were identical to CrN-single layer coating. Moreover, the E-Modulus of all coatings except Cr1/CrN3 rapidly increased as they were deposited in form of multilayer coatings.

In previous studies, various methods have been used to relate hardness and elastic modulus to the mechanical properties for wear applications. A famous method is the ratio of hardness and elastic modulus (H/E) which is referred to the elastic strain to failure of the coating [96]. Moreover, Johnson [97] referred H^3/E^2 as an important parameter which is associated with the coating resistance to plastic deformation. This ratio is generally used in applications for impact loading. Another parameter $(H/E)^{1/2}$ has been related to the fracture toughness of coatings [98]. Since, an impact loading has been observed in case of erosion, H^3/E^2 has been used as a characterizing parameter for the correlation of H and E with mechanical properties. This parameter is discussed detail in the next section (Section 7.3). In the present study the single layer coatings with the highest H^3/E^2 have been selected for the deposition of multilayer coatings.

5.2.2. CrN/X (X=Ti, TiN) Multilayer, TiN Single layer

Mechanical properties of Ti/CrN and TiN/CrN coatings are depicted in Table 5-4. It can be observed that the hardness values for a combination of Ti/CrN are lower than that of CrN coating single layer coatings and higher than that of Ti-layer. Contrarily, the E-Modulus values of the Ti/CrN combination increased in comparison to CrN coatings and decreased with respect to Ti-single layer.

Coating	Bimodal Period(μm)	Coating Thickness (μm)	Hardness (GPa)	E-Modulus (GPa)	H^3/E^2 (GPa)
Ti	-	1.78	6.67 ± 1.53	183.42 ± 51.52	0.088 ± 0.007
TiN	-	1.95	23.66 ± 6.00	328.43 ± 77.25	0.122 ± 0.109
Ti1/CrN3	4	23.64	15.59 ± 2.90	336.6 ± 57.3	0.033 ± 0.021
TiN1/CrN3	4	24.14	18.55 ± 2.14	376.10 ± 52.58	0.045 ± 0.020
TiN	-	24.85	23.74 ± 2.77	358.45 ± 57.3	0.132 ± 0.060

Table 5-4: Mechanical properties of multilayer and single layer coatings

In case of TiN/CrN coatings, hardness and E-Modulus are reported to be almost the same as that of thick TiN coating. It can be clearly observed from Table 5-4 that the H^3/E^2 of TiN coatings was proved

to be highest in all cases. With the addition of a ceramic TiN or metallic Ti coating with CrN coating matrix a clear reduction in the hardness for Ti/CrN and Ti/CrN multilayer coatings is measured.

5.3. Adhesion behavior of coatings

The adhesion behavior of coatings plays a vital role in determining the mechanical properties of coatings used in surface engineering applications. Literature indicates intrinsic stresses, extrinsic stresses, loading rates, substrate properties (hardness, elastic modulus), scratching speed and coating properties as some of the factors influencing the scratch tests [99, 100]. Adhesion tests for the deposited Cr/CrN multilayer coatings, Ti/CrN, TiN/CrN multilayer coatings and TiN single layer coatings has been discussed in the next sections:

5.3.1. Cr/CrN Multilayer

Adhesion of coating is one of the most important parameters which defines the wear rate of a coating system. Low adhesion of the coatings takes place due to low energy of the atoms impacting on the surface during the deposition process [101] or due to the high elastic and thermal mismatch between coating and substrate [102]. In impact applications, such discontinuities at the coating-substrate interface lead to crack generation at the interface followed by buckling or spalling of the coatings.

Scratch testing is a popular method for the determination of coating adhesion. An estimation of the adhesion of the above discussed Cr/CrN multilayer coatings on IN718 substrate is depicted in Table 5-5. The scratch tests have been performed using a progressive loading method with an initial load of 1N increasing to 80N.

Coating	Critical Load (N)
Cr1/CrN1	51.27 ± 3.265
Cr1/CrN3	45.33 ± 3.87
Cr0.5/CrN0.5	51.35 ± 1.67
Cr0.25/CrN0.25	75.1 ± 1.38
Cr0.25/CrN3.75	18.58 ± 1.11
Cr0.25/CrN0.75	43.93 ± 3.26
Cr3/CrN1	No measurements available

Table 5-5 Adhesion behavior of Cr/CrN multilayer coatings obtained through scratch tests

No clear scratch tests result can be provided for Cr3/CrN1 coating. A possible reason for unavailability of acoustic emissions can be the high proportion of metallic coatings in the coating architecture. The American Society of Testing Materials (ASTM) defines scratch test as a non-

suitable method in order to test metallic or polymeric coatings due to their failure in a ductile and plastic manner. Hence this characterization method is limited for brittle coatings [103].

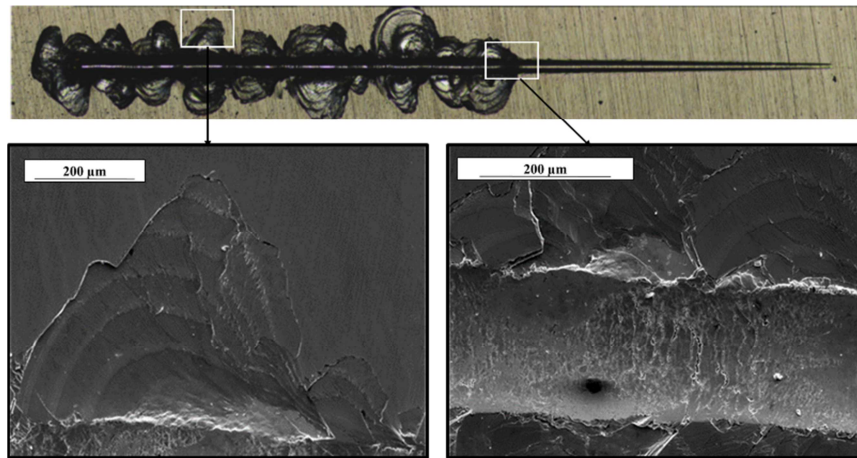


Figure 5.6: SEM images of scratched Cr1/CrN3 coating

A detailed analysis of the scratch test performed for the Cr1/CrN3 coating can be seen in Fig. 5.6. Chipping is observed within the coating of Cr1/CrN3 coating after the application of load. This type of failure is generally observed for thick coatings on soft substrates. For the adhesion test, enough stresses are needed to be introduced in order to chip the coating away from the surface. Hence during the performance of these tests high stresses are generated leading to chipping within the coating.

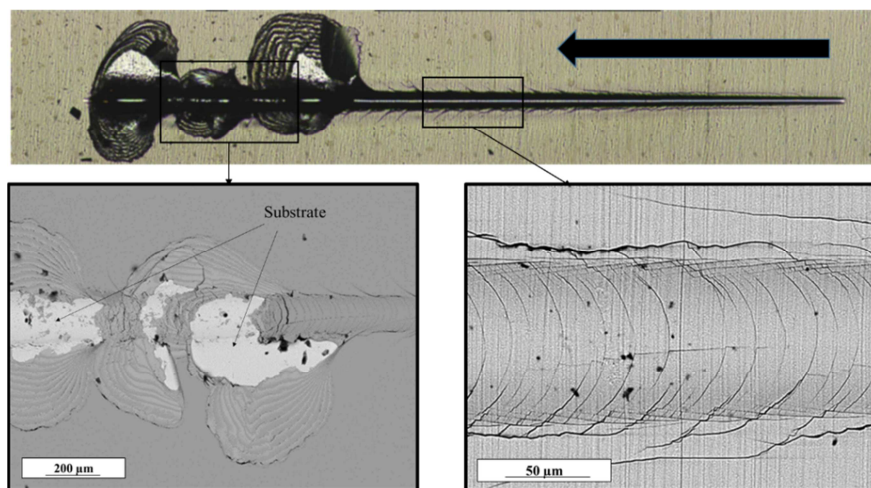


Figure 5.7: SEM images of scratched Cr1/CrN1 coating

Fig.5.7 shows a CLSM (Confocal Laser Scanning Microscopy) as well as SEM images of the scratch test performed for a Cr1/CrN1 coating. At the beginning of the scratch test a series of cohesive cracks is can be seen due to the applied load by the indenter. Such type of cracks occurs when tensile stresses are induced into the coating due to the applied force. An SEM image of the coating at Lc2 with a complete spallation of coating can be seen in Fig. 5.7b. This type of can be addressed to an adhesive

spallation of the coating as appearance of the substrate can be seen resulting due to no/low adhesion between the coating and substrate.

5.3.2. CrN/X (X=Ti, TiN), TiN Single layer

A CLSM of Ti/CrN coating after scratch testing (Fig. 5.8) show removal of coating at a critical load of 34.1436 ± 7.04 N. After the critical load is achieved a plastic deformation of the coating occurs together with complete delamination leaving the substrate behind. This type of failure is generally noticed when, the coating and substrate possess, low hardness.

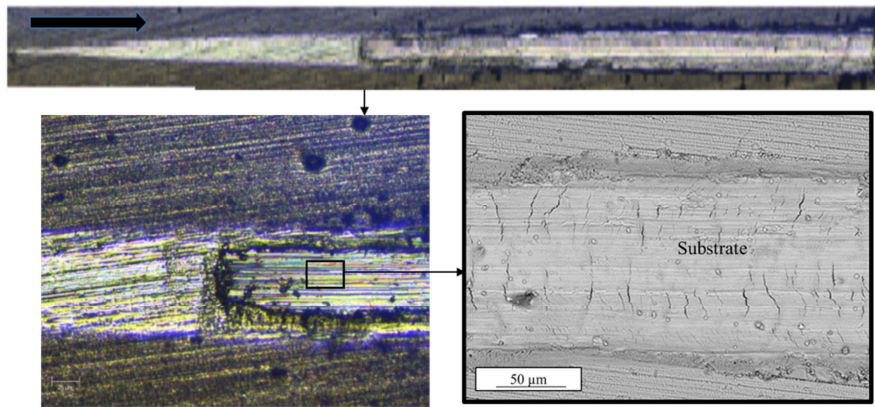


Figure 5.8: SEM images of scratched Ti1/CrN3 coating

This type of coating failure has been referred to ***gross/large area spallation*** in literature and takes place when the adhesion between coating and substrate is poor. Such coatings generally possess high residual stresses. In such type of spallation, cracks generate at the substrate-coating interface due to an interfacial flaw which propagates through the coating towards the surface with increasing load. Hence, a poor adhesion between coating and substrate is expected [104].

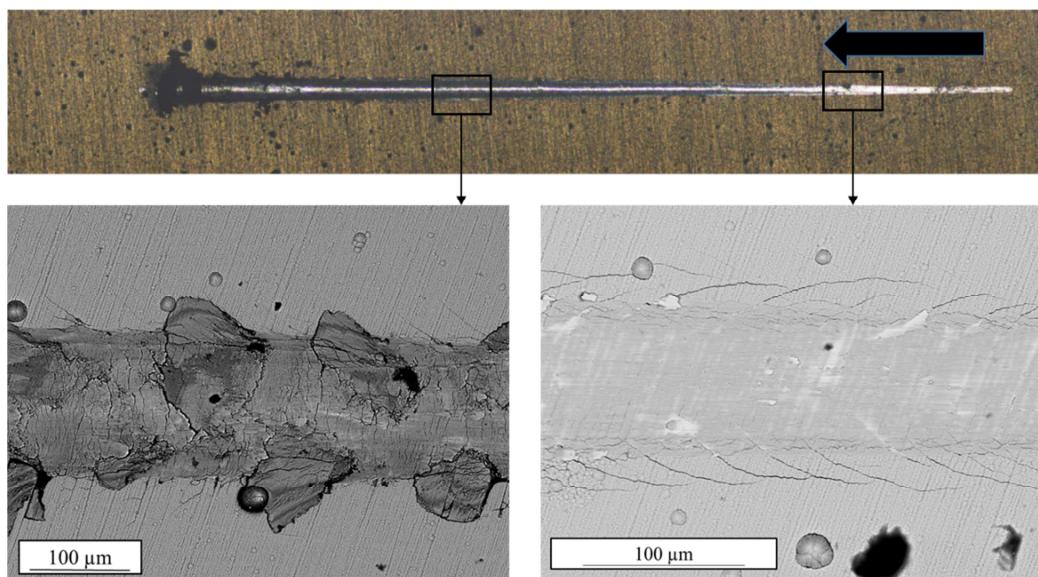


Figure 5.9: SEM images of scratched TiN1/CrN3 coating

An analysis on the adhesion behavior of a TiN/CrN coating can be observed in Fig. 5.9. At the beginning of the loading process, an appearance of cracks moving away from the direction of the scratch can be seen. Regions of the coating are removed which extend laterally from the edges of the scratch groove. Both of the mentioned forms of cracking behaviors occur when distortion within the coating takes place due to external load. Moreover, no spallation on the loading track can be detected through CLSM. Hence, a high adhesion between coating and substrate (L_{c2} : 51.76 ± 2.87 N) is reported in this case.

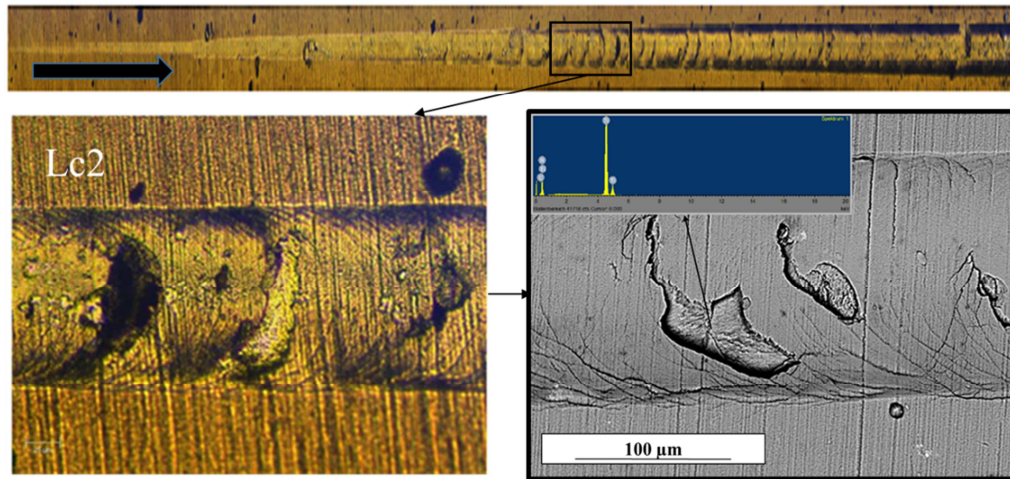


Figure 5.10: SEM images of scratched TiN coating

A series of tensile and Hertzian cracks is generally reported for hard coatings on soft substrates (e.g. TiN, CrN, TiAlN) [105]. CLSM of TiN coating on Inconel718 show a dominant appearance of tensile cracks is observed on the surface of coating. No spallation of the coating from the substrate was observed due to the available compressive stresses within the coating (Fig. 5.10). Hence, a cohesive failure of the coating can be interpreted for the TiN coating system. An EDS analysis of that those areas proved that no spalling of coating till the substrate took place. Such a failure form occurs when a good adhesion between substrate and coating exist. Cracks are first generated within the coating finding their way towards the substrate with the application of high loads [12]. A critical load of 65.67 ± 6.26 N was estimated from three measurements for TiN coatings.

6. Crystallography and XPS Analysis

6.1. Phase Analysis

6.1.1. Cr/CrN Multilayer Coatings

A crystallographic analysis of the Cr/CrN Multilayer coatings is discussed in this section. The phase analysis of the coatings would allow to understand the presence of the phases which are responsible for the mechanical and chemical behavior of the coatings. XRD analyses of three Cr/CrN coatings with a bimodal period of four (4) can be depicted in Fig. 6.1. The diffractogram of Cr3/CrN1 coating shows a combination of high intensity for the Cr (1 1 0) and low intensity for the Cr (2 0 0) peak. Moreover, the presence of Cr₂N (1 0 0) phase along with CrN (2 0 0) can also be reported in this case. In comparison, Cr1/CrN3 depicts a high intensity of fcc-CrN (2 0 0) as well as of Cr (2 0 0). Hence no formation of hexagonal-Cr₂N phase was allowed during the deposition of coating. Literature reports high hardness and high E-Modulus of coatings in presence of Cr₂N phase or in presence of CrN and Cr₂N mixture as well. The ratio of covalent bonding in Cr₂N atom is also reported to be higher as compared to CrN crystal which requires higher energy for to break the bonding in Cr₂N crystal[106]. Presence of high quantity of Cr₂N phase in comparison to CrN phase could lead to higher hardness of the coatings [5]. The calculation of binding energies as well as quantitative phase analysis of CrN and Cr₂N is discussed in section 6.1.1. In contrast to the Cr1/CrN3 coating, Cr1/CrN3.75 coating consists of combination of CrN and Cr₂N phases. The influence of the thickness of the Cr and CrN layer coatings affect the coating growth and the formation of various phases in the coating. A similar type of investigation was performed by Holleck and Schulz [107] deposited TiC/TiB₂ multilayer coatings with different bilayer periods. A presence of amorphous phase is reported at the intermixed boundary of the two layers. The single layer thickness of both components was reported to be 20nm. A partially crystalline structure of TiB₂ was reported with an epitaxial growth of TiC in [111] direction. When the layer thickness was reduced to 5 nm an amorphous TiB₂ coating was observed with TiC coating growth in [200] direction. No influence of the amorphous TiB₂ phase on the nucleation of TiC coating was detected. Formation of amorphous phases in the coating was addressed due to extreme lattice distortion during the crystal growth. Hence the coating thickness seems to influence the various phase formations as well as the presence of amorphous phases within the coating.

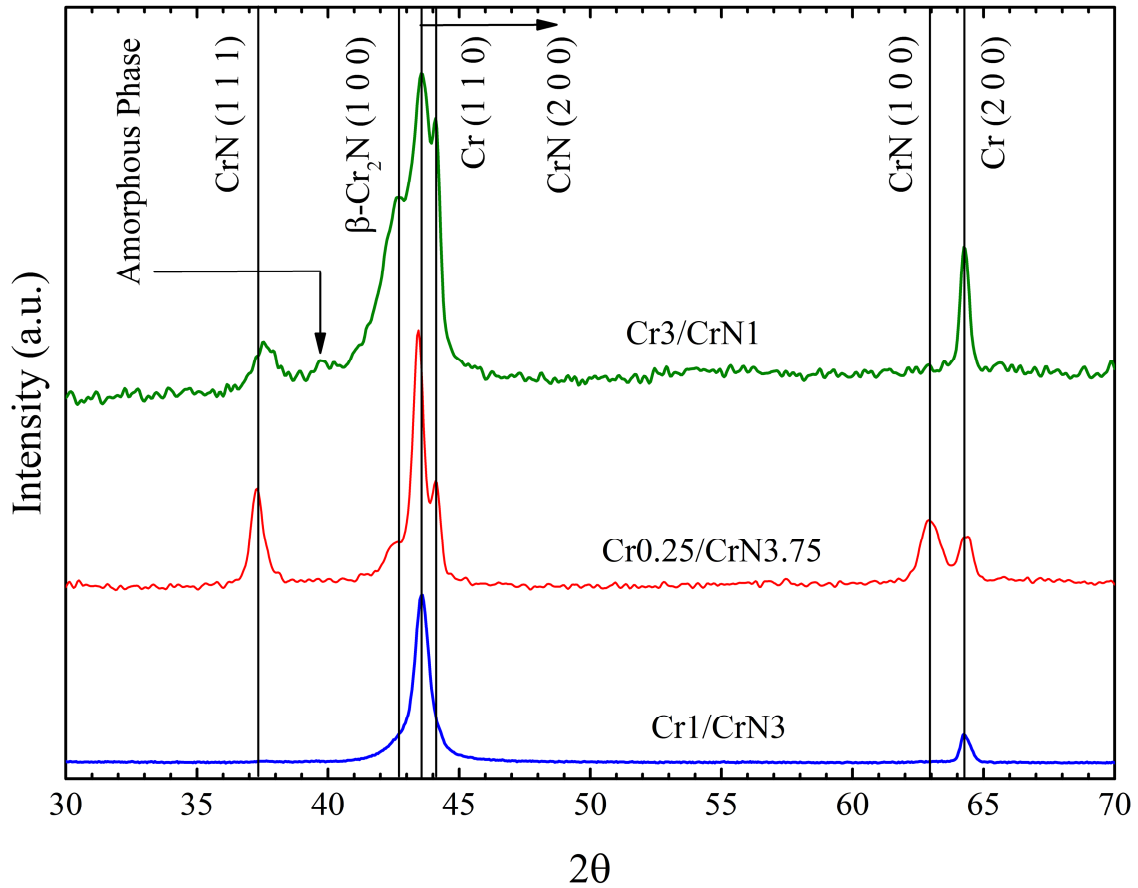


Figure 6.1: XRD Analysis of Cr/CrN coatings (a) Cr1/CrN3 (b) Cr0.25/CrN3.75(c) Cr3/CrN1

A distribution of the various phases during the deposition of CrN coating can be understood by the XPS analysis shown in Fig.6.2. This analysis was made for a CrN layer (approx. 2.4 μ m) deposited on Inconel 718 substrate. From the analysis of Cr2p spectrogram a higher binding energy is measured for Cr₂N (576.8 eV) as compared to CrN (575.15 eV) which describes the preferential formation of CrN phase in comparison to Cr₂N phase. Since the binding energy of CrN and Cr₂N phases is similar to many other phases, the evidence of the presence of the binding of Cr with N atoms (and not with F, C) can be observed from the XPS analysis of N1s orbital. Presence of Cr₂O₃ oxide (476.9 eV) shown in Fig.6.2c, demonstrates the presence of oxygen radicals during the coating process even at high vacuum of 300 mPa. The deconvolution of peaks obtained from N1s peaks allowed a quantification of CrN and Cr₂N phases which were found to be 36.4% and 63.4% respectively.

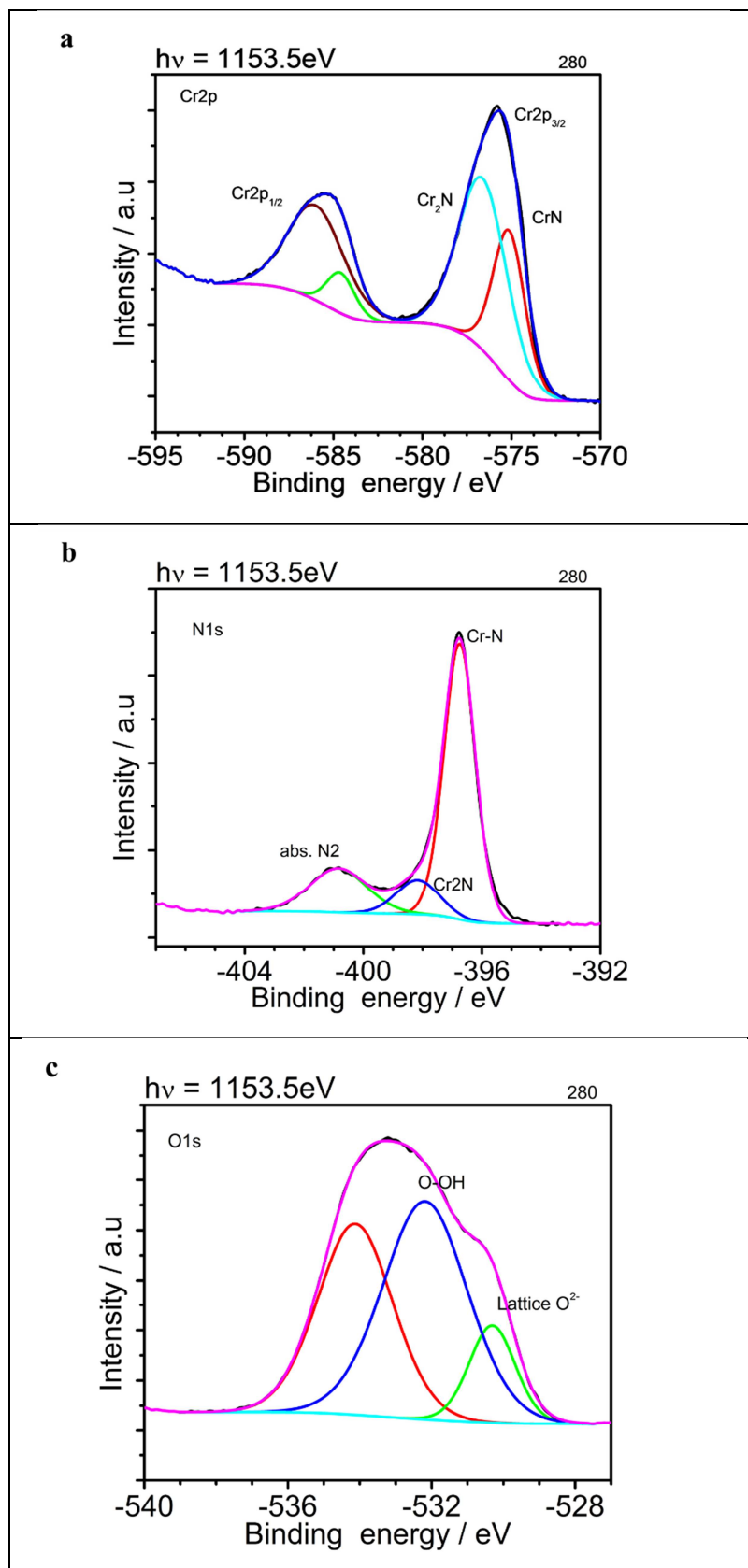


Figure 6.2: XPS analysis of the CrN coating showing various phases and respective binding energies

A note on the thermodynamic stability of CrN and Cr₂N phases was provided by Seok et.al.[108]. According to them, the Gibbs energy for the formation of Cr₂N phase is not enough at low temperatures. Thermodynamic calculations show formation of Cr₂N phase due to a eutectoid reaction $\text{Cr} + \text{CrN} = \text{Cr}_2\text{N}$ at a temperature of 430 °C. The formation of a Cr₂N phase during deposition can be influenced due to extraordinary high perturbations like high voltage bias on substrate or high deposition power. Hence the presence of stable Cr₂N phase is generally reported above 500 °C. Since the deposition temperature of the Cr/CrN multilayer coatings was also at a temperature of 500 ± 10 °C, hence the formation of a stable Cr₂N phase is not guaranteed [108].

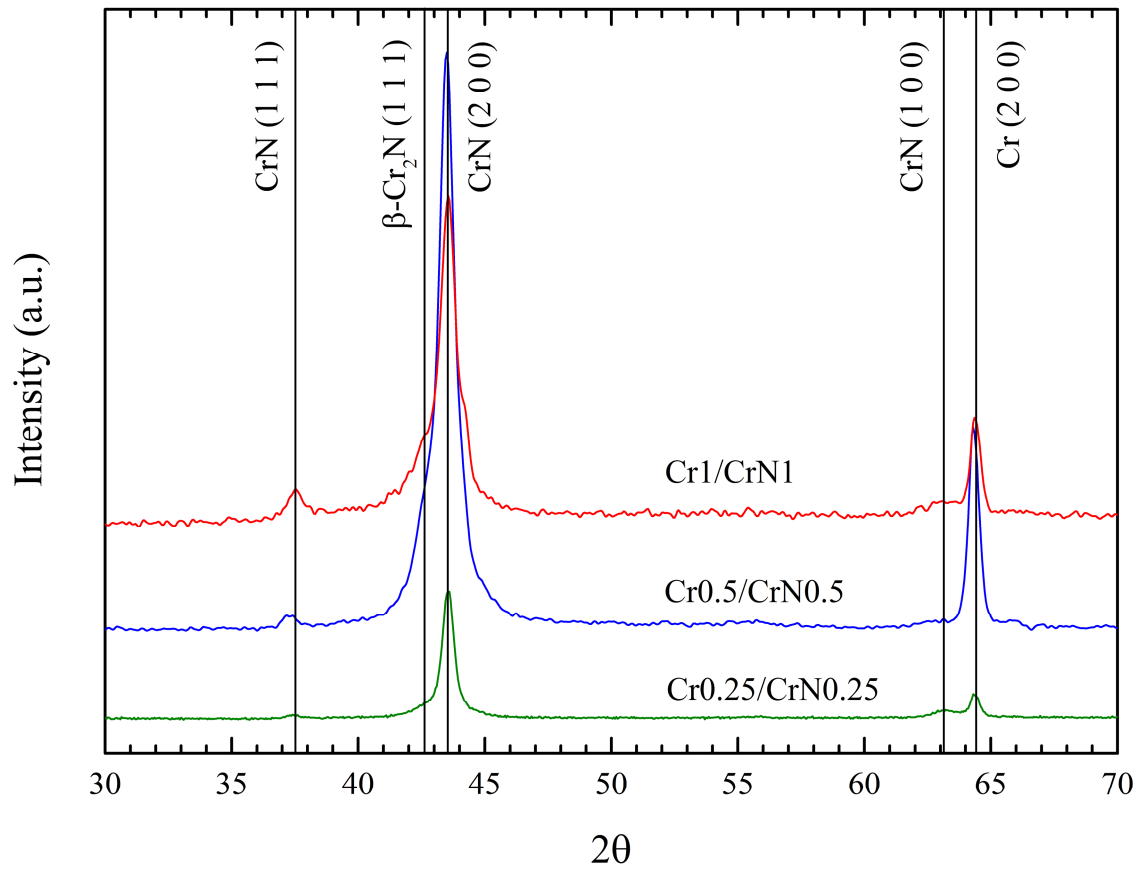


Figure 6.3: XRD Analysis of Cr/CrN coatings (a) Cr1/CrN1 (b) Cr0.5/CrN0.5(c) Cr0.25/CrN0.25

In order to study the effect of thin (nanometer) metallic and ceramic coatings, Cr and CrN coatings were deposited in a thickness range of 250nm-1000nm. Fig 6.2 for Cr1/CrN1 shows the presence of CrN (1 1 1) and Cr₂N (1 1 1) phase along with Cr-phase. A phase analysis of the Cr0.5/CrN0.5 coating show a presence of only CrN phase with two orientations (1 1 1) and (2 0 0). Presence of Cr phase is detected in all the multilayer coatings. A similar type of structure can be detected for Cr0.25/CrN0.25 where CrN phase along with Cr can be obtained from the diffractograms. Similar to Cr1/CrN3, an absence of β-Cr₂N phase was found in Cr0.25/CrN0.25 and Cr0.5/CrN0.5 coatings.

6.1.2. CrN/X (X=Ti,TiN) Multilayer Coatings, TiN single layer

The phase analysis of a TiN coating can be shown in Fig.6.4. The absorption for the TiN coating using a Copper X-ray cathode was calculated to be 3.35 μm with an assumed absorption of 90% through ABSORB DX software (Bruker AG). Only three peaks of fcc-TiN phase (various orientations) are detected from the surface. The XRD results clearly show that no Ti_2N hexagonal-phase formation takes place at these deposition conditions.

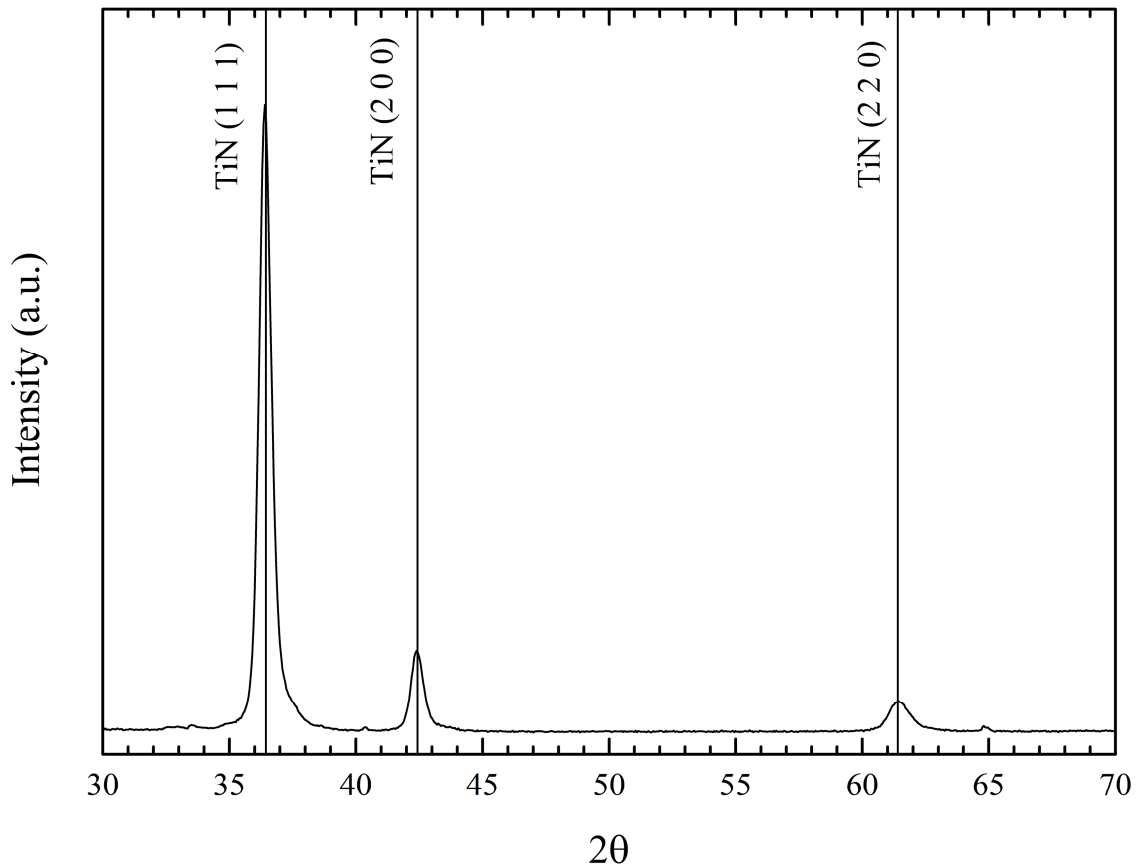


Figure 6.4: XRD Analysis of TiN single layer coating

XRD analysis of the Ti/CrN multilayer is depicted in Fig. 6.5. Since the top layer is CrN, a Cr_2N (0 0 2) phase is detected. Similar to Cr1/CrN3 coating, the deposition parameters does not favor the formation of bcc-CrN phase. Presence of the Ti_xN_y peak shows formation of possible nitrides at the CrN and Ti-layer interface. In combination with the above mentioned phases, a large number of hcp- Cr_2Ti phase were also detected. Presence of intermetallic compounds like Fe_2TiO_4 , Fe_2Ti and Cr_2Ti -phase as the possible elements causing the embrittlement in a structure and are responsible for decrease in bonding strength between two metals [109]. The availability of an amorphous phase is also detected in XRD pattern.

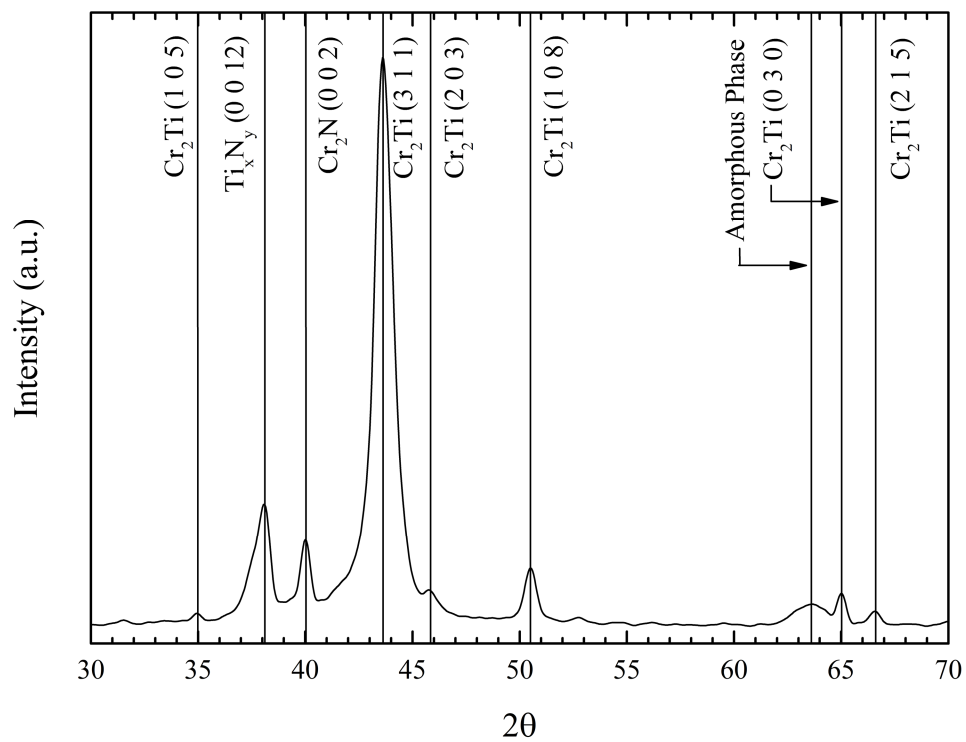


Figure 6.5: XRD Analysis of Ti/CrN multilayer coating

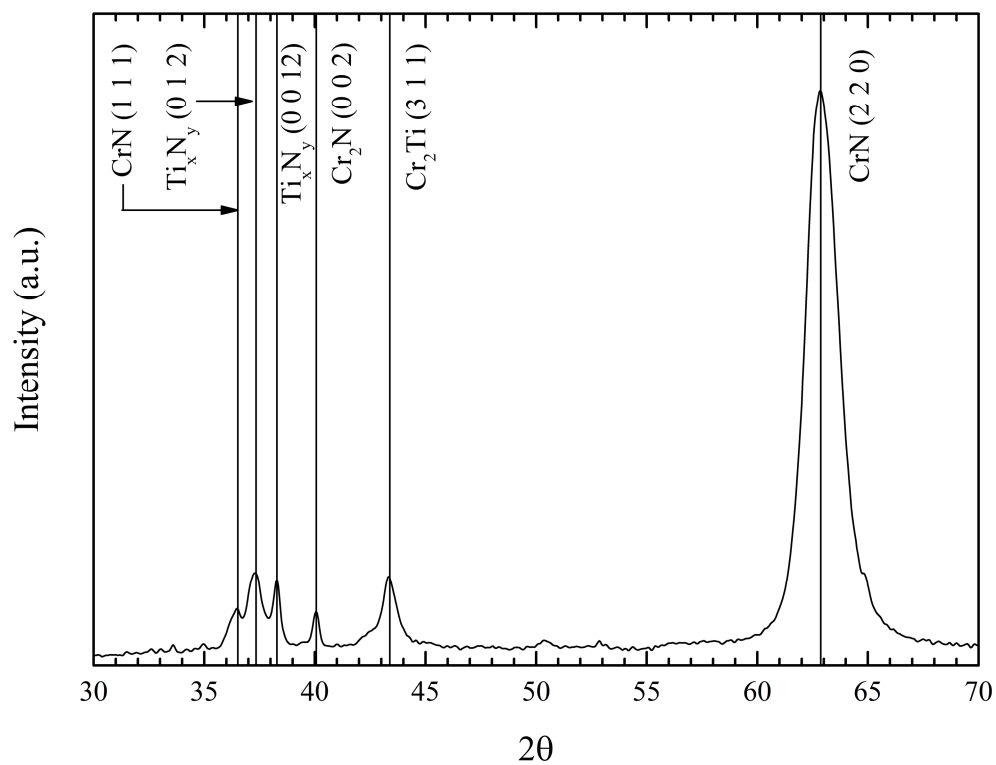


Figure 6.6: XRD Analysis of TiN/CrN multilayer coating

In contrast to the Ti/CrN coating, presence of bcc-CrN phase along with Cr₂N phase in TiN/CrN coating. Similar to Ti/CrN, formation of Ti_xN_y and hcp-Cr₂Ti phases were detected through diffractometry.

6.2. Crystal Size Determination

Crystallite Size (grain size) is generally referred to the smallest diffracting domain of a material. This should not be confused with the particle size as a particle may consist of a number of crystallites. An approach to calculate crystallite size is made in the present work in order to correlate the size of the grains with the hardness of the coatings. It is believed that by refining the grain size of one can limit the size of the pre-existing microcrack which is reported to be beneficial for the strength. On a macroscopic level, smaller grain size is less resistance to crack extension by reducing the potency of any grain bridging which reduces the toughness of the material [110]. Literature refers to two various type of dislocation processes for nanocrystalline materials. In case of crystal size lower than d_c , the deformation process takes place through small scale gliding in the grain boundaries. In case of d_c greater than 30-50nm, the Hall-Patch rule applies which supports dislocation nucleation and motion [111].

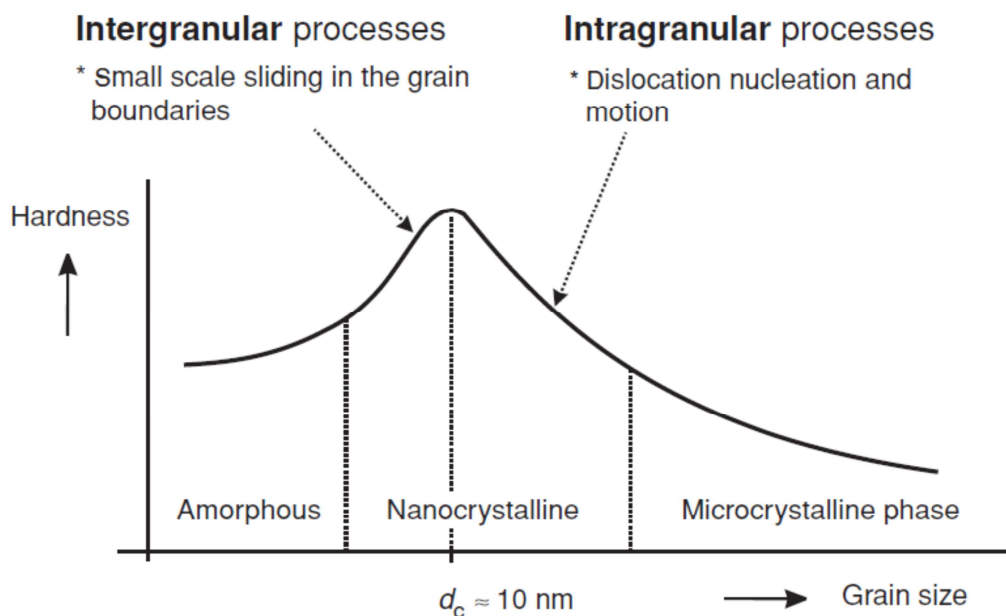


Figure 6.7: Illustration of relationship between grain size and material hardness [112]

In 1918, Scherrer formulated a method to prove that the size of the Bragg peaks is directly proportional to the crystallite size of the powder/coating. Since then line profile analysis gained its popularity for applications in crystallography. During the time period it was found that the width of Bragg reflections does not only reflect the size of the crystal, but is also a result of instrumental, crystallite size and strain broadening which is discussed in detail in the next sections. Therefore, it is important to consider all the above mentioned factors in order to calculate an accurate grain size. Since all these line broadening factors occur together, instrumental broadening as well as line profile (for

size strain and microstrain) have to be analyzed. Since in the present work only crystal size has been discussed the instrumental broadening analysis has been performed (see Section 6.2.1).

6.2.1. Instrumental Broadening Analysis

Diffraction patterns obtained from Bragg reflections are affected by the instrumental settings like width of diverging and receiving slits, emission profile of the tube, filters, monochromators etc. Factors like misalignment of the diffractometer and no perfect absorption of the radiation are some sources of instrumental error. Therefore, instrumental broadening analysis was performed before the determination of the lattice parameter [113].

Instrumental broadening is measured experimentally by measuring peaks of a reference material. A standard specimen for line profile analysis should have a crystal size of about 1 μm , with large number of untextured polycrystalline grains with zero or negligible microstrain [113]. A peak profile of the reference material should be available measured with the same data set as of the specimen to be measured. Background subtraction is performed for both the specimen and their Fourier coefficients are determined [114, 115]. Literature refers the use of BaF_2 , LaB_6 (SRM660), sintered corundum plate (SRM1976) and KCl as some of the reference materials used for the measurement of instrument broadening [116].

$2\theta(\text{radians})$	Θ (radians)	(h k l)	$\beta_{\text{inst}} = \text{FWHM of instrument}$
0.911	0.455	(4 2 0)	0.052

Table 6-1: Estimation of instrumental error through FWHM analysis of Al_2O_3 standard

In order to analyze the XRD peak profiles, Full-Width at Half Maximum (FWHM) is often used as a factor to estimate the lattice parameters of single crystals, texture or stress in a polycrystalline material. A number of researchers have analyzed to the availability of stacking faults and structural disorderness by means of FWHM of the XRD peaks [117]. Measurement of tensile stresses in a material by estimation of FWHM has also been conducted [118]. An estimation of the instrument broadening for the present work has been performed using Al_2O_3 standard (Table 6-1). All the peak broadening obtained during the measurement of the standard are due to the instrumental broadening as 99% of the particles are about 1 μm resulting in less than 0.01° Full Width Half Maximum (FWHM) because of sample influence in the measurement.

6.2.2. Scherrer Method

A conventional method to determine the crystallite size is the Scherrer Method proposed by Paul Scherrer in 1981 [119]. Equation 6.1 show a mathematical formulation of the proposed Scherrer Method.

$$D = \frac{K \cdot \lambda}{\cos \theta \cdot \beta_{hkl}} \quad \text{Equation 6.1}$$

$$\beta_{hkl}^2 = \beta_{instrument}^2 + \beta_{measurement}^2 \quad \text{Equation 6.2}$$

where

β_{hkl} = FWHM peak of the crystal

$\beta_{instrument}$ = FWHM peak of the instrument

$\beta_{measurement}$ = FWHM peak of the crystal with instrumental error

K= shape of crystallite size

λ = X-ray wavelength in nm

Using X-ray diffraction and Braggs Law the mean size of nano-crystallines in nano-crystalline bulk material can be measured. This method does not consider the crystal strain effects present within the material [120]. In the present study K=0.89 which is assumed for crystals of spherical shape. The Scherrer equation is suitable for crystals when the crystal size is less than 100 nm. A big disadvantage of the Scherrer equation is that no particle strain is considered during the calculation of crystal size. Crystal size analysis under consideration of strain can be obtained through modified modified Scherrer or William Hallson method. Literature proposes Transmission Electron Microscopy as an accurate method to estimate crystal size [121].

Coating	Crystallite Size (nm)
Cr1/CrN1	CrN: 41 ± 4, Cr: 65
Cr1/CrN3	CrN: 19, Cr:25
Cr3/CrN1	CrN: 21 ± 4, Cr ₂ N: 27, Cr: 49
Cr0.25/CrN0.25	CrN: 19 ± 4; Cr ₂ N: 19; Cr:30
Cr0.5/CrN0.5	CrN: 26, Cr ₂ N: 26, Cr:23
Cr0.25/CrN3.75	CrN: 16; Cr ₂ N: 20; Cr: 24
TiN	25± 4, 3089
Ti/CrN	Cr ₂ Ti: 74 ± 26; Cr ₂ N: 34; Ti _x N _y :12
TiN/CrN	CrN:6; Cr ₂ Ti: 12; Cr ₂ N: 27

Table 6-2: Average crystal size analysis of multilayer and single layer coatings

In Table 6-2, the crystal size of various multilayers and TiN single layer can be seen. Measurements of 2-4 peaks were performed for each diffractogram and an average crystal size was calculated. Only Cr1/CrN1 and Ti/CrN multilayer coatings show large crystal sizes, 35nm and 49nm respectively. All other coatings show an average crystal size below 30 nm.

The crystal size of the reactive sputtered coatings is dependent on the ion/atom (J_i/J_o) ratio which is influenced by the N_2/Ar ratio during the deposition process. A crystal size of approximately 20-60 nm was reported for a mixture of Cr_2N and CrN phase within a N_2/Ar ratio of 0.2-0.4 [122]. Similar results were found through the measurements (Table 6-2), where the size of CrN/ Cr_2N phases was found to be between 16-41 nm.

6.3. Stress Analysis

6.3.1. $\sin^2 \psi$ - Method for stress analysis

Due to high energies during plasma assisted vapour deposition macrostress (σ) is expected which influences the properties of the coatings. An excessive amount of stress can lead to film and substrate cracking in case of tensile stresses and film cohesion and buckling in case of compressive stresses [123].

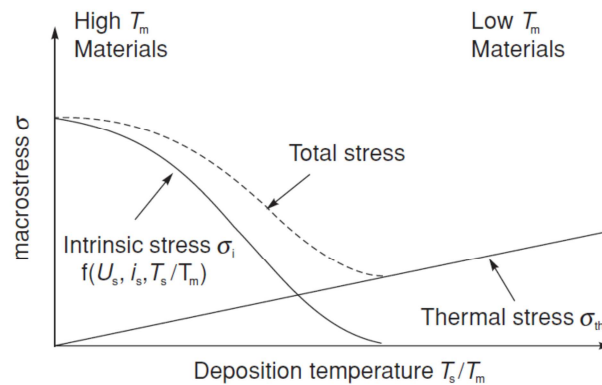


Figure 6.8: Schematic diagram of the macrostress σ versus T_s/T_m

Macrostress within coatings can be further classified into intrinsic (growth) stresses and thermal stresses. Intrinsic stresses take place when an accumulation of crystal defects within the film occurs during deposition. The generation of thermal stresses takes place due to different thermal expansion coefficients of film and substrate [124]. A comprehensive analysis on stress generated during deposition process show that intrinsic stresses within a coating decrease with the increase in T_s/T_m ratio (Fig. 6.8). In contrast, an increase in thermal stresses correlated to an increase in homologous temperature. Hence total stress, which is a sum of intrinsic and thermal stress decrease with increasing homologous temperature and increase with the increase after a critical homologous temperature is approached [124].

In this work a conventional $\sin^2\psi$ method is used to address the macro stresses within the deposited coatings. In conventional $\sin^2\psi$ method, the distance between two atoms (d) is considered as the strain gauge. A $\langle hkl \rangle$ is opted for which all the measurements have to take place. By tilting the table at an angle ψ , from normal to the hkl , strain in various grains of the same hkl values are measured. The stress is then measured through linear elasticity formalism through elastic constant tensor of the material [125]. A schematic of the $\sin^2\psi$ method can be seen in Fig. 6.9.

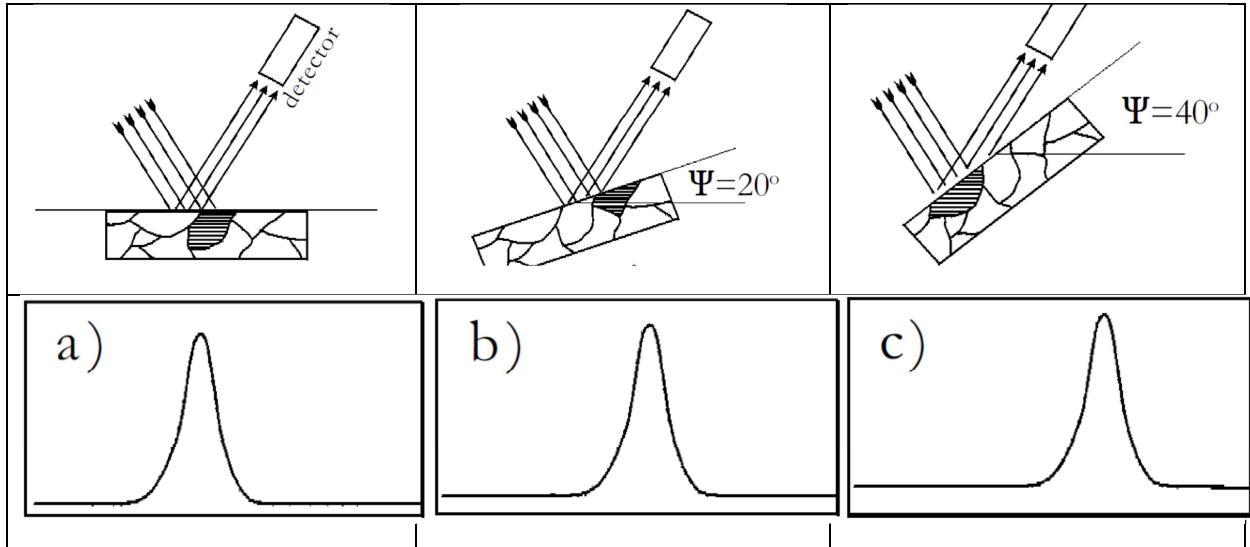


Figure 6.9: Shift of diffraction peak with changing tilt angle

Stress through $\sin^2\psi$ method can be estimated from the following formula:

$$\sigma = 1 + \frac{E}{(1+\nu) \sin^2 \varphi} \frac{(dn-d_0)}{d_0} \quad \text{Equation 6.3}$$

where

σ = residual stress within the coating

E = E-Modulus of coating

Ψ = Tilt angle of the specimen

ν = Poisson ratio

d_0 = d-spacing without stress

dn = d-spacing with stress

By plotting a relationship between ' d ' and ' $\sin^2\psi$ ', macro stress and the stress free lattice parameters can be estimated from slope and ordinate respectively. Deviations of the values from the linearity can be obtained due to the availability of texture and/or stress gradients [125].

6.3.2. Stress Measurements

An analysis of the Cr1/CrN3 coating with analysis of Cr and CrN phases is conducted through XRD analysis (Fig.6.10). The Cr-peak is only identified when the specimen is not tilted ($\psi=0$; shown with light green color). With tilting of table of Cr (1 1 0)-peak disappears with appearance of other peaks at various angles (Fig. 6.10a). This behavior hints to a high texture of the coating. The Cr (1 1 0)-peak is considered for further analysis with a constant E-Modulus of 279 GPa and a Poisson ratio of 0.21. The d-spacing values of the Cr (1 1 0) peak at tilting angles were recorded as a function of angles in a graph (Fig.6.10a) and the observed slope represents the available residual stress within the coating layer. Stress analysis showed that a compressive stress of 1962 ± 1045 MPa for the Cr-layer within the multilayer coatings. The high standard deviation within the measurements indicates a pronounced texture of the Cr-coating or the superimposition of the CrN coating on the Cr-layers.

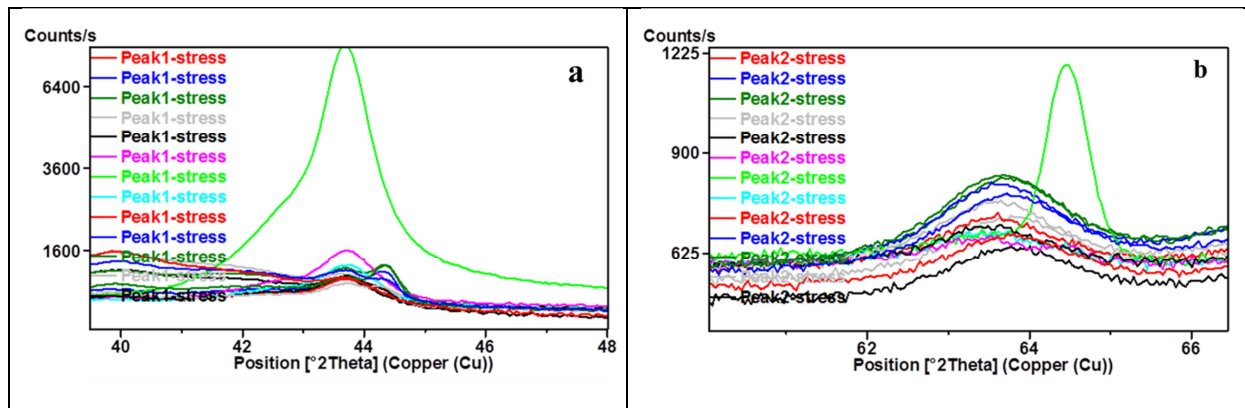


Figure 6.10: Peaks observed at various Chi angles (a) @44.393° for Cr (110) (b) @63.204° for CrN(220) in Cr1/CrN3 multilayer coating

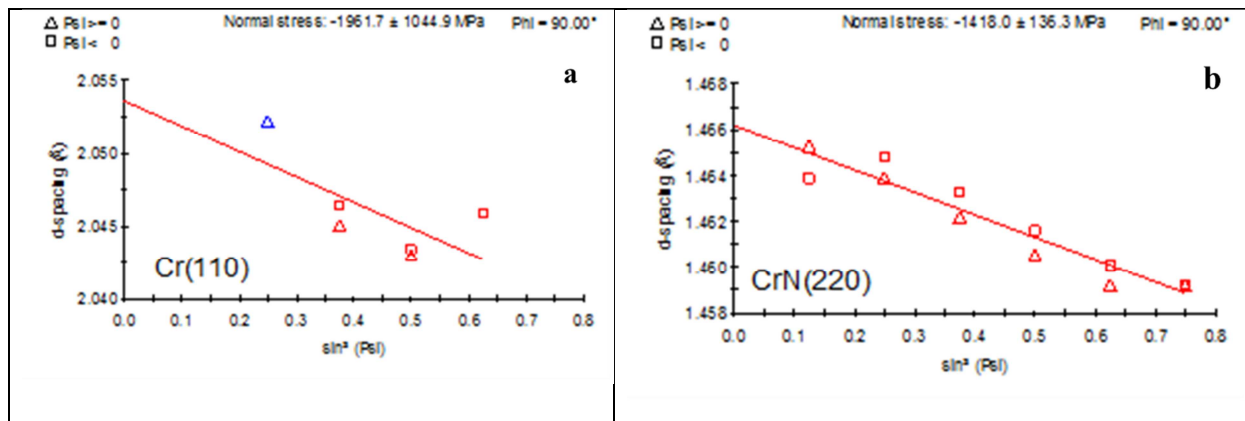


Figure 6.11: $\sin^2\psi$ plots for (a) Cr-layer (b) CrN-layer performed for Cr1/CrN3 multilayer coating

A similar type of analysis has been conducted for a CrN layer for a peak measured at 63.204° with an orientation of (2 2 0). The disappearance of CrN (2 2 0) peak was observed as the specimen was tilted at various angles (Fig. 6.10b) as in the previous practice, the d-spacing was calculated at various tilting

angle and was plotted against the $\sin^2\psi$ values. The stress in the CrN coating was found to be compressive and was in the range of 1418 ± 136.3 GPa.

The effect of the increase in the thickness of ceramic layer (CrN) and decrease of metallic layer (Cr) layer is discussed through a stress measurement performed for the Cr_{0.25}/CrN_{3.75} specimen. It was found that no Cr-reflections for the coating are detected. It is assumed this behavior of Cr layer is due to the high thickness of CrN top coating. An analysis of CrN for a (2 0 0) and (2 2 0) peak are shown in Fig.6.12a, b. In contrast to Cr₁/CrN₃, the CrN-peaks can be observed in all the possible tilt positions which was not the case in Cr₁/CrN₃. Analysis of the d-spacing at various angles with $\sin^2\psi$ for CrN (2 2 0) showed the presence of a compressive stress of 1195.8 ± 176.3 GPa (Fig. 6.13).

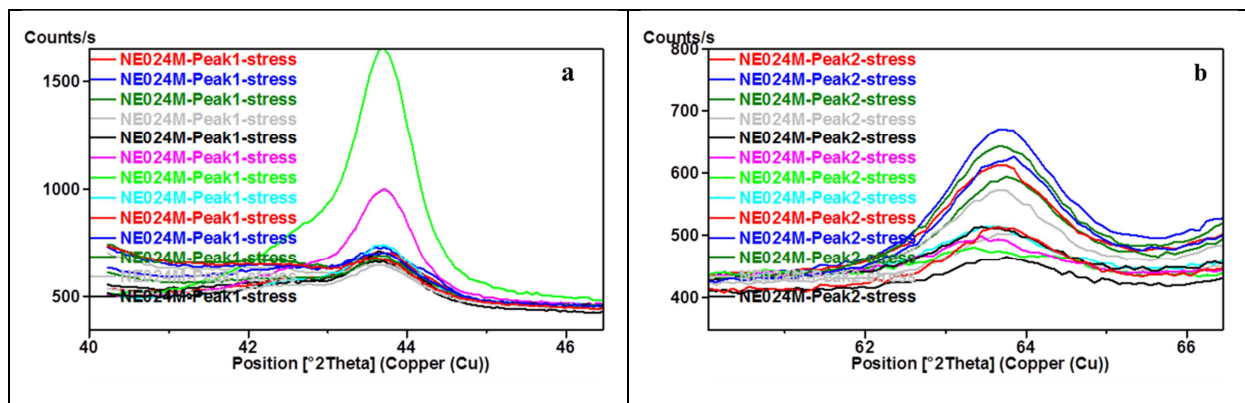


Figure 6.12: Peaks observed at various Chi angles (a) @44.393° for CrN (200) (b) @63.204° for CrN(220) in Cr_{0.25}/CrN_{3.75} multilayer coatings

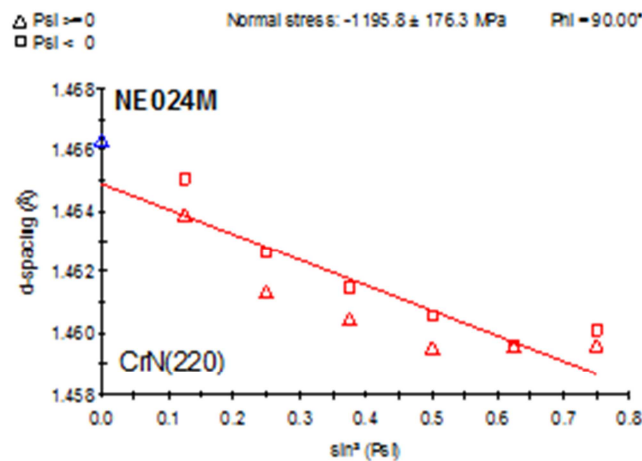


Figure 6.13: $\sin^2\psi$ plots for a CrN-layer in a Cr_{0.25}/CrN_{3.75} multilayer coating

The above discussed analysis shows that similar results were obtained for the top layers for Cr₁/CrN₃ and Cr_{0.25}/CrN_{3.75} coatings. This leads to the interpretation that the thickness of the metallic or the ceramic components in the deposited multilayer does not influence the stress level within the coating significantly.

7. Erosion Behavior

7.1. Cr/CrN Multilayer Coatings

During the last years various ductile and brittle coatings for protection against wear of compressor components in aeroengines. Ductile coatings lead to high plastic deformation at low angles (15-55°) whereas brittle coatings display a high material erosion at high incidence angles (75-90°). Since particle impingement with compressor components experience is possible at 0-90°, it is necessary to design a coating containing ductile and brittle components [5].

A possible method to design such a coating is the deposition of alternating metallic and ceramic layers to form a multilayer coating. The ductile layers in a multilayer system would allow erosion resistance at high angles whereas the brittle layers would resist the particle penetration at low angles. It was postulated by Lawn et. al. [98] that multilayer coatings comprising of brittle coatings with thin soft intermetallic layers provide best energy absorption due to restricting cracks to individual layers and due to the distribution of energy through the whole system. Moreover, the different material parameters of such a system are responsible for the combined behavior of the coatings.

In the present study an approach has been made to understand the erosion mechanism of Cr/CrN multilayer coatings. The reason for the application of Cr/CrN coatings lies in the mechanical and chemical properties achieved from the individual components used in this coating architecture. CrN coating is known as wear resistant and offers high protection against corrosion [126]. Moreover, low intrinsic stresses and low friction coefficients have also been reported for CrN coatings [127]. A combination of Cr and CrN layers would provide a combination of ductile properties of Cr coating leading to low removal during erosion whereas CrN would provide more fracture toughness leading to resistance to crack propagation.

7.1.1. Gravimetric Analysis

Erosion tests were conducted at room temperature at incidence angles of 30° and 90°. Macroscopic images of the exemplary specimens of Cr_{0.25}/CrN_{0.25} and Cr_{0.25}/CrN_{3.75} are depicted in Fig.7.1.

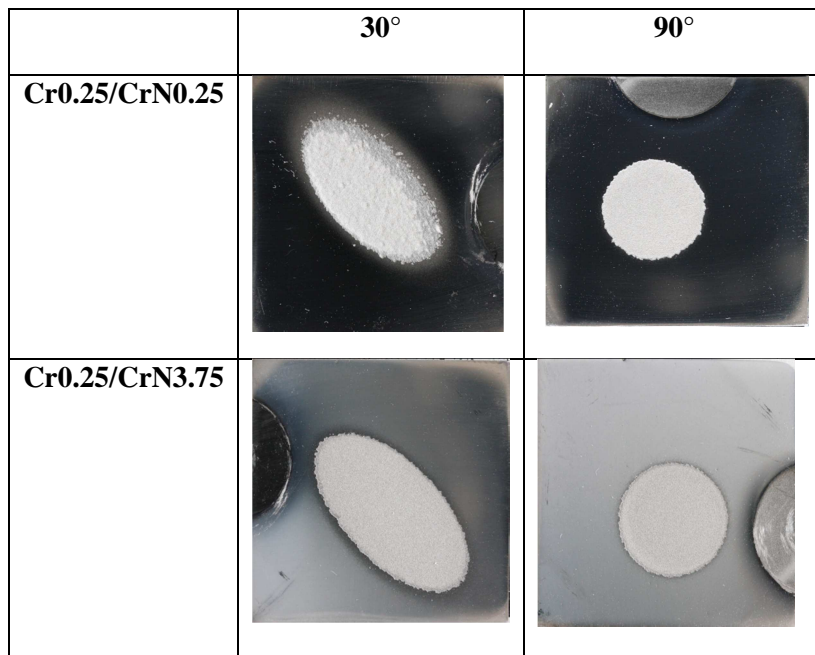


Figure 7.1: Macroscopic images of multilayer Cr/CrN multilayer coatings

It can be seen that the shape of the erosion scar changed from oval/elliptical at 30° to a round shape for 90° incidence angle (Fig. 7.1). This change in shape can be related to the increase in contact area between the particles and the coating surface during the erosion process at various angles. Another interesting finding is the optical difference observed at 30° incidence angle between the two coatings. It can be observed that sharp transfer from substrate to coating can be observed within the eroded area for Cr0.25/CrN3.75 whereas no clear coating edges were observed for Cr0.25/CrN0.25. This indicates that the erosion process for Cr0.25/CrN0.25 does not allow rapid spallation during the erosion process.

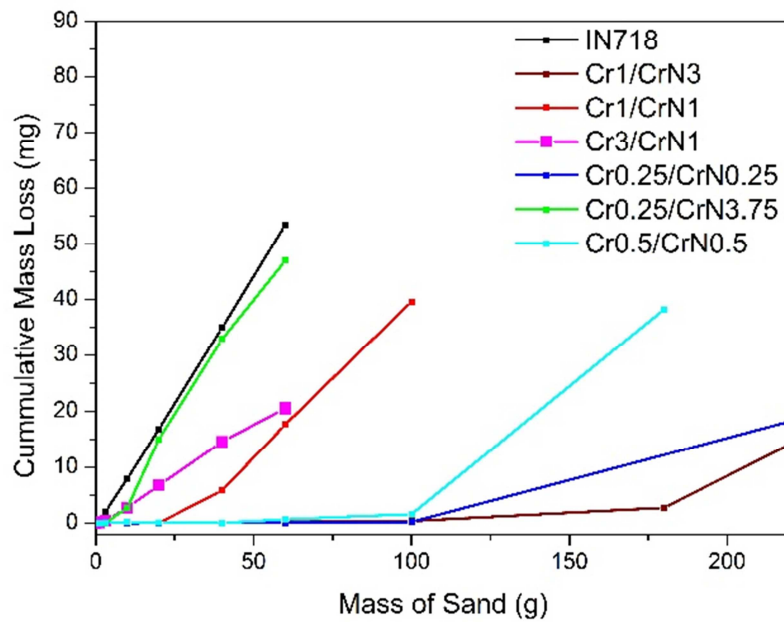


Figure 7.2: Gravimetric measurements for erosion of multilayer Cr/CrN coatings at 30° impact angle

Such type of behavior is generally observed for coatings with a good adhesion to the substrate or which support layer by layer removal of coating segments. Gravimetric analysis of Cr/CrN multilayer coatings at an incidence angle of 30° show that most of the multilayer coatings protect against erosion (Fig.7.2). Cr0.5/CrN0.5, Cr1/CrN3 and Cr0.25/CrN0.25 coatings show relatively longer incubation times compared to IN718 substrate without coating. The erosion curve of Cr0.5/CrN0.5 is found to be nearly parallel to the erosion curve of the uncoated IN718 after the incubation time depicting that coating has been rapidly eroded after the incubation period. In contrary, Cr0.25/CrN0.25 and Cr1/CrN3 showed a non-parallel behavior after the incubation time indicating slow removal of the coatings. This behavior also indicates that even after the first cracks are generated, the coating architecture does not allow the acceleration of the crack propagation process. High energetic particles are required to completely erode the coating for the substrate. Since metal phases show critical behavior during erosion at an incidence angle of 30°, further improvement of the system with a coating with higher hardness and higher fracture toughness is intended.

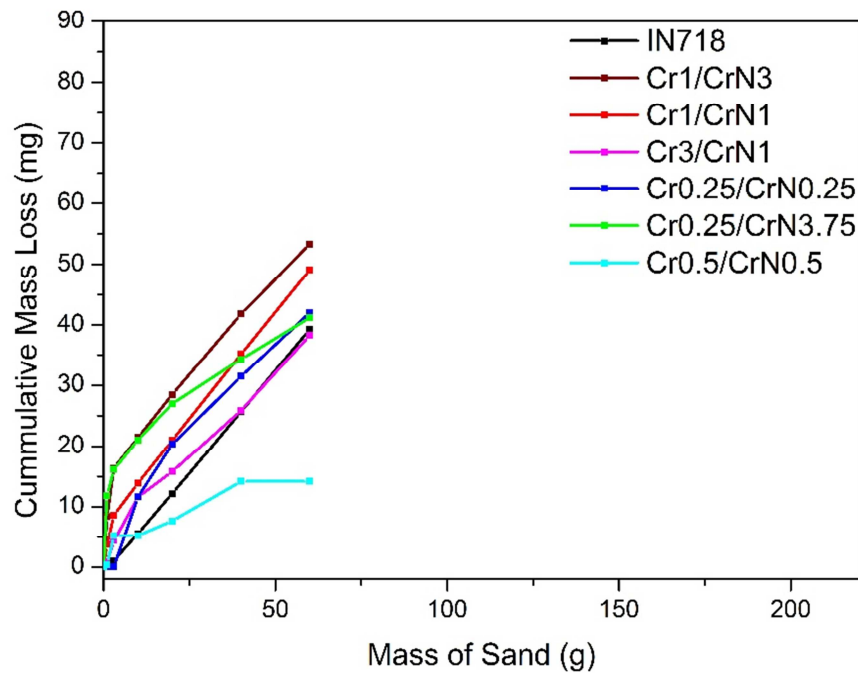


Figure 7.3: Gravimetric measurements observed during erosion of multilayer Cr/CrN coatings at an incidence angle of 90°

Erosion analyses of the coatings at normal angles are depicted in Fig. 7.3. No coating showed an incubation time in this case. Hence, the performance of this coating deteriorated during the erosion process at oblique angles. Multilayer coatings with high CrN volume i.e. Cr1/CrN3 and Cr0.25/CrN3.75 seem to be showing the worse erosion behavior in this case. Since ceramic phases are critical at oblique incidence angles, hence it can be interpreted that high volumes of ceramic phases within a coating would always be critical during erosion at 90°. A thickness of 0.25 μm of CrN seems to be a better option but still not the best one. Another possibility to improve the coating behavior at oblique angles can be used as a ceramic coating of relatively higher fracture toughness.

7.1.2. Erosion Mechanism

The erosion mechanisms in single or multilayer coatings differ in accordance to the various testing conditions. In the present investigation a variation in the bilayer period of the Cr/CrN multilayer coating is used to study the erosion mechanisms. This variation would lead to different mechanical and structural properties affecting the crack propagation within the coating. Moreover, a variation in the particle incidence angle of the erosion particle has also been discussed here to understand the more ductile or brittle behavior of the coating due to changes in the bilayer period.

A SEM image of a Cr1/CrN1 coating shows the removal of the coating in large pieces from the coating surface (Fig. 7.4a). A high density of lateral cracks mostly on the metallic-ceramic interface can also be detected. Hence, formations of such cracks at the interface of the coating are caused due to low mechanical bonding between the two layers. Moreover, intercolumnar shearing of the coating also took place at some locations within the cross-section.

PVD coatings grow in form of columnar structures and are prone to failure when these columns are subjected to external loading. Due to impingement of particles with high velocities, bending of these columns take place leading to vertical cracking and shearing of columns [64]. A similar effect can be seen for the Cr1/CrN1 coating eroded at 90° (Figure. 7.4b). Once a crack is initiated in the top layer, instead of crack deflection in the second layer, continuous crack propagation between the grown columns takes place until the crack reaches the substrate. Initiation of lateral cracking is expected in the further stages of the erosion process leading to removal of the coating in form of pieces between two vertical cracks. Failure of coatings due to compressive stresses can be related to the continuous particle impact on the coating surface leading to surface fatigue [128].

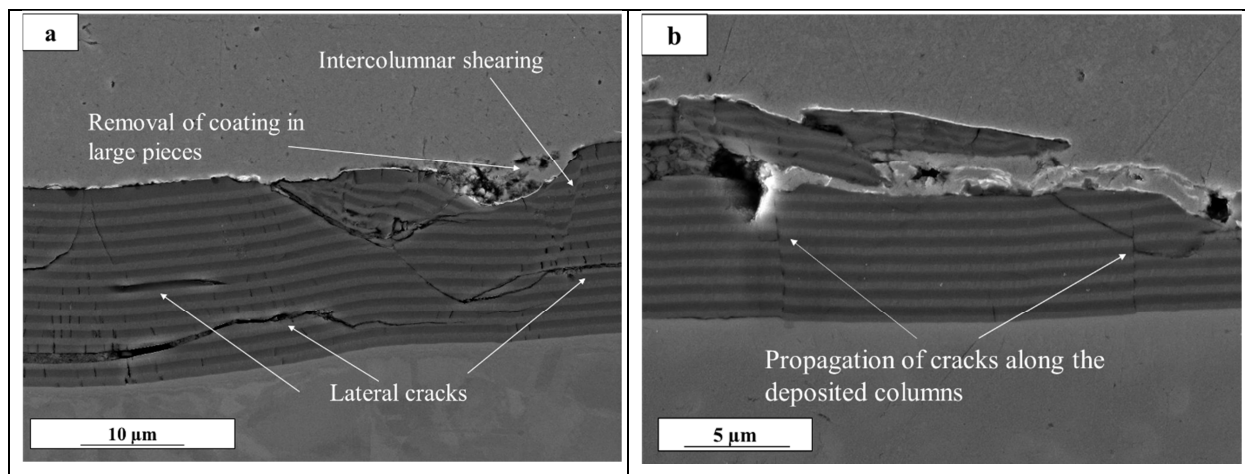


Figure 7.4: Cr1/CrN1 coating at (a-b) 90 °incidence angle

Due to high cyclic loading during the solid particle erosion, the coating applies a compressive stress on the substrate. When these compressive stresses exceed the plastic limit of the substrate, a shear failure of the coating occurs leading to embedding of the coating into the substrate accompanied with substrate deformation. This is also referred as shear step in literature [129]. A similar effect can be seen in Fig. 7.5a. where a number of coating columns are displaced (δ) due to the incidence of sharp edged erodent. According to Bhomwick et. al. [129] when an indenter penetrates a coating surface, and a displacement δ is induced by the indenter, the columns at the edge of the indenter displace vertically with a distance δ as shown in Fig. 7.5b. This leads to push the coating within the

substrate resulting in expansion of plastic cavity within the coating. Therefore, the indenter has to overcome the resistance due to intercolumnar shear and the elasto-plastic resistance of the bulk substrate. A possibility to reduce this shear failure is to increase the thickness of the coating in order to decrease the intensity of the internal stresses between the two consecutive layers or between coating and substrate [23].

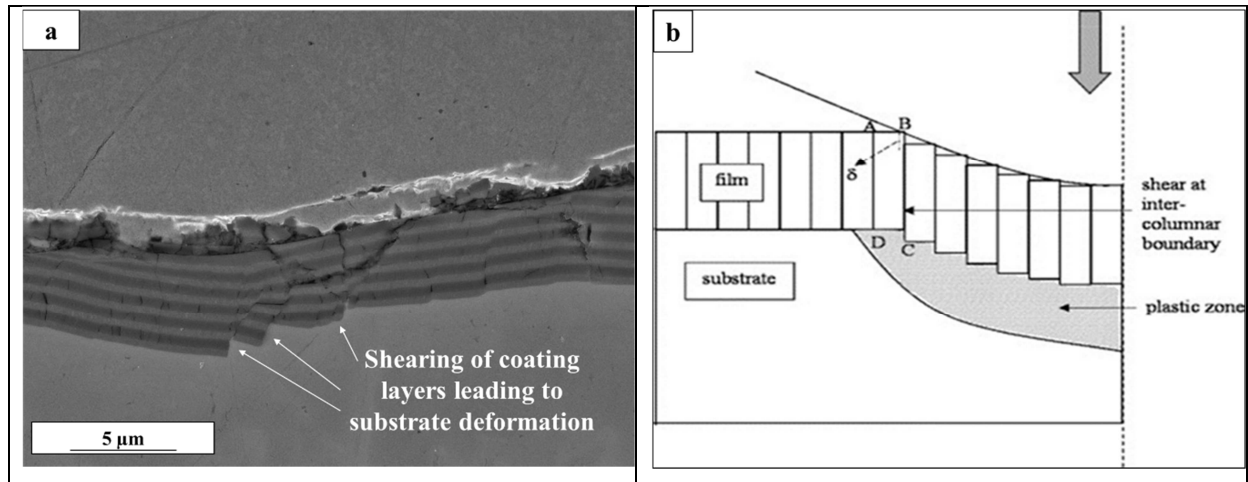


Figure 7.5: Intercolumnar shear sliding of (a) Cr1/CrN1 coating (b) Schematic

Fig. 7.6a shows the erosion of surfaces at oblique angles for a Cr1/CrN3 coating with an appearance of consecutive semicircular cracks (cone cracks) on the coating surface. Cone crack generation is caused due to residual stresses on the surface and the failure of surface due to contact. This type of cracking has been defined as the Mode I type failure and a specific stress intensity factor is required to induce such type of cracks [130]. The generation of conical cracks is a consequence of radial cracks (Fig. 7.6b). Radial cracks generated at the coating substrate interface which propagate during the erosion process finally leading to distortion of the coating into pieces. Multiple radial cracks generate during the erosion and finally tend to form a network due to the cohesive property of the cracks.

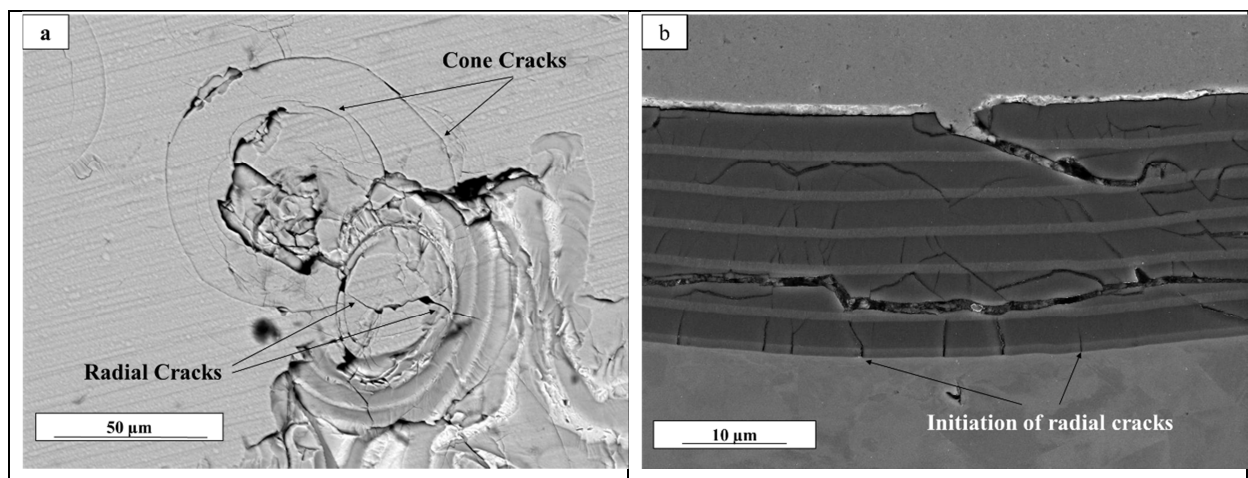


Figure 7.6: (a) SEM image of Cr1/CrN3 at 90° impact angle (a) surface (b) cross-section

Formation of cone and radial cracks during the impact is a characteristic of ceramic layer. An interesting development of cone or radial cracks during the abrasion process has been studied by Qasim et. al [131]. According to them, the individual coating thickness in a bilayer coating and the size of the indenter (incoming particle) is responsible to decide if the failure would lead to cone or radial cracking. Critical load has been identified as one of the important factors which lead to surface yielding in form of cone cracks or to interface /substrate yielding leading to radial cracks. Another theory of the material removal process in form of cone cracks or radial cracks have been provided by Lee et. al. [132]. They found that the elastic mismatch between coating and substrate is one of the key factor in ruling the formation of radial or cone cracks. For $E_c/E_s < 5$ (hard substrates) a formation of radial cracks would initiate first whereas $E_c/E_s > 5$ (soft substrates) would favor the formation of cone cracks. Radial cracks pop at the coating-substrate interface and propagate radially into the coating over lateral distances. They propagate in the subsurface and find their way to the surface when the external loading exceeds the critical load values of the coatings. Formation of such cracks is a function of material properties and the external loading [133, 134]. Cone cracking is referred as a secondary abrasion process in literature as it is observed after the formation of radial cracks [135]. Cone cracking needs generally needs higher impact energies than radial cracking [133].

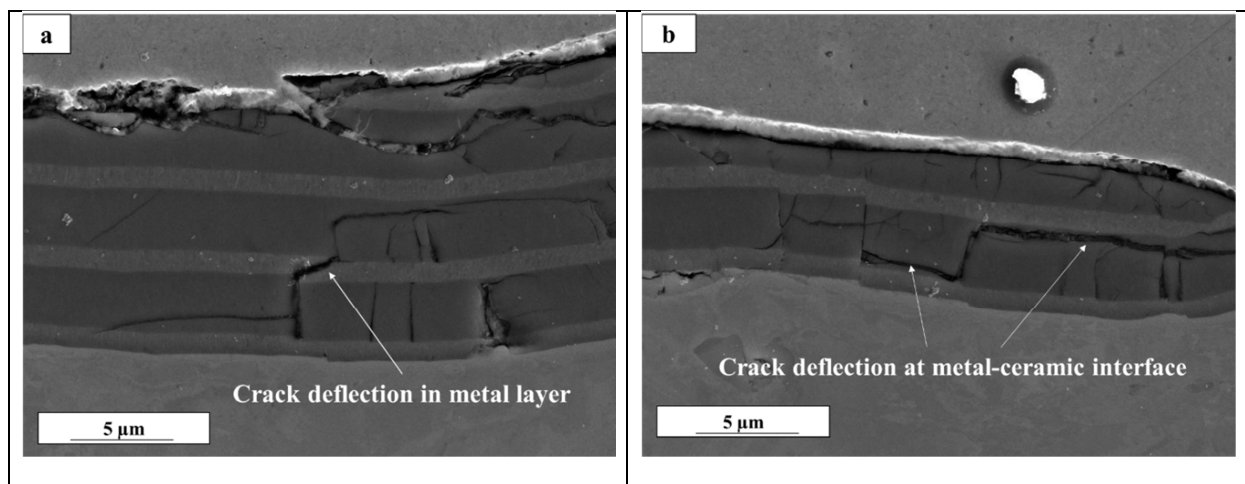


Figure 7.7: Erosion mechanism observed for Cr1/CrN3 multilayer coatings (a) incidence angle 30° (b) incidence angle 90°

A layer by layer material removal is depicted for an incidence angle of 30° (Fig. 7.7a) for Cr1/CrN3 coating. A crack is originated during the erosion process in the CrN layer which deflected with a slope within a metal layer. The crack propagation from metal Cr to CrN layer further deflected at an angle of 135 ° and propagated in further stages normal to the interface. The sloped propagation of the cracks in a metal layer clearly addresses to the advantage of using materials of various mechanical properties. It can also be observed that many of the cracks generated at the metal-ceramic interface and stopped at the next metal-ceramic interface. Hence, it can be interpreted that the toughness of the metal Cr layer was high enough for such loading conditions which resisted the further propagation of the crack. This layer by layer removal process would prolong the material removal process which is essential for the

long incubation times. Most of the specimen tested in this work at shallow angles show a similar behavior.

A comprehensive explanation of tribological behavior of multilayer coatings with thin metal layers has been defined by Chen et. al. [136]. According to them, metal and ceramic layers having different crystalline structures lead to crystal mismatch at grain boundaries. This led to a stress generation at the interfaces and hinders the movement of dislocation in the metallic layer. Coatings with thin metallic layer generally lead to high stresses at the boundaries and hence more amount of ceramic layer is to be removed before a crack can be initiated in the metallic layer. As the thickness of the metallic layer is increase low stresses are needed to initiate plasticity in the metallic coatings. A similar effect can be observed for Cr1/CrN3 eroded at oblique angles in Fig. 7.7b. It can be observed that the crack generated in CrN layer stop or deflect at the interface of the Cr and CrN coating interface. Hence the energy of the particles were enough to generate the cracks but not to allow the movement of this crack into Cr thin layer.

A single particle impact is depicted for Cr3/CrN1 coating (Fig. 7.8a). Plastic deformation of the first layers took place which can be seen in form of a dent. The compressive stresses observed at the edges of the impact seem to exceed the plastic yield of the coating leading to damage (spalling) in that area.

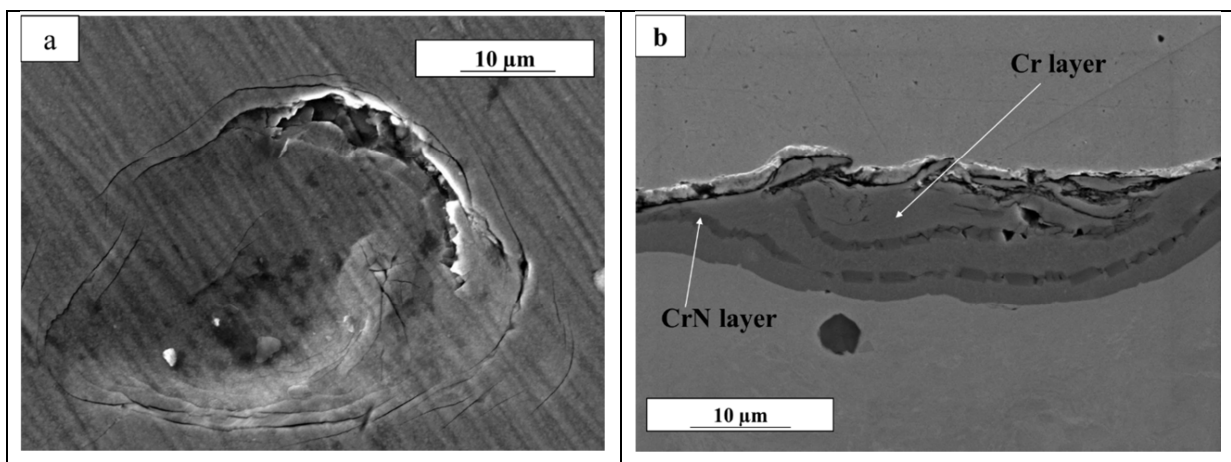


Figure 7.8: (a) Single particle impact Cr3/CrN1 (b) Cross-sectional image of Cr3/CrN1 at normal incidence angle

The theory of plastic deformation of the coating due to single particle impact observed in Fig. 7.8a which can be supported with the cross-section observed in Fig. 7.8b. It can be observed that squeezing of ceramic CrN thin layers took place between the metallic Cr layers during the erosion process. Such a type of behavior can be related to the critical thickness of the layers and the fracture toughness of the coatings. CrN with low thickness and inadequate fracture toughness does not seem to withstand the external loading due to the particles. In contrast, Cr-metallic layers seem to be tough enough to bear the external loading, because no squeezing of metallic layers is reported in previous discussed cases. Therefore, while designing a multilayer system, it is importance to understand the concept of critical

thickness of single layers, so that a combination of mechanical properties can be obtained for the desired applications. SEM and gravimetric analyses of Cr₃/CrN₁ coating lead to the conclusion that such a system did not provide the advantages of a multilayer coating system where no load bearing capacity of CrN layers were observed in a Cr matrix. Wiecinski [84] too reported on the critical thickness of layers where he found an increase in erosion rate with the increasing ductile phase in Cr/CrN multilayer coating. Maurer and Schulze [64] too discussed the importance of critical thickness of films and postulated a variation in the erosion phenomenon when the coating thickness is sufficiently high or low.

An interesting finding on the availability of ductile phase within a ceramic matrix has been reported by Ramanujam and Nakamura [137]. They investigated the erosion behavior of multiple particle erosion of ceramic coatings using FEM analysis. They modelled a NiCrAlY coating with no metal phase, with an addition of 11% CoNiCrAlY and 29% CoNiCrAlY metal phase. A schematic of the eroded behavior during erosion can be observed in Fig. 7.9. The simulated results were categorized into kinetic energy (T), elastic strain energy (We), plastic strain energy (Wp) and total fracture/separation energy (τ). In case of pure ceramic coating, high values of imparted kinetic energies were observed with low values of elastic strain energy and separation energy. With the addition of 11% metal phase, a reduction in the imparted kinetic energy into the substrate is observed as compared to pure ceramic coating. Moreover, plastic strain energy was observed for this specimen along with elastic strain energy. With the increase of metal content, high plastic strain energy values were observed with the decrease in the kinetic energy values imparted by the particles.

Ramanujam and Nakamura [137] also postulated that erosion of a coating is sensitive to the coating structure just below the impacts. A higher material removal in coating with high metallic content was found as compared to pure ceramic coatings and coating with less metallic content. The material removal was found to be in form of large chunks and the large material removal was addressed to high inhomogeneity of coating material and microstructural deficiencies next to the impact locations. The simulation results correspond to the two main fracture mechanisms in metallic/ceramic coatings. The first factor is the fracture toughness at the metal-ceramic boundaries and the second mechanism was the plastic absorption capacity of the coatings. Discussing the combination effect of the two factors, the fracture toughness of the ductile phase plays the more important role. Higher fracture toughness of the ductile phase is responsible for the energy absorption and would lead to high plastic deformation resistance of the coating.

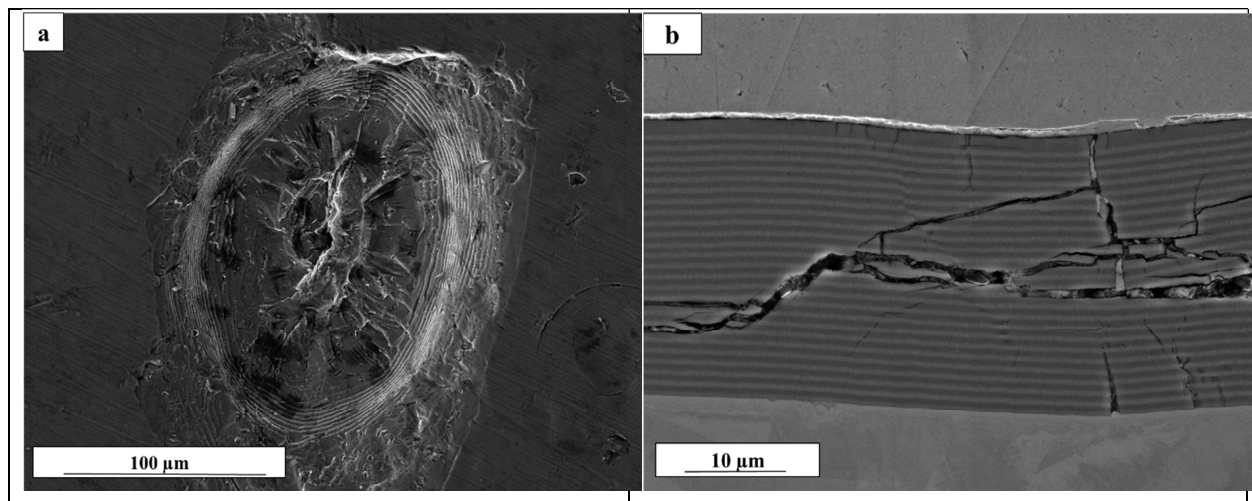


Figure 7.9: SEM image of Cr0.5/CrN0.5 at 90° impact angle (a) single particle impact (b) cross-section image

A single particle impact for Cr0.5/CrN0.5 multilayer coating after erosion at oblique angle is shown in Fig. 7.9a. The size of the crater was found to be approximately 150 μm which can be related to the size of a single erodent particle. The first few coating layers (from the top) revealed a layer by layer erosion which is desired for the deceleration of the erosion process. Detailed analysis of the cross-section of the same specimen shows that an internal distortion of the coating took place leading to the detachment of the coating into pieces (Fig. 7.10b). Multiple impact of the particles lead to crack propagation from the coating surface to the coating-substrate interface but the crack propagation does not lead to a delamination of the coating from the substrate. No clear crack deflection can be seen during the crack propagation and the cross-section is densely occupied by lateral cracks which is typical for ceramic coatings.

7.2. CrN/X (X=Ti,TiN) Multilayers, TiN single layer

In order to study on the erosion behavior due to variation in material properties, the Cr (metallic layer) was replaced with another metallic layer (Ti-coating). A combination of ceramic-ceramic layer was studied by introducing a TiN (ceramic coating) with CrN (ceramic coating). A TiN single layer was deposited in order to compare the multilayer coatings with a conventional single layer erosion resistant coating.

7.2.1. Gravimetric analysis

A gravimetric analysis of the erosion behavior of the different coatings at an incidence angle of 30° can be observed in Fig.7.10. It can be observed that no protection against erosion was obtained for TiN1/CrN3 coating. Hence a total failure can be observed for a ceramic-ceramic combination in this case. An incubation period of 5 minutes was observed in case of Ti1/CrN3 coating. In contrast,

Cr1/CrN3 coating was observed to be best among the multilayer system. In case of single layer TiN coating, no erosion was observed after an erosion period of 8 hours.

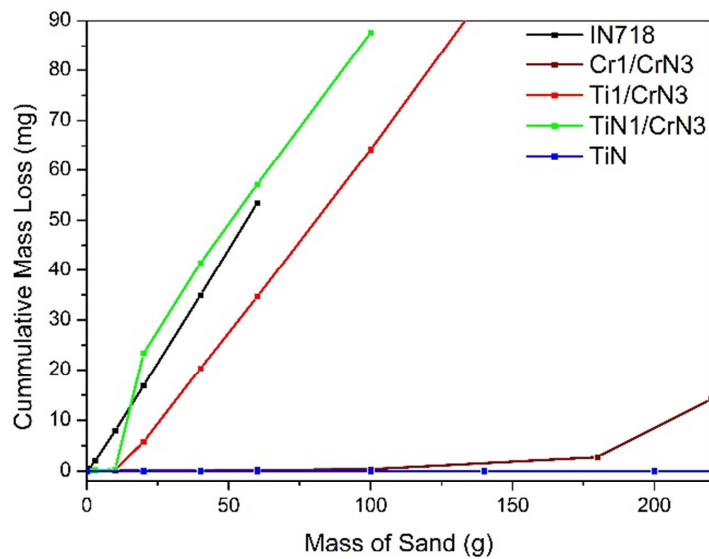


Figure 7.10: Gravimetric analysis of Multilayer and Single layer coatings at 30°

Between all the four tested multilayer coatings in this case, Cr1/CrN3 coating in this case showed the best erosion resistance. Therefore it can be assumed in this case, that the 1:3 ratio observed for Cr/CrN combination cannot be applied for Ti/CrN and TiN/CrN combinations. Gravimetric analysis of the four tested coatings at oblique angles can be observed in Fig. 7.11. It can be seen that TiN single layer coating proved to be the best among all the tested coatings. At normal incidence angles, Cr/CrN multilayer coatings did not show better performance than Ti/CrN and TiN/CrN coating. Hence it can be here directly interpreted that coatings did not show a similar performance during tests at oblique angles as in case of 30°.

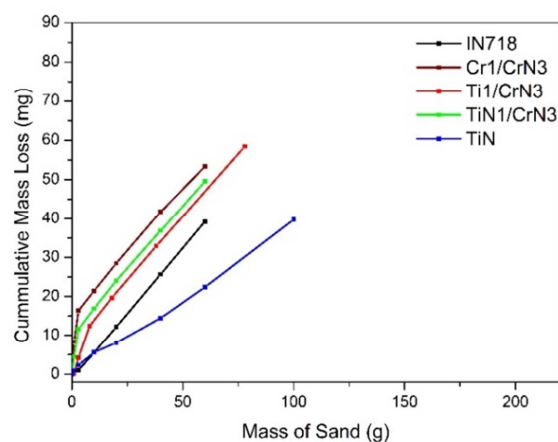


Figure 7.11: Mass Loss graphs of various multilayer and monolayer coatings eroded at 90° impact angle

A comparison between Cr/CrN and TiN/CrN coatings was made by Major et.al. [138] with a thickness of 1 μm of each layer. Moreover, they also proved that the wear performance of a bilayer period of 2 μm of TiN/CrN multilayer was better than Cr/CrN coating. Improved performance of TiN/CrN multilayer was related to the presence of small crystals of TiN (25nm) in the CrN (40nm) coating whereas high lattice distortion of was observed in the Cr/CrN multilayer during deposition process. The findings observed in Fig.7.11 clearly show that Cr/CrN multilayer was a better option for erosion applications at low angle. Moreover, the numbers of bilayers also play a vital role for a particular coating system used for a particular application.

7.2.2. Erosion Mechanism

The erosion behavior of Ti1/CrN3 coatings at various erosion behavior can be observed from Fig.7.12. After first 10 minutes no removal of material can be observed from the optical micrographs. At the end of 20 min, appearance of substrate can be observed which became more evident after erosion at 40g.

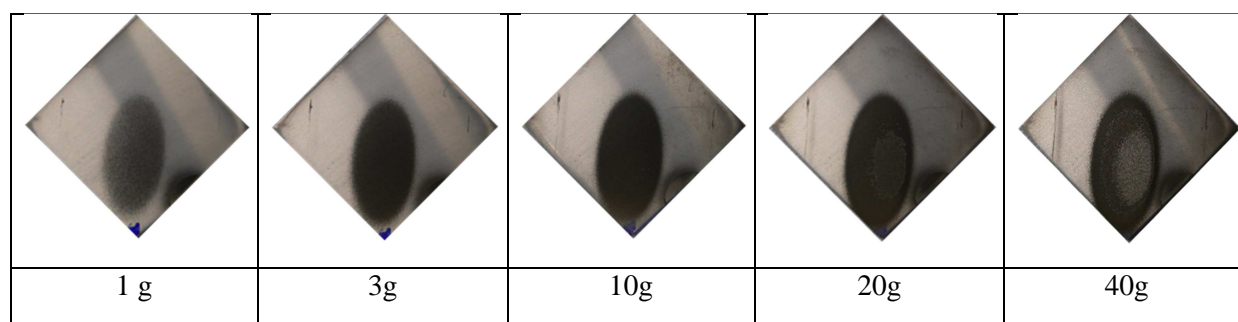


Figure 7.12: Optical images observed for Ti1/CrN3 after various intervals during erosion tests at 30° impact angle

Fig.7.13a shows an SEM image of the Ti/CrN coatings in a low eroded area. It can be seen that the crack initiation took place at the CrN-Ti interface. Therefore, it can be assumed that a weak interfacial energy exists at the CrN-Ti interface which can be either be a result of the difference in lattice structure or in deposition energy of the ions between CrN and Ti layers. Moreover, the crack propagation did always take place in the CrN layer instead of the Ti layer. This can be related to the E-Modulus of the used materials in the coating system. The low E-Modulus of the Titanium (183.42 ± 51.52 GPa) in comparison to CrN (195.76 ± 25.17 GPa) seems to be one of the parameters affecting the behavior of crack propagation.

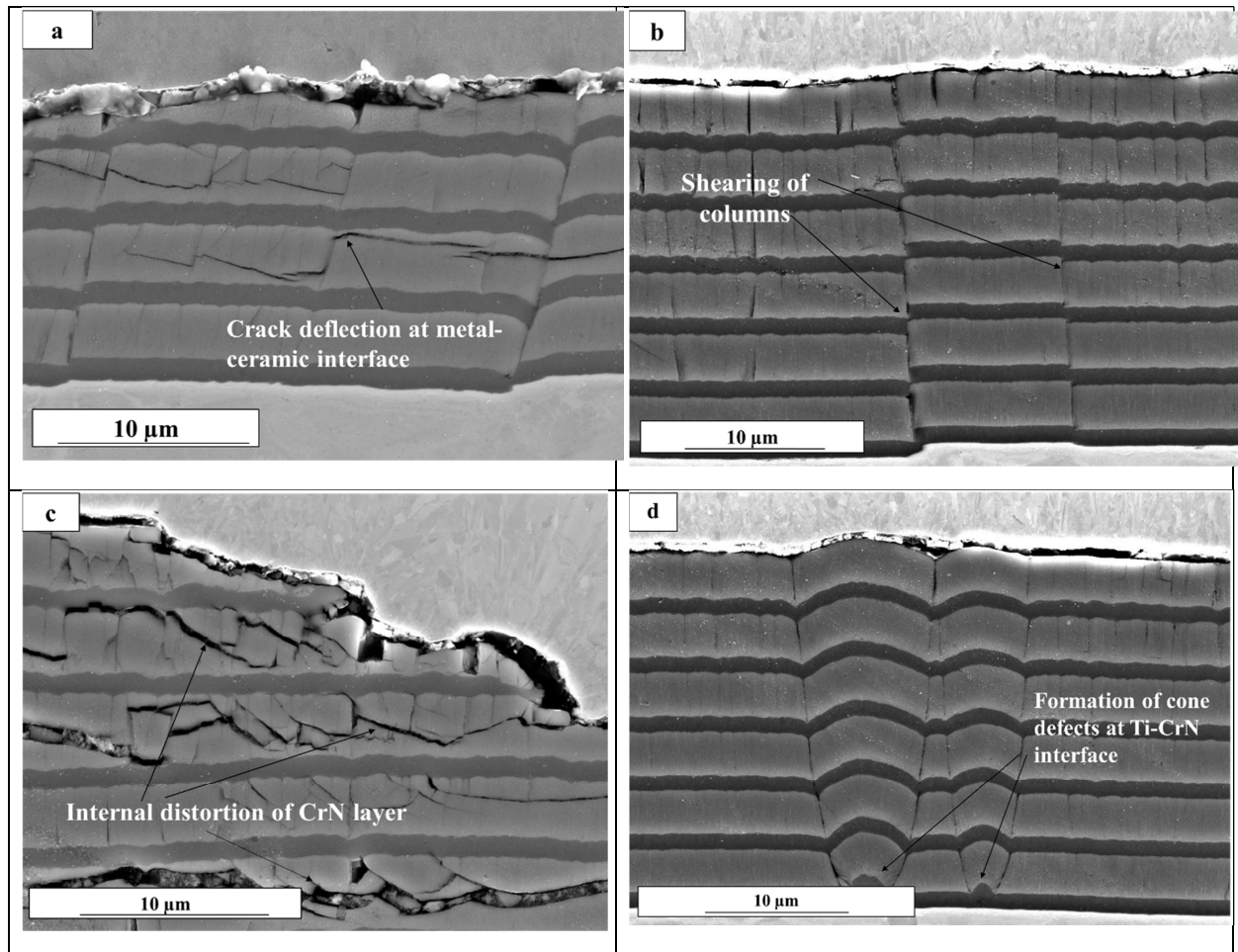


Figure 7.13: SEM images of Ti/CrN coatings at (a) 30° impact angle (b-d) 90° impact angle

An interesting study on the density of the cracks generated during a wear process is discussed by L. Leterrier [139]. According to him, the fragmentation process of a coating system can be classified into 3 stage mechanism. During the first stage, cracks initiate at the defect sites and the propagation of the cracks takes place perpendicular to the loading direction. In order to generate the onset of cracking, the applied load should exceed the critical strain values (also known as crack onset strain, COS). The density of the cracks generated during phase is governed by the statistical number of coating defects available in the coating system. During the second stage, the size of the coating fragments reach a maximum size and no generation of new cracks are observed. Further strain in this stage leads to transverse buckling of the coatings. As observed in Fig. 7.13c, a high density of cracks can be seen for 90° as compared to 30° and can be interpreted that high strain was observed during impact angles. Moreover, presence of lateral cracks at 30° and availability of lateral and transverse cracks at 90° is also a clue that high strain was observed at 90° then at 30°. During stage 3, the crack generation reaches a saturation value and delamination of the coating was addressed as one of the main wear process.

Detailed SEM investigation on the growth of Ti1/CrN3 coatings shows a high density of coating defects (Fig. 7.13d). Defects at coating-substrate interface affect the growth of the multilayer coatings which can be referred as a discontinuation in coating growth. Such type of contamination takes place due to presence of foreign particles before or during the coating process [140]. Literature indicates that growth of such cones at the coating-substrate interface lead to poor adhesion of the coating eventually leading to decohesion and delamination. In case of high residual stresses within the coatings, such defects can lead to spalling of the coating from the surface [141]. In erosion applications, penetration of particles at the opening between defect and coating can lead to rapid crack propagation till the coating-substrate interface. Scratch test results of the Ti1/CrN coating (Section 5.3.2) also support the above mentioned theory as low adhesion and large area spallation were observed for these coatings. A series of optical images during erosion testing of TiN1/CrN3 can be observed in Fig. 7.14. With reference to the gravimetric analysis (Fig. 7.11), mass removal of the coating starts from the very first minutes but no clear damage can be observed from the optical image. With increasing erosion time, the size of erosion scar seem to increase leading to almost complete material removal after 20 min.

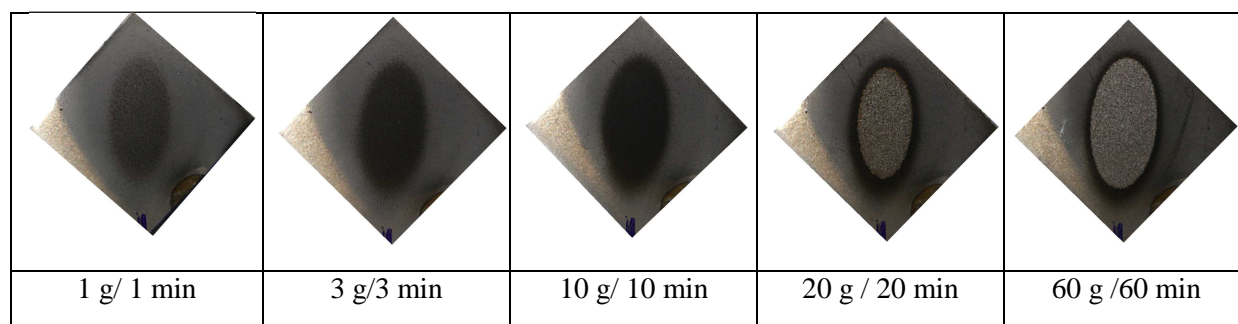


Figure 7.14: Optical images observed for TiN1/CrN3 after various intervals during erosion tests at 30° impact angle

Another important coating growth characteristic of TiN/CrN is the abnormal growth of CrN coating on TiN layer. It was observed that coating growth of CrN layer is form of V-Column structure on TiN coating with nucleation of new columns during the coating process (Section 5.1.2). It can be assumed that an incoming incident particle has a high probability to detach CrN columns because the adhesion between the two consecutive layers is low due to the low contact area. This can be also observed from Fig.7.15a shows a CrN layer is completely removed from the TiN layer. Moreover, crack propagation between the columns which further propagated towards the coating-substrate interface. Hence, better adhesion between two consecutive layers can be a solution to improve the erosion of these coatings. The erosion of a TiN/CrN coating at oblique angles can be observed in Fig. 7.15b. The load bearing capacity of the coating is very low leading to structural disintegration of the coating columns. The crack generation seems to start from the coating substrate interface moving rapidly towards the coating surface. Hence TiN as the bonding layer between coating and substrate may be responsible for the poor adhesion between coating and substrate.

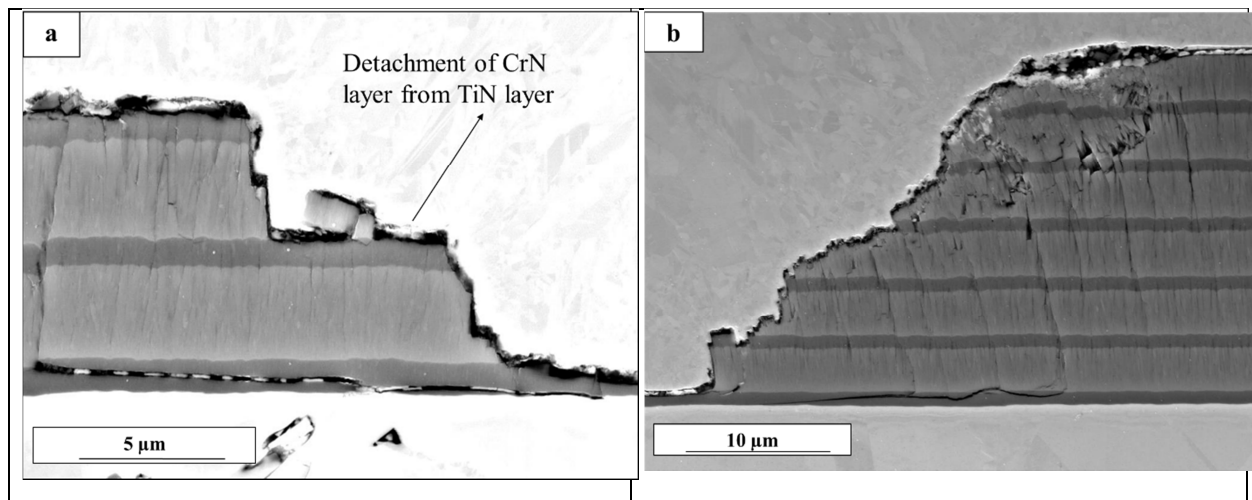


Figure 7.15: SEM images of TiN/CrN coatings a) 30° impact angle b) 90° impact angle

Erosion of a TiN coating at 30° impact angle can be observed in Fig.7.16. The kinetic energy of the incoming particles seems to be low to initiate a crack propagation mechanism in the coating. Removal of the coating surface due to a coating defect can be observed in Fig. 7.16a. It can be observed here that the incident particle was able to remove a part of a column leaving behind an opening on the coating surface. An effect of a single particle impact is seen in Fig.17.6b. As available from the edges the fine columns the TiN coating resist the bending of the columns. Low plastic deformation is determined in this case with no removal of coating (Fig. 7.10).

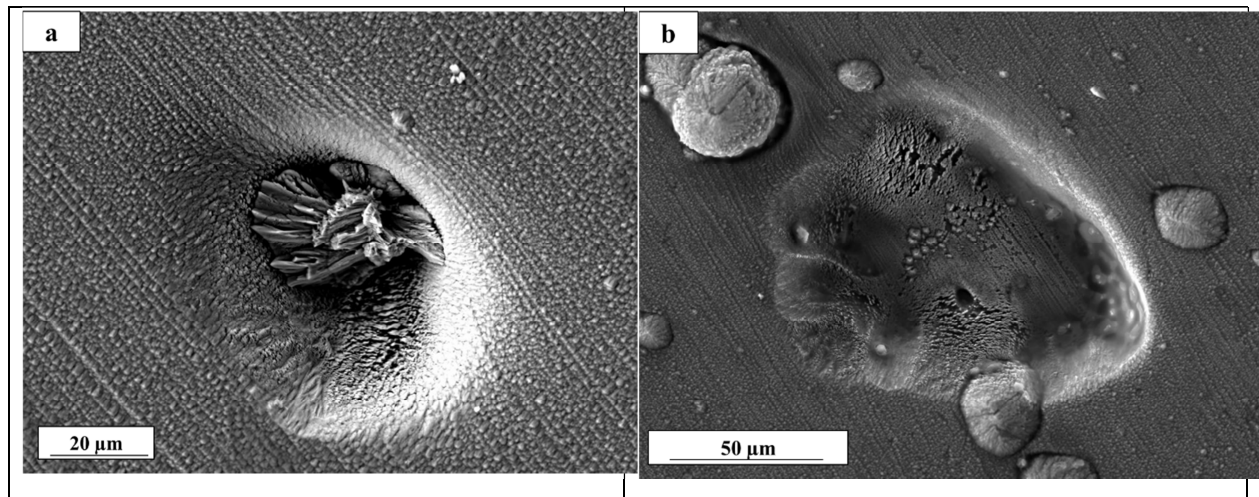


Figure 7.16: SEM images of TiN coatings at a-b) 30° impact angle

An optical analysis of a TiN coating at 90° incidence angle at various instances during the erosion can be observed in Fig. 7.17. at various instants during the erosion process. During the first minutes, nucleation of discontinuities leading to small holes can be seen on the coating surface due to the particle erosion. With further erosion, these holes grow in size making their way to the substrate. A coalescence of these holes in the later stages of the erosion process can lead to removal of coating in large pieces.

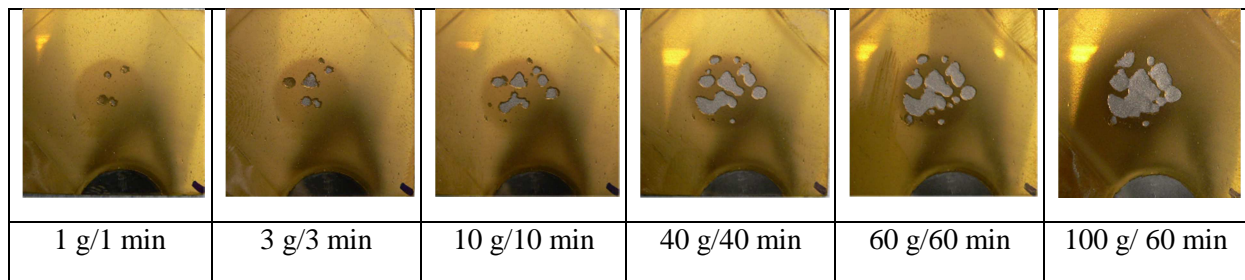


Figure 7.17: Optical images observed for TiN1/CrN3 after various intervals during erosion tests

Fig.7.18 shows SEM images of TiN after erosion at an oblique angle. The presence of carrot-effects (7.18 a) due to availability of contaminants or inadequate arc management process can lead to deterioration in coating structural integrity. A crack propagation between the columns has been preferred at these erosion conditions (7.18-b,c). Moreover, distortion of the coating in form of intercolumnar crack propagation took place. The adhesion of the coating with the substrate sufficient as no crack propagation arises from the coating substrate interface.

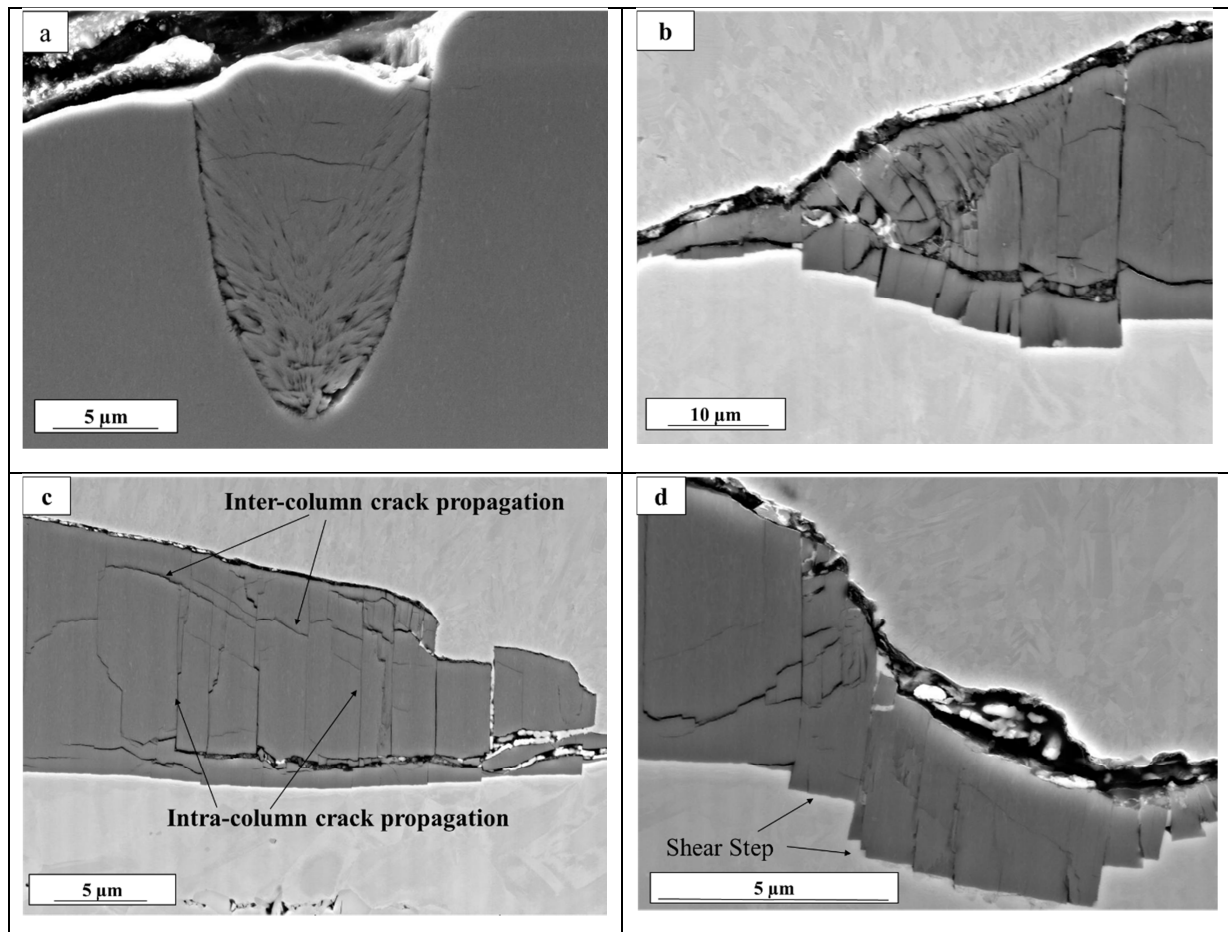


Figure 7.18: Erosion behavior of TiN coating a-d) 90° impact angle

A shear step mechanism can be identified in Fig.7.18d. This mechanism takes place when the compressive stresses in the coating exceed the plastic limits of the substrate leading to embedding of coating in the substrate. This behavior was also seen for Cr/CrN coatings (Fig. 7.5a). The erosion

behavior of TiN coating was studied by Yang et. al. [142]. According to them lower erosion rates were observed at 30° than at 90°. They proposed that transition metal nitrides belong to a group of semi-brittle material. Cutting was identified as the main material removal process at shallow angles and cracking at oblique angles. They also formulated that a moderate cutting and cracking should be offered by a coating for erosion applications. This can be achieved by a combination of optimum hardness and toughness of a coating. In contrast, Languna et.al. reported a ductile erosion of TiN coatings on AISI 4140 Steel [143]. They found cutting effects with the formation of radial cracks at shallow incidence angles in comparison to crater formation at oblique angles. Hence, a higher erosion rate was reported at 30° incidence angle as compared to 90°. No analyses on residual stresses or texture of the coatings have been provided which can further explain the behavior of the TiN coating system.

7.3. On the design of erosion resistant coatings

7.3.1. Correlation between H^3/E^2 and erosion rate

Elastic deformation and resistance to plastic deformation should be offered by protective coatings during solid particle contact. Hence protective coatings should possess low Elastic Modulus (E) and high hardness (H). A high hardness will provide resistance against penetration whereas low Elastic Modulus will distribute load on a large area [144]. In order to simulate contact behavior, Johnson proposed a model where a load P_y is needed to initiate plastic deformation in a flat plane with a rigid sphere of radius 'r'. The contact analysis of the two rigid body lead to the following relationship:

$$P_y = 0.78 r^2 (H^3/E^2)$$

Hence, a direct relation between plasticity of the material and material parameters (Hardness and E-Modulus) was obtained. Literature indicates H^3/E^2 as a parameter which controls the resistance of a material against plastic deformation [145-147]. In the present discussion, the relationship between erosion rate and H^3/E^2 was analyzed.

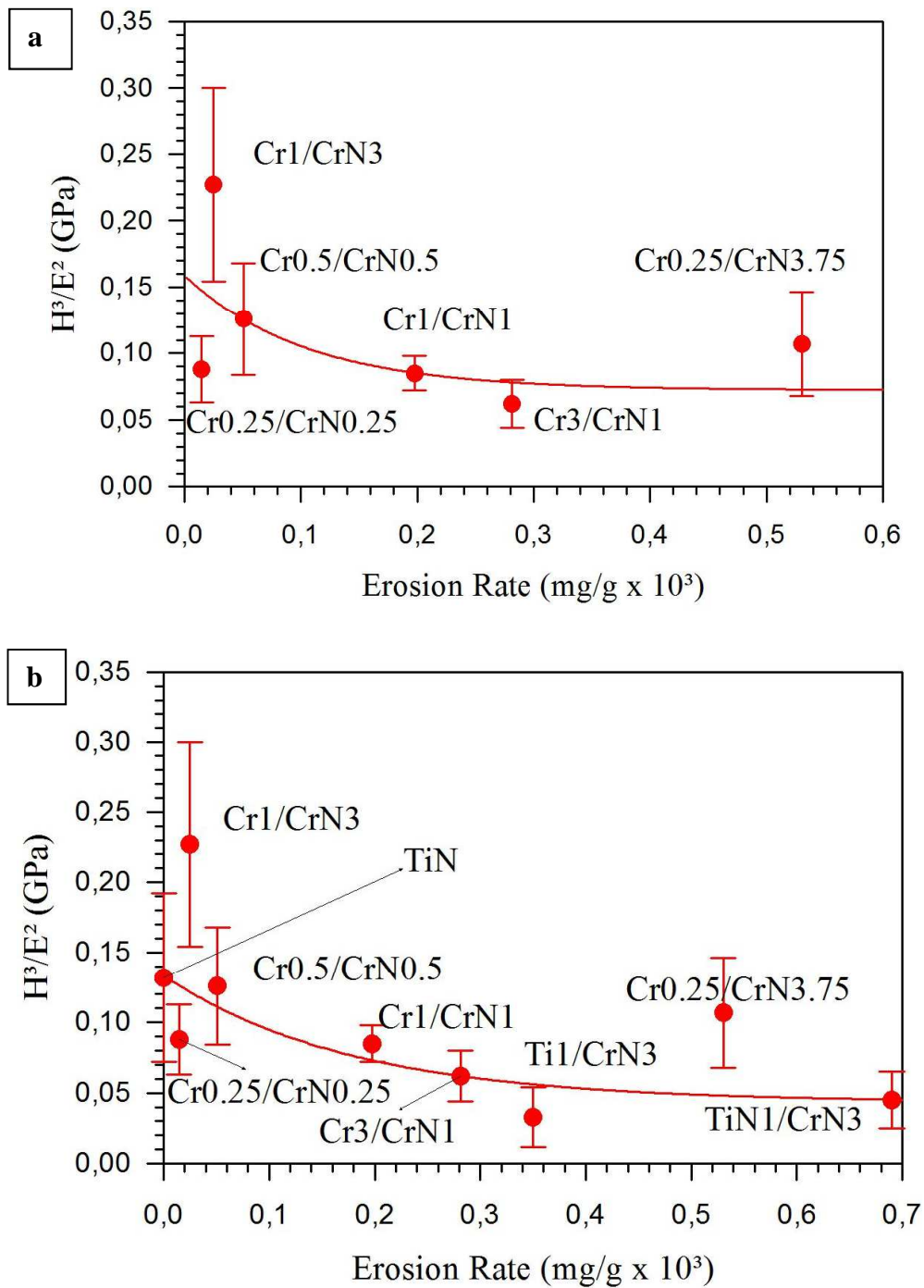


Figure 7.19: Relationship between Erosion rate and mechanical properties of coatings (a) Cr/CrN coatings (b) all tested single layer and multilayer coatings

Fig. 7.19a,b illustrates the relationship between H^3/E^2 and the erosion rate for various coatings. Erosion rates were calculated for 60 minutes at an incidence angle of 30° . A comparison of the erosion behavior of various Cr/CrN coatings is given in Fig. 7.19a. An exponential decay of the trend line with increasing H^3/E^2 values can be seen. A fit of 20% was estimated for the Cr/CrN coatings through the data fit. In the second analysis, a correlation between H^3/E^2 and the erosion rate between the tested Cr/CrN coatings, Ti/CrN, TiN/CrN and TiN coatings is shown (Fig 7.20b). A fit of 26% is obtained by

a non-linear regression analysis in this case. The four exceptions Cr0.25/CrN0.25, Cr1/CrN3, Cr0.25/CrN3.75 and Ti1/CrN3 did show almost no correlation with the plotted trend. Previous analysis revealed that the Cr0.25/CrN0.25 coating show a low H^3/E^2 value with high adhesion on the substrate (Section 5.3). Contrarily, in case of Cr0.25/CrN3.75, extremely low adhesion (Section 5.3) values were measured for this coating along with a low H^3/E^2 . In case of Cr0.25/CrN0.25 and Ti1/CrN3 high adhesion values were estimated (Section 5.3). As available from this data (Fig. 7.19 a,b), coatings with exceptional good/worse properties do not fit with the trend line. The comparison of the two illustrations provides similar mathematical functions. Hence, it can be concluded that Johnson's model can be an optimum method in order to study the erosion behavior of coatings with an assumption that the coating adhesion and the mechanical properties (Hardness/E-Modulus) should be high enough. A similar type of analysis has been conducted by Bousser [18]. He analyzed the erosion rates of CrN, TiN and TiSiN coatings against hardness of the coating (H), elastic strain to failure (H/E) and onset of plastic deformation to failure (H^3/E^2). He identified the hardness of the coating (H) as the best fit for this relationship (87%) was found for followed by a H^3/E^2 (44%) and H/E (10%).

7.3.2. Effect of elastic mismatch between coating and substrate

Deposition of hard coatings on soft substrates enhances the wear resistance of coatings but such a combination can also lead to interface problems. Deposition of coatings on substrates lead to high residual stresses due to thermal or elastic mismatch between the coating and substrate (E_c/E_s). These stresses can result to buckling and spalling of coatings [148]. Lee reported that maximum tensile stress occurs at the surface of the coating when E_c/E_s ratio was less than 1.5 whereas for E_c/E_s ratio greater than 1.5, these stresses were found to be on the coating-substrate interface [148]. Difference in Elastic Modulus between coating (E_c) and substrate (E_s) also play an important role in determining the critical load of a coating. For a soda-lime glass coating an increase in E_c/E_s ratio lead to a decrease in the critical load resulting in fast delamination of the coating. Coatings with an $E_c/E_s > 5$ prefer to laminate with the initiation of radial cracks. An $E_c/E_s < 5$ leads to cone cracks whereas $E_c/E_s < 1$ (highly stiff substrates) are resistant against initiation of radial fractures [2]. A similar type of model has been proposed by Miranda et. al. [149] defining elastic mismatch between coating and substrate as a critical factor in brittle coatings. In Fig. 7.20, the quotient of ratio of yield strength of substrate (Y_c) and tensile stress of coating (Sc) as a function of the elastic mismatch modulus can be seen. According to the authors the tensile stresses/von Mises stresses generated within the coating and coating-substrate interface is responsible for the type of crack propagation within the coatings system. Moreover, knowledge about the yield strength of coating and substrate would help to localize if the yielding takes place within the substrate or coating. If, the elastic mismatch modulus is unity ($E_c/E_s=1$), the stresses present at the coating-substrate interface will decide regarding the yielding in coating or substrate. For high stresses at the interface, yielding starts from the coating going towards the substrate. In case of

soft coating on hard substrate ($E_c/E_s < 1$) yielding starts from the substrate [149]. Similar type of analysis has been conducted by various researchers where the formation of radial or cone cracks after loading is dependent on the E_c/E_s ratio [150].

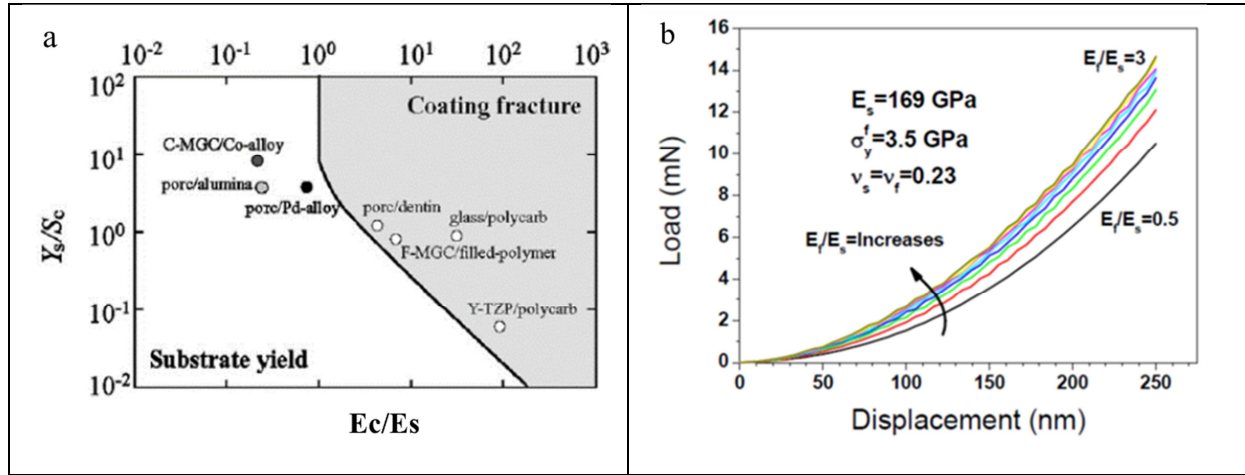


Figure 7.20: Influence of elastic-modulus ratio on the (a) substrate-coating fracture (b) force-displacement response

A relationship between the quotients elastic modulus ratio of the coating to substrate and ratio of yield strength of substrate to tensile stresses in coatings can be observed in Fig. 7.20b. FEM simulations were performed for a substrate with an E-Modulus of 169 GPa. E-modulus of coating was varied between 84.5 GPa and 507 GPa. With increase in E_c/E_s ratio, higher load is required to achieve a similar penetration depth. A higher elasticity is achieved when the increase in E_c/E_s ratio results in resistance against plastic deformation. Such a type of behavior is expected for hard coatings on softer substrates. In case of soft coatings and hard substrates ($E_c/E_s < 1$) lower loads are required for the onset of plastic deformation. For such systems a pileup effect is observed during the nanoindentation process and no plastic deformation of the substrate (shear-step effect) is expected after the erosion due to the higher hardness of substrate [151].

Coatings System	E_f/E_s	Dominant Erosion Mechanism
Inconel 718	E_s : 241.2	-
Cr1/CrN3	0.38	Crack deflection, Lateral cracks
Cr3/CrN1	1.17	Plasticity of Substrate/ No clear radial or lateral cracks observed
Cr1/CrN1	1.32	Lateral/ Radial Cracks
Cr0.25/CrN0.25	1.23	Lateral Cracks
Cr0.5/CrN0.5	1.04	Lateral/radial cracks
Cr0.25/CrN3.75	1.25	Lateral cracks

Ti1/CrN3	1.39	Lateral /radial cracks
TiN1/CrN3	1.55	Lateral /radial cracks
TiN	1.486	Plasticity of Substrate/Inter/Intra columnar cracks, shear sliding of columns

Table 7-1: Dominant erosion mechanisms observed due to E_c/E_s ratios

In the current study a correlation between the elastic mismatch ratio (E_c/E_s) and the dominant erosion mechanism in the single and multilayer coatings was requested. A low E_c/E_s value for the Cr1/CrN3 coating (Table 7-1) proved the presence of lateral cracks at an impact angle of 30° . Radial/cone cracks have been observed for the same coating at an impact angle of 90° . In other multilayer coatings, the elastic mismatch was found in the range of 1-1.5 showing a dominant presence of radial or lateral cracking. In case of single layer TiN coating, no radial cracks were visible. The dominant coating mechanism was inter/intra columnar crack generation. Nanoindentation theories cannot be idealized to describe the erosion behavior of coatings but a nanoindentation theory can be used to understand the contact behavior between particle/coating, substrate/coating or coating/coating. For all most all the calculated E_f/E_s ratios a combination of radial and lateral cracks has been observed which is in contrast to the nanoindentation theories. Substrate deformation (shear step) can be seen for a E_f/E_s ratio of 0.38 (Cr1/CrN3) which is proved from the model proposed in Fig. 7.20b. On contrary, presence of shear steps can also be found for TiN coatings ($E_f/E_s = 1.486$). Erosion investigation has been performed at various incidence angles leading to different wear mechanisms for high speed particles. In case of nanoindentation, a defined low speed indentation is opted for the measurements which makes the technique incomparable with erosion testing.

7.3.3. Effect of modulus mismatch between consecutive layers

The influence of effect of elastic mismatch of bilayers on the crack propagation can be understood from contact mechanics. Generally, a FEM model consisting of a substrate with a single or multilayer is used which is indented using a spherical rigid indenter with various forces. The elastic properties of the substrate and coatings (Elastic Modulus and Poisson ratio) are varied in order to observe various indentation effects and to identify the weak positions within a coating system. These weak positions are addressed to be the locations where spalling of the coating can take place. Lardner et. al. [152] found that the E-Modulus of top layer (E_1) and consecutive coating layer (E_2) play a vital role in understanding the load absorption capability of the coating. They concluded that with the help of E_1/E_2 ratio it is possible to localize if the maximum tensile stresses and shear stresses between the coating-coating or at the substrate-coating interface.

	E1-E2 (GPa)	Erosion Rate @30° (mg/g)	Erosion Rate @ 90° (mg/g)
Cr1/CrN3	112.42	0	2.52
Ti1/CrN3	12.23	0.84	0.84
TiN1/CrN3	275.25	1.8	1.8

Table 7-2: Comparison of erosion rates for various coatings

An analysis of the relationship between modulus mismatch between CrN and Cr,Ti, TiN is depicted in Table 7-2. No direct relationship between elastic modulus mismatch and the erosion rates at 30° and 90° incidence angles can be seen. Since erosion is a combination of various wear processes like cutting, chipping, elastic deformation, shearing etc. therefore no clear statement can be made on the relationship between two parameters. Hence, it can be assumed that a correlation between modulus of mismatch and a wear process can be provided when a single form of wear process takes place. A similar type of analysis has been conducted by Borawski et.al. [153]. He tested TiAlN coatings with a combination of metallic interlayers (T, Zr, Hf, Nb). No clear trends between the elastic mismatch modulus and the erosion rate were found for the multilayer coatings when eroded with glass and Al₂O₃ particles.

In order to discuss the effect of elastic modulus mismatch, it is necessary to understand the coating structure of various coatings. In case of Cr/CrN multilayer coating, a growth of CrN layer ($E = 195.75 \pm 25.17$) takes place on the Cr layer (308.17 ± 22.24). The CrN coating shows a combination of bcc and hexagonal structure whereas the Cr layer consists of a bcc structure. Similarly in case of Ti/CrN coating, the CrN coating was deposited on a hexagonal Ti ($E = 183.42 \pm 51.52$ GPa) layer and in TiN/CrN on a TiN ($E = 470 \pm 67.56$ GPa) fcc structure. In all the cases CrN was the topmost layer in the coating system. If crack propagation starts from the top most layer (CrN), the bcc and hexagonal phases will decide the direction and the crack arrest intensity of crack propagation. If the consecutive layer offers a change in crystal structure, a resistance or change in crack direction would be offered to the incoming crack. If the crystal structure of the consecutive layer is similar to that of the CrN coating, low/no resistance against crack propagation is expected. It is important to mention that not only the crystal structure is the deciding factor for the control of crack propagation but material properties like fracture toughness (K_{IC}) plays an equal important role in this case. If a radial crack at the substrate-coating interface takes place during the wear process, the mechanical properties of the coating intact with the substrate will decide on the crack propagation behavior of the crack. A detailed study on the macro-crack propagation with materials of various structures has been performed by Lipperman et. al. [154]. With the help of FEM simulations, the authors were able to prove that in a triangular structure, crack propagation has only one crack type which can propagate in three possible directions. In case of hexagonal structure, three different types of cracks can take place with three possible directions. Hence 9 possible propagation paths were proposed for a hexagonal structure.

Stress intensity factor and the material properties were some of the factors influencing the propagation paths of a crack.

Literature also refers to some of the fracture mechanics factors known as Dunders Parameters α , β which are responsible for the characteristics of coatings in a bilayer period. Parameter α refers to the extensional stiffness between two materials whereas β shows a mismatch in the volumetric stiffness. These parameters based on Elastic Modulus and Poisson ratios of two or more materials [155]. Lower values of Dunders parameter indicate larger elastic mismatch leading to shield crack propagation within the interlayer [156].

8. Conclusions and future prospects

Erosion of turbine components due to solid particle impact has been identified as a major problem. Replacement of such components leads to high investment costs and low mean-time-between-overhaul. The most popular method to reduce wear of such components is the application of coatings providing a protection due to their special properties. In the present work, various PVD coatings have been developed in order to study and understand the erosion behavior of coatings. Single layer as well as multilayer coatings have been deposited in a magnetron sputtering coater and subsequently tested under defined testing conditions.

The deposition parameters used for the PVD magnetron sputtering process play a vital role the coating growth resulting in variation in mechanical properties. In case of reactive gas sputtering, the ratio between N_2/Ar causes the formation of more or less hard phases leading to increase or decrease in hardness of the coatings. Chamber pressure, substrate bias and cathode power seem to influence the growth of the coating too. In case of Cr/CrN multilayer coatings, some coatings prefer the formation of CrN phase whereas in other systems a combination of CrN and Cr_2N was analyzed by means of diffractometry. A stable formation of CrN because of lower binding energies was found using an XPS analysis resulting in a high probability for the formation of CrN phase in contrast to Cr_2N . In case of

single layer TiN coatings, only the presence of pure TiN phase was detected from the diffractograms. Formation of CrN, TiN and a mixture of Cr and Ti phases were received during the deposition of Ti/CrN and TiN/CrN phases. Similar to single layers, the mechanical properties of multilayer coatings were affected by various phase formations within the coatings. The formation of Cr_2Ti has also been reported during the deposition of Ti/CrN and TiN/CrN coatings which is responsible for embrittlement of the structure resulting in deterioration of mechanical properties. Hence, the selection of optimum deposition parameters, change in bilayer period, reduction or increase in the thickness of the alternating deposited layers etc. formation of unwanted phases can be avoided. This would lead to better mechanical properties for the particular application.

Detailed investigation on the erosion behavior of Cr/CrN, CrN/X (X= Ti, TiN) and single layer TiN coating has been performed in this research work. The erosion behavior of the above discussed coatings varies with variable testing conditions. A change in erosion mechanisms with the changing incidence angle was proved. Dominant lateral cracking was detected while erosion at low angles whereas a dominant radial and Hertzian cracking took place at normal angles. A change in bilayer period of the Cr/CrN multilayer showed a visible effect on the erosion behavior of those coatings. Contrary to the Cr1/CrN3 coating, Ti1/CrN3 and TiN1/CrN3 coatings did not show erosion protection against sand erosion. TiN monolayer coating on the other hand showed no erosion at low angles and almost no protection at normal angles.

A relationship between H^3/E^2 and erosion rate of the coating was discussed in the last sections. Low fit of the data between the two parameters but a logarithmic decreasing trend can be seen. Low adhesion and low values of H^3/E^2 due to high Elastic Modulus were identified as some of the factors which lead to low correlation between the two factors. Analysis on the elastic mismatch between coating and substrate show that E_c/E_s is a useful method in analyze to define nanoindentation processes but no relation was found for this parameter for erosion wear processes. Similarly, a relationship between differences of Elastic Modulus of consecutive layers in a multilayer coating was studied. No direct relationship between erosion rates was and difference in E-Modulus and erosion rates at low as well as at oblique angles. This effect was again referred to the various wear mechanisms occurring at different incidence angles.

Fracture toughness of coatings plays an important role in order to forecast the behavior of hard coatings. In the present research work, effort has been made in order to estimate the fracture toughness of coatings. Unfortunately, no success has been achieved through the nanoindention methods. Literature hints the use of a 4-point bending test as an alternative method to estimate the fracture toughness of coatings. Hence, analytical methods like 4-point bending test can be used to address the important parameters like fracture toughness and another material parameters to forecast the properties of the coatings. Alternative to scratch tests, 4-point bending tests have also been used to estimate the adhesion of coatings on a substrate.

Another important aspect which influences the behavior of multilayer coatings is the adhesion between two consecutive layers. The interface toughness between two consecutive layers can be analyzed through Nano indentation or bending tests. This would allow to identify the weak points within the coatings and to explain the wear mechanism. An estimation of Dunders Parameters (fracture mechanics) can also be considered as an alternative method to understand the combined behavior of two consecutive deposited layers and their influence on the wear behavior.

Coatings with high hardness and low E-Modulus have been established as the best candidates for wear applications. In order to improve the hardness of Cr, Ti/CrN multilayer coatings, the CrN ceramic layer can be replaced using harder TiN, TiAlN, TiAlCrN or TiAlSiN coatings. The hardness value of these coatings ranges to between 28-60 GPa as compared to 20 GPa for CrN coating. On the other hand, replacement of CrN with other possible hard coatings can lead to high stresses due to elastic/thermal mismatch. Moreover, high Elastic Modulus values have been reported for the described hard coatings. Hence an optimum combination of high hardness, low Elastic Modulus and optimum stress values should be obtained for wear applications.

Understanding the structural strength and weaknesses can be a suitable method to analyze the wear behavior of multilayer coatings. The deposition of consecutive layers with different mechanical properties leads to variation in the coating structure during growth of the coatings. This results in different mechanical and chemical properties of the coatings with the variation of depth. Hence a detailed structural examination of coating can be an effective method to study the behavior of multilayer coatings. Transmission Electron Microscopy (TEM) can be an effective to study the coating structure, porosity, crystal structure and size and orientation of the coating layers. TEM analyses on the growth of coatings at various deposition process parameters, deposition methods and effects on coating growth due to various substrates are intended for the future.

References

1. Naraparaju, R., U. Schulz, and C.C. Büttner, *High Temperature Oxidation Stability of Aerodynamically Optimised Riblets for Blades of Aero-engine Applications*. Oxidation of Metals, 2015. **83**(1-2): p. 133-150.
2. Hetmanczyk, M., L. Swadzba, and B. Mendala, *Advance materials and protective coatings in aero-engines application*, in *Journal of achievements in materials and manufacturing engineering*. 2007. p. 372-381.
3. Hamed, A., W. Tabakoff, and R. Wenglarz, *Erosion and deposition in turbomachinery*. Journal of Propulsion and Power, 2006. **22**(2): p. 350-360.
4. Walt, J.P.v.d. and A. Nurick, *Erosion of dust-filtered helicopter turbine engines, Part 1: Basic theoretical considerations* Journal of Aircraft, 1995. **32**(1): p. 106-111.
5. Muboyadzhyan, S.A., *Erosion-Resistant coatings for gas turbine compressor blades*. Russian Metallurgy, 2009. **2009**(3): p. 3-20.
6. Yang, Q., et al., *Erosion resistance performance of magnetron sputtering deposited TiAlN coatings*. Surface and Coatings Technology, 2004. **188-189**: p. 168-173.
7. Gachon, Y., et al., *Erosion by solid particles W/W-N multilayer coatings obtained by PVD process*. Surface and Coatings Technology, 1999. **113**(1-2): p. 140-148.
8. Panich, N., et al., *Tribological study of nano-multilayered Ultra-hard coatings based on TiB₂*. Revised Advanced Material Science, 2006. **13**: p. 117-124.
9. Lee, S.G., et al., *Product lifecycle management in aviation maintenance, repair and overhaul*. Computers in Industry, 2008. **59**(2-3): p. 296-303.
10. Brendel, T., et al. *MTU solutions against erosive attack and loss of EGT margin in turbo engines -ERCoatnt*. 2008.
11. Branco, J.R.T., et al., *Solid particle erosion of plasma sprayed ceramic coatings*. Materials Research, 2002. **7**(1): p. 147-153.
12. Aquaro, D., *Erosion due to the impact of solid particles of materials resistant at high temperature*. Meccania, 2006. **41**: p. 539-551.
13. Westergard, R., et al., *The erosion and abrasion of alumina coatings plasma sprayed under sprayed coatings*. Tribology International, 1998. **31**(5): p. 271-279.
14. Hamed, A.A., et al., *Turbine Blade Surface Deterioration by Erosion*. Journal of Turbomachinery, 2005. **127**: p. 445-452.
15. Bons, P.J., et al. *The many faces of turbine surface roughness*. in *Proceedings of ASME Turbo Expo*. 2001. New Orleans.
16. Ghenaïet, A., S.C. Tan, and R.L. Elder. *Prediction of an axial turbomachine performance degradation due to sand ingestion*. in *IMEchE*. 2005.
17. Uihlein, T.J., et al., *Erosionsschutz in Triebwerksverdichtern- Ein Beitrag zur CO₂-Reduktion*, M.A.E. GmbH, Editor. 2012.
18. Bousser, E., *Solid Particle Erosion Mechanisms of Protective Coatings for Aerospace Application*, in *Department of Physics*. 2013, Ecole Polytechnic Montreal.
19. Oka, Y.I., K. Okamura, and T. Yoshida, *Practical estimation of erosion damage caused by solid particle impact, Part 1: Effects of impact parameters on a predictive equation*. Wear, 2005. **259**(2005): p. 95-101.
20. Levy and Chick, *Effect of erodent composition and shape on erosion of steel*. Wear, 1983. **89**(2): p. 151-162.
21. Roy, M., *Elevated temperature erosive wear of metallic materials*. Journal of Applied Physics, 2006. **39**: p. 101-124.
22. Hutchings, I.M. *Ductile-brittle transitions and wear maps for the erosion and abrasion of brittle materials*. 1992.
23. Maurer, C. and U. Schulz, *Erosion resistant titanium based PVD coatings on CFRP*. Wear, 2013. **302**: p. 937-945.

24. ElTobgy, M.S., E. Ng, and M.A. Elbestawi, *Finite element modelling of erosive wear*. International Journal of machine tools and manufacture 2005. **45**: p. 1337-1346.
25. Tilly, G.P., *A two stage mechanism of ductile erosion*. Wear, 1973. **23**: p. 87-96.
26. Yerramareddy, S. and S. Bahadur, *Effect of operational variables, microstructure and mechanical properties on the erosion of Ti-6Al-4V*. Wear, 1991. **142**: p. 253-263.
27. Finnie, I., *Erosion of surfaces by solid particles*. Wear, 1960. **3**: p. 253-258.
28. Finnie, I., Wolak, and Kabil, *Erosion of surfaces by solid particles*. Journal of materials, 1967. **2**(3): p. 682-700.
29. Li, C.-J., G.-J. Yang, and A. Ohmri, *Relationship between Particle Erosion and Lamellar Microstructure for Plasma-Sprayed Aluminium Coatings*. Wear, 2006. **260**: p. 1166-1172.
30. Torrance, A.A., *Modelling abrasive wear* Wear, 2005. **258**(281-293): p. 281-293.
31. Arnell, R.D., P.J. Kelly, and J.W. Bradley, *Control of structure and properties of coatings deposited by pulsed magnetron sputtering*, in *Nanostructured thin films and nanodispersion strengthened coatings*, A.A. Voevodin, et al., Editors. 2003. p. 183-192.
32. Bielawski, M., *Residual stress Evaluation in TiN Coatings Used for Erosion Protection of Aerospace Components*. Materials Science Forum, 2006. **524-525**: p. 867-872.
33. Anand, K., *Flue Effects in Solid Particle Erosion*. Wear, 1987. **118**: p. 243-257.
34. Shewmon, P.T., *Particle size threshold in erosion of materials*. Wear, 1981. **68**: p. 253-258.
35. Kleis, I., *Probleme der Bestimmung des Strahlverschliessness bei Metallen*. Wear, 1960. **13**(3): p. 199-215.
36. Neilson, J.H. and A. Gilchrist, *An experimental investigation into aspects of erosion in rocket motor tail nozzles*. Wear, 1968. **11**(2).
37. Wang, Y.-F. and Z.-G. Yang, *Finite element model of erosive wear on ductile and brittle materials*. Wear, 2008. **265**: p. 871-878.
38. Aquaro, D. and E. Fontani, *Erosion of ductile and brittle materials*. Meccania, 2001. **36**: p. 651-661.
39. Nicolaus, M. and M. Schäpers, *Grundlagen der Dünnschichttechnologie*, in *Moderne Beschichtungsverfahren*. 2005, Wiley-VCH Verlag GmbH & Co. KGaA. p. 35-55.
40. Kelly, P.J. and R.D. Arnell, *Magnetron Sputtering: a review of recent developments and applications* Vacuum, 2000. **56**: p. 159-172.
41. Svaokovski, I.V., D.A. Golosov, and S.M. Zavatsiky, *Characterisation parameters for unbalanced magnetron sputtering systems*. Vacuum, 2002. **68**: p. 283-290.
42. Olaya, J.J., S.E. Rodil, and S. Muhl, *Comparative study of niobium nitride coatings deposited by unbalanced and balanced magnetron sputtering*. Thin Solid Films, 2008. **516**: p. 8319-8326.
43. D.A., G., M. S.N., and Z. S.M., *Effects of Magnetic System Unbalance on Magnetron Sputtering Characteristics*. Plasma Physics and Technology, 2014. **1**(2): p. 62.
44. ev, A.A.S., et al., *Investigation of Plasma Characterization in an Unbalanced Magnetron Sputtering System*. Plasma Physics Report, 2009. **35**(5): p. 406.
45. Risse, A., *Beschichten*, in *Fertigungsverfahren der Mechatronik, Feinwerk- und Präzisionsgerätetechnik*. 2012, Springer: Berlin.
46. Höglund, C., *Reactive magnetron sputter deposition and characterization of thin films from the Ti-Al-N and Sc-Al-N systems*, in *Thin Film Physics Division*. 2008, Linköping University: Linköping. p. 54.
47. Musil, J., et al., *Reactive magnetron sputtering of thin films: present status and trends*. Thin Solid Films, 2005. **475**: p. 208-218.
48. Kadlec, S., J. Musil, and H. Vyskocil, *Hysteresis effect in reactive sputtering: a problem of system stability*. Journal of Applied Physics, 1986. **19**: p. 187-190.
49. Beanland, R., D.J. Dunstan, and P.J. Goodhew, *Plastic relaxation and relaxed buffer layers for semiconductor epitaxy*. Advances in Physics, 1996. **45**(2): p. 87-146.
50. Floro, J.A., et al., *Physical Origins of Intrinsic Stresses in Vomer- Weber Thin Films*, in *MRS Bulletin*. 2002.
51. Baskaran, A. and P. Smereka, *Mechanisms of Stranski-Krastanov*. Journal of Applied Physics, 2012. **111**.

52. Othaman, Z., et al., *The Stranski-Krastanov Three Dimensional Island Growth Prediction on Finite Size Model*.
53. Movchan, B.A. and A.V. Demchishin, *Structure and Properties of Thick Condensates of Nickel, Titanium, Aluminium Oxides and Zirconium Dioxide in Vacuum*. Fiz. Metal. Metalloved. 28, 1969. **28**: p. 653-660.
54. Hultman, L. and J.E. Sundgren, *Structure/Property Relationships for Hard Coatings*, in *Handbook of Hard Coatings*, G.E. McGuire, S.M. Rossnagel, and R.F. Bunshah, Editors. 2001.
55. Anders, A., *A Structure Zone Diagram Including Plasma Based Deposition and Ion Etching*. Thin Film Solids, 2009. **518**(15): p. 4087-4090.
56. Thornton, J.A., *High rate thick film growth*. Annual Review Material Science, 1977: p. 239-259.
57. Barna, P.B. and M. Adamik, *Fundamental structure forming phenomena of polycrystalline films and the structure zone models*. Thin solid films, 1998. **317**(1-2): p. 27-33.
58. Thompson, C.V., *Structure Evolution During Processing of Polycrystalline Films*. Annual Review Material Science, 2000: p. 159-90.
59. Barna, P.B. and A. Adamik, *Formation and Characterization of the structure of the Surface Coatings*, in *Protective Coatings and Thin Films*. 1996. p. 279-298.
60. Thornton, J.A., *Influence of apparatus geometry and deposition conditions on the structure and topography of thick sputtered coatings*. Journal of Vacuum Science & Technology, 1974. **11**(4): p. 666-670.
61. Freund, L.B. and S. Suresh, *Thin Film Materials*. 2003: Cambridge.
62. Messier, R., A.P. Giri, and R.A. Roy, *Revised Structure Zone Model for Thin Film Physical Structure*. Journal of Vacuum Science Technology, 1983. **A2**(2): p. 500-503.
63. Levy, A.V. and W. Buqian, *Erosion of hard material coating system*. Wear, 1988. **121**(3): p. 325-346.
64. Maurer, C. and U. Schulz, *Solid particle erosion of thick PVD coatings on CFRP*. Wear, 2014. **317**(1-2): p. 246-253.
65. Schroeter, O., *Herstellung und Charakterisierung von PVD-Schichten auf Basis der Cr₂AlC-MAX-Phase*, in *Metallkunde und Werkstofftechnik*. 2011, Brandenburgische Technische Universität.
66. Wei, R., et al., *Erosion resistance of thick nitride and carbonitride coatings deposited using plasma enhanced magnetron sputtering*. Plasma Processes and Polymers, 2007. **4**(1): p. 694.
67. Wheeler, D.W. and R.J.K. Wood, *Fracture of diamond coatings by high velocity sand erosion*. Philosophical Magazine, 2009. **89**(3): p. 285-310.
68. Veprek, S. and M.G. Veprek-Heijman, *Industrial applications of superhard coatings nanocomposite coatings*. Surface and Coatings Technology, 2008. **202**(21): p. 5063-5073.
69. Kwasny, W., *Predicting properties of PVD and CVD coatings based on fractal quantities describing their surfaces*. Journal of Achievements in Materials and Manufacturing Engineering, 2009. **37**(2): p. 128.
70. Holleck, H. and V. Schier, *Multilayer PVD coatings for wear protection*. Surface and Coatings Technology, 1995. **76-77**(1): p. 328-336.
71. Feuerstein, A. and A. Kleyman, *Ti-N multilayer systems for compressor airfoil and sand erosion protection*. Surface and Coatings Technology, 2009. **204**(6-7): p. 1092-1096.
72. Quensnel, E. and Y. Pauleau, *Tungsten and tungsten-carbon PVD multilayered structures as erosion-resistant coatings*. Surface and Coatings Technology, 1993. **62**: p. 474-479.
73. Aperador, W., C. Ramirez, and J.C. Caicedo, *The effect of TiCV/TiNbCN coating on erosion-corrosion resistance*. Ingenieria e Investigacion, 2012. **32**(2): p. 6-11.
74. Aquaro, D., *Impact of Solid Particulate on Brittle Materials*. Journal of Mechanical Engineering, 2010. **56**: p. 275-283.
75. Jiang, J. and R.D. Arnell, *The effect of substrate roughness on the wear of DLC coatings*. Wear, 2000. **239**: p. 1-9.
76. Hassani, S., et al., *Predictive tools for the design of erosion resistant coatings*. Surface and Coatings Technology, 2008. **203**: p. 204-210.

77. Ramalingam, S. and L. Zhemng, *Film-substrate interface stresses and their role in the tribological performance of the surface coatings*. Tribology International, 1995. **28**(3): p. 145-161.
78. Al Mohammad, A., *Effect of substrate structures on epitaxial growth and electrical properties of WO₃ thin films deposited on and (0001) α -Al₂O₃ surfaces*. Vacuum, 2009. **83**(11): p. 1326-1332.
79. Han, Z., et al., *Effects of Thickness and Substrate on the Mechanical Properties of Hard Coatings*. JCT Research, 2004. **1**(4): p. 337-341.
80. Spieß, L., et al., *Methoden der Röntgenbeugung*, in *Moderne Röntgenbeugung*. 2008, Vieweg + Teubner. p. 190.
81. Robinson, K.S. and P.M.A. Sherwood, *X-Ray photoelectron spectroscopic studies of the surface of sputter ion plated films*. Surface and Interface Analysis, 1984. **6**(6): p. 261-266.
82. Nowotnik, A., et al., *Mechanical properties of hot deformed Inconel 718 and X750*. Journal of Achievements in Materials and Manufacturing Engineering, 2012. **50**(2).
83. Liu, W.C., M. Yao, and Z.L. Chen, *Effect of cold rolling on the precipitation behavior of δ phase in INCONEL 718*. Metallurgical and Materials Transactions A, 1999. **30**(1): p. 31-40.
84. Wieceński, P., et al., *Erosion resistance of the nanostructured Cr/CrN multilayer coatings on Ti6Al4V alloy*. Vacuum, 2014. **107**(0): p. 277-283.
85. Purandare, Y.P., A.P. Ehasarian, and P.E. Hovesepian, *Deposition of nanoscale multilayer CrN/NbN physical vapor deposition coatings by high power impulse magnetron sputtering*. Journal of Vacuum Science & Technology, 2008. **26**(2): p. 288.
86. Perucca, M., et al., *Cast iron cutting with nano TiN and multilayer TiN-CrN coated inserts*, in *International Conference on Structural Nano Composites*. 2004. p. 1.
87. Fan, Y.D., et al., *Microscopic model for columnar growth of thin films*. physica status solidi, 1992. **134**(1): p. 157-166.
88. Krell, A.K., *Cavitation erosion resistance of Ti/TiN multilayer coatings*. Surface and Coatings Technology, 2013. **228**: p. 115-123.
89. Deng, J., et al., *Erosion wear of CrN, TiN, CrAlN and TiAlN nitride coatings*. International Journal of Refractory Metals and Hard Metals, 2012. **35**(10-16).
90. William, D.S., et al., *Nitrogen, oxygen and argon incorporation during reactive sputtering of titanium nitride*. Journal of Vacuum Science and Technology, 1987. **5**(6).
91. Daniel, R., et al., *The origin of stresses in magnetron-sputtered thin films with zone T structures*. Acta Materialia, 2010. **58**: p. 2621-2633.
92. Rebenne, H.E. and D.G. Bhat, *Review of CVD TiN coatings for wear-resistant applications: deposition processes, properties and performance*. Surface and Coatings Technology, 1993. **63**: p. 1-13.
93. Zhang, S., *TiN coating of tool steels: a review*. Journal of Materials Processing Technology, 1993. **39**: p. 165-177.
94. Chen, Y.-H., et al., *Synthesis and structure of smooth, superhard TiN/SiNx multilayer coatings with an equiaxed microstructure*. Surface and coatings Technology, 2001. **146-147**: p. 209-214.
95. Petrov, I., et al., *Microstructural evolution during film growth*. Journal of vacuum science technology, 2003. **21**(5): p. 117-128.
96. Leyland, A. and A. Matthews, *On the significance of the H/E ratio in wear control: a nanocomposite coating approach to optimised tribological behaviour*. Wear, 2000. **246**(1-2): p. 1-11.
97. Johnson, K.L., *Contact Mechanics*. 2001.
98. Lawn, B.R., A.G. Evans, and D.B. Marshall, *Elastic/Plastic indentation damage in ceramics: The median/radial crack damage*. American ceramic society 1980. **63**(9-10): p. 579.
99. Nie, X., et al., *Thickness effects on the mechanical properties of micro-arc discharge oxide coatings on aluminium alloys*. Surface and Coatings Technology, 1999. **116-119**(0): p. 1055-1060.
100. Ichimura, H. and A. Rodrigo, *The correlation of scratch adhesion with composite hardness for TiN coatings*. Surface and Coatings Technology, 2000. **126**(2-3): p. 152-158.

101. Lin, J., et al., *Modulated pulse power sputtered chromium coatings*. Thin Solid Films, 2009. **518**(5): p. 1566-1570.
102. Clyne, T.W. and S.C. Gill, *Residual stresses in thermal spray coatings and their effect on interfacial adhesion: A review of recent work* Journal of Thermal Spray Technology, 1996. **5**(4): p. 401-412.
103. Materials, A.S.o.T., *Standard Test Method for Adhesion Strength and Mechanical Failure Modes of ceramic coatings by Quantitative Single Point Scratch Testing*. 2010. p. 1-28.
104. Bull, S.J., *Failure modes in scratch adhesion testing* Surface and Coatings Technology, 1991. **50**: p. 25-32.
105. Lawn, B.R., *Indentation of Ceramics with Spheres: A Century after Hertz*. Journal of the American Ceramic Society, 1998. **81**(8): p. 1977-1994.
106. Wei, G., A. Rar, and J.A. Barnard, *Composition, structure, and nanomechanical properties of DC-sputtered CrNx ($0 \leq x \leq 1$) thin films*. Thin Solid Films, 2001. **398-399**(0): p. 460-464.
107. H.Holleck and H.Schulz, *Preparation and behaviour of wear-resistant TiC/TiB₂, TiN/TiB₂ and TiC/TiN coatings with high amounts of phase boundaries*. Surface and Coatings Technology, 1988. **36**: p. 707-714.
108. Seok, J.W., N.M. Jadeed, and R.Y. Lin, *Sputter-deposited nanocrystalline Cr and CrN coatings on steels*. Surface and Coatings Technology, 2001. **138**: p. 14-22.
109. Ghosh, M. and S. Chatterjee, *Diffusion bonded transition joints of titanium to stainless steel with improved properties*. Materials Science and Engineering: A, 2003. **358**(1-2): p. 152-158.
110. Launey, M.E. and R.O. Ritchie, *On the fracture toughness of advanced materials*. Advanced Materials, 2009. **21**: p. 2103-2110.
111. Ovid'ko, I.A., *Review on the fracture processes in nanocrystalline materials*. Journal of Materials Science, 2007. **42**(5): p. 1694-1708.
112. Zhang, S., D. Sun, and X.L. Bui, *Magnetron Sputtered Hard and Yet Tough Nanocomposite coatings with Case Studies: Nanocrystalline TiN Embedded in Amorphous SiNx*, in *Materials Science and Engineering*. 2007.
113. Birkholz, M., *Line Profile Analysis, in Thin Film Analysis by X-Ray Scattering*. 2006.
114. Berkum, J.G.M.v., et al., *Applicabilities of the Warren-Averbach analysis and an alternative analysis for separation of size and strain broadening*. Journal of Applied Crystallography, 1994. **27**: p. 345-357.
115. Kamminga, J.D. and L.J. Seijbel, *Diffraction line broadening analysis if broadening is caused by both dislocations and limited crystallite size*. Journal of Research of the National Institute of Standards and Technology, 2004. **109**(1): p. 65-74.
116. Louer, D. and N. Audebrand, *Profile fitting and diffraction line broadening analysis*. 1999, International Centre for Diffraction Data.
117. Kim, J.-M. and H.-T. Chung, *Electrochemical characteristics of orthorhombic LiMnO₂ with different degrees of stacking faults*. Journal of Power Sources, 2003. **115**(1): p. 125-130.
118. Rai, S., et al., *Characterization of low cycle fatigue damage in 9Cr-1Mo ferritic steel using X-ray diffraction technique*. International Journal of Pressure Vessels and Piping, 1999. **76**(5): p. 275-281.
119. Scherrer, P., *Bestimmung der Grösse und der Inneren Struktur von Kollidteilchen Mittels Röntgenstrahlen*, *Nachrichten von der Gessellschaft der Wissenschaften, Göttingen*. Mathematische-Physikalische Klasse, 1918. **2**: p. 98-100.
120. Monschi, A., M.R. Foroughi, and M.R. Monschi, *Modified Scherrer Equation to Estimate More Accurately No-Crystallite Size Using XRD*. World Journal of Nano Science and Engineering, 2012. **2**: p. 154-160.
121. Prabhu, Y.T., et al., *X-ray analysis of Fe doped ZnO nanoparticles by Williamson-Hall and size-strain plot*. International Journal of Engineering and Advaned Technology, 2013. **2**(4): p. 268-274.
122. Mayrhofer, P.H., G. Tischler, and C. Mitterer, *Microstructure and mechanical/thermal properties of Cr-N coatings by reactive unbalanced magnetron sputtering*. Surface and Coatings Technology, 2001(142-144): p. 78-84.
123. Bromark, M., et al., *PVD coatings for tool applications: Tribological evaluation*. Surface Engineering, 1994. **10**(3).

124. Thornton, J.A., *Stress-related effects in thin films*. Thin Solid Films, 1989. **171**: p. 5-31.
125. Mendibide, C., et al., *X-ray diffraction analysis of the residual stress state in PVD TiN/CrN multilayer coatings deposited on tool steel*. Surface and Coatings Technology, 2005. **200**(1-4): p. 165-169.
126. Kot, M., et al., *Effect of bilayer period on properties of Cr/CrN multilayer coatings produced by laser ablation*. Surface and Coatings Technology, 2008. **202**(15): p. 3501-3506.
127. Sue, J.A. and T.P. Chang, *Friction and wear behavior of titanium nitride, zirconium nitride and chromium nitride coatings at elevated temperatures*. Surface and Coatings Technology, 1995. **76-77, Part 1**(0): p. 61-69.
128. Hutchings, I.M. *Some comments on the theoretical treatment of erosive particle impacts*. in *5th International Conference on Erosion by Solid and Liquid*. 1979. Cambridge University, England.
129. Bhowmick, S., V. Jayaram, and S.K. Biswas, *Deconvolution of fracture properties of TiN films on steels from nanoindentation load-displacement curves*. Acta Materialia, 2005. **53**(8): p. 2459-2467.
130. Smail, J.W., D.J. Green, and M.B. Abrams, *Onset of Cone Cracking in Ion-Exchanged Glass*. Journal of the American Ceramic Society, 2007. **90**(1): p. 333-335.
131. Qasim, T., et al., *Effect of indenter size on critical conditions for contact damage in planar and non-planar bi-layers*. Strength, Fracture and Complexity, 2004. **2**(2): p. 81-93.
132. Lee, K.S., et al., *Cracking of Brittle Coatings Adhesively Bonded to Substrates of Unlike Modulus*. Journal of Materials Research, 2000. **15**(08): p. 1653-1656.
133. Lee, C.-S., B.R. Lawn, and D.K. Kim, *Effect of Tangential Loading on Critical conditions for radial cracking in brittle coatings*. Journal of American Ceramic Society, 2001. **84**(11): p. 2719-2721.
134. Lawn, B.R., et al., *Damage-Resistant Brittle Coatings*. Advanced Engineering Materials, 2002. **2**(00).
135. Qasim, T., et al., *Effect of coating thickness on crack initiation on crack propagation in non-planar bi-layers*. Material Science and Engineering, 2006. **419**: p. 189-195.
136. Cheng, Y.H., et al., *Mechanical and tribological properties of Ti/TiN multilayer coatings*. Surface and Coatings Technology, 2010. **204**: p. 146-151.
137. Ramanujam, N. and T. Nakamura, *Erosion mechanisms of thermally sprayed coatings with multiple phases*. Surface and Coatings Technology, 2009. **24**: p. 42-53.
138. Major, L., et al., *Microstructure design and tribological properties of Cr/CrN and TiN/CrN multilayer films*. Advanced Engineering Materials, 2008. **10**(7): p. 617-621.
139. Leterrier, Y., *Fragmentation test method for adhesion of coatings In situ in a microscope*. 2009, Ecole Polytechnique Lussanne.
140. C.Mitterer, O. Heuze, and V.-H.Derflinger, *Substrate and coatings damage by arcing during sputtering*. Surface and Coatings Technology, 1997. **89**(3): p. 233-238.
141. Wilkund, U., J. Gunnars, and S. Hogmark, *Influence of residual stresses on fracture and delamination of thin hard coatings*. Wear 1999. **232**: p. 262-269.
142. Q.Yang, et al., *Erosion resistance performance of magnetron sputtering deposited TiAlN coatings*. Surface and Coatings Technology, 2004. **188-189**: p. 168-173.
143. Laguna-Camacho, J.R., et al., *Solid particle erosion behaviour of TiN coating on AISI4140 Steel*. Journal of Surface Engineered Materials and Advanced Technology, 2014(4): p. 1-8.
144. Kim, G.S., et al., *Synthesis of CrN/AlN superlattice coatings using closed-field unbalanced magnetron sputtering process*. Surface and Coatings Technology, 2003. **171**(1-3): p. 91-95.
145. Shtanskil, D.V., et al., *Structure and physical-mechanical properties of nanostructured thin films*. Low Dimensional Systems and Surface Physics, 2003. **45**(6): p. 1122-1129.
146. Yoon, J.S., et al., *A study on the synthesis and microstructure of WC-TiN superlattice coating*. Surface and Coatings Technology, 2000. **131**(1-3): p. 372-377.
147. Musil, J., *Hard and superhard nanocomposite coatings*. Surface and Coatings Technology, 2000. **125**: p. 322-330.
148. Lee, K.S., *Effect of elastic modulus mismatch on the contact crack initiation in hard ceramic coating layer*. KSME International Journal, 2003. **17**(1): p. 1928-1937.

149. Miranda, P., et al., *Designing damage-resistant brittle-coating structures: I. Bilayers*. Acta Materialia, 2003. **51**: p. 4347-4356.
150. Lawn, B.R., et al., *Damage-resistant brittle coatings*. Advanced Engineering Materials, 2000. **2**(11): p. 746-747.
151. Tsui, T.Y., *Substrate effects on nanoindentation mechanical property measurement of soft films on hard substrates*. Journal of Materials Research, 1999. **14**(1): p. 292-301.
152. T.J.Lardner, R.J. .Giovianzzo, and J.E. Ritter, *The effect of high modulus single and double layer coatings on contact stresses*. Philosophical Magazine A, 2006. **66**(3): p. 452.
153. Borawski, B., et al., *The influence of ductile interlayer material on the particle erosion resistance of multilayered TiN based coatings*. Wear, 2011. **271**(11-12): p. 2891.
154. Lipperman, F., M. Ryvkin, and M.B. Fuchs, *Design of crack-resistant two dimensional periodic cellular materials*. Journal of Mechanics of Materials and Structures, 2009. **4**(3): p. 441-457.
155. Chen, J. and S.J. Bull, *Approaches to investigate delamination and interfacial toughness in coated systems: an overview*. Journal of Applied Physics, 2011. **44**: p. 3.
156. Wäppling, D., J. Gunnars, and P. Stahle, *Crack growth across a strength mismatched bimaterial interface*. International Journal of Fracture, 1998. **89**: p. 223-243.